INDUCED CURRENT MAGNETIC RESONANCE
ELECTRICAL IMPEDANCE TOMOGRAPHY (ICMREIT) WITH LOW
FREQUENCY SWITCHING OF GRADIENT FIELDS

A THESIS SUBMITTED TO
THE GRADUATE SCHOOL OF NATURAL AND APPLIED SCIENCES
OF
MIDDLE EAST TECHNICAL UNIVERSITY

BY

HASAN HÜSEYİN EROĞLU

IN PARTIAL FULFILLMENT OF THE REQUIREMENTS
FOR
THE DEGREE OF DOCTOR OF PHILOSOPHY
IN
ELECTRICAL AND ELECTRONICS ENGINEERING

JULY 2017

Approval of the thesis:

**INDUCED CURRENT MAGNETIC RESONANCE
ELECTRICAL IMPEDANCE TOMOGRAPHY (ICMREIT) WITH LOW
FREQUENCY SWITCHING OF GRADIENT FIELDS**

submitted by **HASAN HÜSEYİN EROĞLU** in partial fulfillment of the requirements for the degree of **Doctor of Philosophy in Electrical and Electronics Engineering Department, Middle East Technical University** by,

Prof. Dr. Gülbin Dural Ünver   _____
Dean, Graduate School of **Natural and Applied Sciences**

Prof. Dr. Tolga Çiloğlu   _____
Head of Department, **Electrical and Electronics Engineering**

Prof. Dr. B. Murat Eyüboğlu   _____
Supervisor, **Electrical and Electronics Engineering Dept., METU**

Examining Committee Members:

Prof. Dr. Özlem Aydın Çivi   _____
Electrical and Electronics Engineering Dept., METU

Prof. Dr. B. Murat Eyüboğlu   _____
Electrical and Electronics Engineering Dept., METU

Prof. Dr. Yusuf Ziya İder   _____
Electrical and Electronics Engineering Dept., Bilkent University

Prof. Dr. Ergin Atalar   _____
Electrical and Electronics Engineering Dept., Bilkent University

Assoc. Prof. Dr. Özgür Ergül   _____
Electrical and Electronics Engineering Dept., METU

                  Date: 10/07/2017

I hereby declare that all information in this document has been obtained and presented in accordance with academic rules and ethical conduct. I also declare that, as required by these rules and conduct, I have fully cited and referenced all material and results that are not original to this work.

Name, Last name : Hasan Hüseyin Eroğlu

Signature   :

ABSTRACT

INDUCED CURRENT MAGNETIC RESONANCE ELECTRICAL IMPEDANCE TOMOGRAPHY (ICMREIT) WITH LOW FREQUENCY SWITCHING OF GRADIENT FIELDS

Eroğlu, Hasan Hüseyin

Ph.D., Department of Electrical and Electronics Engineering

Supervisor: Prof. Dr. B. Murat Eyüboğlu

July 2017, 150 pages

In this thesis, it is aimed to investigate induced current magnetic resonance electrical impedance tomography (ICMREIT) starting from modeling and analysis to experimental validation. Forward and inverse problems of ICMREIT are formulated. A magnetic resonance imaging (MRI) pulse sequence is proposed for the realization of ICMREIT using the slice selection (z) gradient coil of MRI scanners. Considering the proposed MRI pulse sequence, relationship between the low frequency (LF) MR phase and the secondary magnetic field is expressed. Forward problem is solved using finite element method (FEM) for z and y gradient coils of MRI scanners. For the solution of the inverse problem, J-derivative and E-calculation image reconstruction algorithms are proposed and the performance of the algorithms is evaluated by using simulated measurements. Sensitivity and distinguishability analyses are

performed in order to investigate imaging characteristics of ICMREIT. Phantom experiments are performed for physical realization of ICMREIT. Simulated and physical LF phase measurements have similar characteristics. Low sensitivity of LF phase measurements is thought to be the main reason for the quantitative difference between the simulated and experimental measurements and the major limitation of the method towards clinical applications. Using the LF phase measurements, current density and true conductivity images are reconstructed. Reconstructed current density and conductivity images show that ICMREIT is a safe and a potentially applicable medical imaging method. Reconstructed conductivity images are rough estimates of the simple phantoms and they exhibit qualitative reconstructions rather than quantitative images. Sensitivity of LF phase measurements and image reconstruction performance should be increased in order to use the method in clinical practice.

Keywords: Induced current magnetic resonance electrical impedance tomography (ICMREIT), finite element method (FEM), magnetic resonance (MR) phase imaging, low frequency (LF) phase, image reconstruction.

ÖZ

GRADYAN ALANLARIN DÜŞÜK FREKANSTA ANAHTARLANMASIYLA AKIM İNDÜKLEMELİ MANYETİK REZONANS ELEKTRİKSEL EMPEDANS TOMOGRAFİSİ (AİMREET)

Eroğlu, Hasan Hüseyin

Doktora, Elektrik ve Elektronik Mühendisliği Bölümü

Tez Yöneticisi: Prof. Dr. B. Murat Eyüboğlu

Temmuz 2017, 150 sayfa

Bu tezde, akım indüklemeli manyetik rezonans elektriksel empedans tomografisi (AİMREET) yönteminin modelleme ve çözümlemeden başlayarak deneysel gerçekleştirmeye kadar devam eden bir süreçte incelenmesi amaçlanmıştır. AİMREET ileri ve ters problemleri formülize edilmiştir. AİMREET'nin manyetik rezonans görüntüleme (MRG) tarayıcılarında bulunan kesit seçici (z) gradyan sargısı aracılığıyla gerçekleştirilebilmesi için bir MRG darbe dizini önerilmiştir. Önerilen MRG darbe dizini dikkate alınarak düşük frekanslı (DF) MR faz bileşeni ile ikincil manyetik alan arasındaki ilişki açıklanmıştır. İleri problem, MRG tarayıcılarının z ve y gradyan sargıları için sonlu elemanlar yöntemi (SEY) kullanılarak çözülmüştür. Ters problemin çözümü için J-türevi ve E-hesaplama görüntü geriçatım yordamları önerilmiş ve yordamların başarımları benzetim ölçümleri aracılığıyla değerlendirilmiştir.

AİMREET'nin görüntüleme niteliklerinin incelenmesi için duyarlılık ve ayırt edilebilirlik çözümlemeleri gerçekleştirilmiştir. AİMREET'nin fiziksel gerçeklemesi için fantom deneyleri yapılmıştır. Benzetimler ve deneyler sonucunda elde edilen DF faz ölçümlerinin nitelikleri benzerdir. DF faz ölçümlerinin düşük duyarlılığının benzetim ve deney ölçümleri arasındaki nicel farkın ana nedeni olduğu ve yöntemin klinik uygulamalara yönelik en büyük sınırlaması olduğu düşünülmektedir. DF faz ölçümleri kullanılarak akım yoğunluğu ve gerçek iletkenlik görüntüleri geriçatılmıştır. Geriçatılan akım yoğunluğu ve iletkenlik görüntüleri AİMREET'nin güvenli ve uygulama potansiyeli olan bir tıbbi görüntüleme yöntemi olduğunu göstermektedir. Geriçatılan iletkenlik görüntüleri, basit fantomların kaba tahminleri olup nicel görüntülerden daha çok nitel geriçatımları sergilemektedir. Yöntemin klinik uygulamalarda kullanılması için DF faz ölçümlerinin duyarlılıklarının ve görüntü geriçatım başarımının artırılması gerekmektedir.

Anahtar Kelimeler: Akım indüklemeli manyetik rezonans elektriksel empedans tomografisi (AİMREET), sonlu elemanlar yöntemi (SEY), manyetik rezonans (MR) faz görüntüleme, düşük frekans (DF) faz, görüntü geriçatımı.

To the bright future

ACKNOWLEDGEMENTS

I express my sincerest gratitude to my supervisor, Prof. Dr. B. Murat Eyüboğlu, for his continuous support, guidance, patience, motivation, and contributions throughout my graduate education and thesis study.

I express my gratitude to my friend Mehdi Sadighi, for his continuous support, friendship, and help throughout my graduate education and thesis study. He participated in almost all parts of the experiments. He also contributed to my thesis by discussing the results after each experiment. Without his valuable help and support, I couldn't finish this thesis.

I express my gratitude to Thesis Monitoring Committee (TMC) members, Prof. Dr. Ergin Atalar and Assoc. Prof. Dr. Özgür Ergül for expressing their valuable comments and recommendations to my thesis progress reports in six TMC meetings.

I express my gratitude to Prof. Dr. Yusuf Ziya İder and Prof. Dr. Özlem Aydın Çivi for accepting to be a member of my thesis jury and evaluate my thesis.

TABLE OF CONTENTS

LIST OF TABLES

LIST OF FIGURES

xvii

xviii

LIST OF ABBREVIATIONS

LF	: Low Frequency
RF	: Radio Frequency
AC	: Alternating Current
EIT	: Electrical Impedance Tomography
ICEIT	: Induced Current Electrical Impedance Tomography
MR	: Magnetic Resonance
MRI	: Magnetic Resonance Imaging
MRCDI	: Magnetic Resonance Current Density Imaging
ACCDI	: AC Current Density Imaging
MREIT	: Magnetic Resonance Electrical Impedance Tomography
ICMREIT	: Induced Current Magnetic Resonance Electrical Impedance Tomography
EPT	: Electric Properties Tomography
LF-EPT	: Low Frequency Electric Properties Tomography
LF-MREPT	: Low Frequency Magnetic Resonance Electric Properties Tomography
FOV	: Field of View
IEC	: International Electrotechnical Commission
3D	: Three Dimensional
BVP	: Boundary Value Problem
FEM	: Finite Element Method

CW	: Clockwise
CCW	: Counter Clockwise
GS	: Gradient Strength
SR	: Slew Rate
ST	: Slice Thickness
DOF	: Degrees of Freedom
SNR	: Signal to Noise Ratio
PE	: Phase Encoding
RO	: Read-out
SS	: Slice Selection
EPI	: Echo-Planar Imaging
RL	: Resistive-Inductive
MHD	: Magnetohydrodynamic
Ph	: Phantom
Sltn	: Solution
Inh	: Inhomogeneity
NaCl	: Sodium-Chloride
CuSO4	: Copper-Sulfate
T	: Tesla
A	: Ampere
V	: Volt
s	: Second
m	: Meter
rad	: Radian
°	: Degree
Hz	: Hertz
π	: Pi Constant
S	: Siemens
dB	: Decibel

l	: Liter
g	: Gram
k	: Kilo
m	: Milli
c	: Centi
μ	: Micro
n	: Nano
a.u.	: Arbitrary Unit
pu	: Per Unit

LIST OF SYMBOLS

(x, y, z) : Cartesian Coordinates

(r, φ, z) : Cylindrical Coordinates

R : Distance Between Source and Field Points

$\overline{(\cdot)}$: Vector Field

$\hat{a}_{(.)}$: Unit Vector in $(\cdot)$ Direction

$(\cdot)_i$: Orthogonal Projection of a Vector Field in $\hat{a}_i$ direction

$\left\| \overline{(\cdot)} \right\|$: Norm of a Vector Field

$\left| \overline{(\cdot)} \right|$: L_2 (Euclidean) Norm of a Vector Field

$\times$: Cross Product

$\cdot$: Dot Product

$\nabla(\cdot)$: Gradient of a Scalar Field

$\nabla^2(\cdot)$: Laplacian of a Field

$\nabla \times \overline{(\cdot)}$: Curl of a Vector Field

$(\cdot)_{avg}$: Average Value of a Distribution

$(\cdot)_{max}$: Maximum Value of a Distribution

$(\cdot)_{peak}$: Peak Value of a Waveform

$(\underline{\cdot})$: Tensor

$\overline{B}$: Magnetic Flux Density

B_o : Main Magnetic Field of an MRI Scanner

B_1	: Magnetic Field Created by an RF Coil of an MRI Scanner
$\overline{B}_p$	: Primary Magnetic Flux Density
$\overline{B}_s$	: Secondary Magnetic Flux Density
$\overline{E}$	: Electric Field Intensity
$\overline{J}$	: Electrical Current Density
$\overline{J}_{LF}$	: Low Frequency Eddy Current
$\overline{J}_{LF-sys}$	: Low Frequency Eddy Current Induced in the Conductors of the MRI Scanner, System Eddy Current
$\overline{J}_{LF-sys}^{ss}$	: Steady State Value of $\overline{J}_{LF-sys}$
$\overline{J}_{RF}$	: Radio Frequency Eddy Current
$\overline{A}$	: Vector Magnetic Potential
V	: Scalar Electric Potential
I	: Electrical Current
$\bar{n}$	: Normal Vector
Ω	: A Bounded Domain
$\partial\Omega$	: Boundary of Ω
Ω_∞	: Infinite Element Domain
N_e	: Number of Finite Elements
N_{edge}	: Number of Edge Elements
N_{tri}	: Number of Triangular Elements
N_{teth}	: Number of Tetrahedral Elements
N_i	: Number of Iterations
N_p	: Number of Pixels
$[A]_{N\times N}$	: A Matrix with a Size of $N \times N$
$[A_{ij}]$	: A Matrix Element Corresponding to ij^{th} Pixel
$[b_{ij}]$	: A Vector Element Corresponding to ij^{th} Pixel

σ : Electrical Conductivity

σ_{ref} : Reference Conductivity Distribution

σ_{rec} : Reconstructed Conductivity Distribution

σ_b : Background Conductivity

σ_{ih} : Conductivity of an Inhomogeneity

$\Delta\sigma$: Conductivity Difference of an Inhomogeneity from the Background

ρ : Resistivity

ε : Dielectric Permittivity

ε_o : Dielectric Permittivity of Free Space

ε_r : Relative Permittivity

μ : Magnetic Permeability

μ_o : Magnetic Permeability of Free Space

γ : Gyromagnetic Ratio of Hydrogen

f : Electrical Frequency

ω : Angular Frequency

T : Period of a Waveform

N_{coil} : Number of Turns

I_{coil} : Magnitude of the Excitation Current

S : Cross Sectional Area

Φ : MR Phase Distribution

Φ_{LF} : MR Phase Induced by $\bar{J}_{LF}$

Φ_{RF} : MR Phase Induced by $\bar{J}_{RF}$

Φ_{RF_leak} : RF Leakage Phase in Φ_{LF} Distribution

$\Phi_{RF}{}^{shifted}$: Shifted RF Phase by Geometrical Distortions

$\Phi_{LF}{}^{shifted}$: Shifted LF Phase by Geometrical Distortions

Φ_{diff} : MR Phase Contribution of Diffusion Flux

Φ_{MHD} : MR Phase Contribution of Flow Effects

G_x	: Read-out Gradient of an MRI Scanner
G_y	: Phase-encoding Gradient of an MRI Scanner
G_z	: Slice-selection Gradient of an MRI Scanner
$G_{(\cdot)}{}^+$	: A Gradient Waveform Applied in ($\cdot$) Direction with Positive Polarity
$G_{(\cdot)}{}^-$	: A Gradient Waveform Applied in ($\cdot$) Direction with Negative Polarity
Δx	: Geometrical Distortion in Read-Out Gradient Axis of an MRI Scanner
$(\cdot)^+$	: ($\cdot$) Distribution Obtained with $G_{(\cdot)}{}^+$
$(\cdot)^-$	: ($\cdot$) Distribution Obtained with $G_{(\cdot)}{}^-$
N_{cycle}	: Number of Cycles of a Gradient Waveform
T_c	: Coil Excitation Interval of an MRI Pulse Sequence for ICMREIT
T_s	: Duration of $\bar{J}_{LF}$ pulses in a Single Cycle of a Gradient Waveform
T_w	: Interval Between the 90$^\mathrm{o}$ RF Pulses and the Coil Current
T_{plt}	: Plateau of Gradient Pulses
T_E	: Echo Time of an MRI Pulse Sequence
T_R	: Pulse Repetition Time of an MRI Pulse Sequence
t_r	: Ramp Time of Gradient Pulses
t_A	: Interval Between the 90$^\mathrm{o}$ RF Pulses and the Gradient Waveform for the MRI Pulse Sequence proposed for ICMREIT
t_B	: Interval Between the 90$^\mathrm{o}$ RF Pulse and the first 180$^\mathrm{o}$ RF Pulse for the MRI Pulse Sequence proposed for ICMREIT
t_C	: Interval Between the Soft and the Hard 180$^\mathrm{o}$ RF Pulses for the MRI Pulse Sequence proposed for ICMREIT
t_D	: Interval of Repetitive 180$^\mathrm{o}$ RF Pulses for the MRI Pulse Sequence Proposed for ICMREIT
ϵ_σ	: Conductivity Reconstruction Error
$\epsilon_{\sigma-g}$	: Conductivity Reconstruction Error for the Whole Phantom (Global)
$\epsilon_{\sigma-l}$	: Conductivity Reconstruction Error for an Inhomogeneity (Local)

ϵ_J	: Current Density Reconstruction Error
ϵ_{lim}	: Lower Limit for $|\overline{E}|$ Values
D	: Distinguishability Function
ϵ	: A Very Small Numerical Value, Epsilon
θ	: Angular Position
C_{ih}	: Center of a Cylindrical Conductivity Inhomogeneity
P	: Radius of a Cylindrical Conductor
h	: Height of a Cylindrical Conductor
d_{ih}	: Diameter of a Cylindrical Conductivity Inhomogeneity
ρ_{ih}	: Radius of a Cylindrical Conductivity Inhomogeneity
Δx_{ph-ih}	: Distance Between the Center of the Phantom and the Inhomogeneity
$R_{min/max}$	: Ratio between the minimum and the maximum $|\Delta B_z(x,y)|_{avg}$ values
$R_{ih/bg}$	: Conductivity Contrast Ratio Between the Inhomogeneities and the Background
R_{sys}	: Effective Resistance of the Conductive Parts of the MRI Scanner, Effective Resistance of the MRI System
L_{sys}	: Effective Inductance of the Conductive Parts of the MRI Scanner, Effective Inductance of the MRI System
τ	: Time Constant of the Conductive Parts of the MRI Scanner, Time Constant of the MRI System, L_{sys}/R_{sys}
D_m	: Diffusion Coefficient
C	: Concentration
$\bar{j}_{diff}$	: Diffusion Flux
$\bar{j}_{drift}$	: Drift Flux
μ_p	: Mobility of pth Ion

z_p : Valance of pth Ion

C_p : Concentration of pth Ion

$\overline{F}_{em}$: Lorentz Force

ρ_{fl} : Fluid Density

$\overline{u}$: Fluid Velocity

T_1 : Longitudinal Relaxation Time Constant

T_2 : Transverse Relaxation Time Constant

CHAPTER 1

INTRODUCTION

Low frequency (LF) electrical conductivity imaging of biological tissues has attracted the interest of many researchers in the past decades since the electrical conductivity distributes between the tissues and changes with respect to the physiological responses [1-4]. The starting point of LF electrical conductivity imaging is electrical impedance tomography (EIT) which is based on locating electrodes on the surface of a volume conductor object and injecting electrical current through these electrodes [5-15]. Distribution of the injected current inside the object with respect to the object conductivity creates an electrical potential field, which is measured through the surface electrodes, and these potential measurements are used to reconstruct conductivity images [5-15]. Today, EIT is utilized in intensive care units for monitoring ventilation and perfusion of patients [10-15]. As an alternative to injected current EIT, induced current EIT (ICEIT) is proposed, in which eddy current is induced in a volume conductor object by exciting a nearby coil with time varying electrical current [16-18]. Similar to the injected current EIT, induced eddy current generates an electrical potential field, which is measured by means of surface electrodes, and these potential measurements are used to reconstruct conductivity images [16-18]. It is reported that sensitivity of surface potential measurements to internal conductivity perturbations is very low and

reconstructed conductivity images of EIT suffer from low spatial resolution, which can be considered as the major drawbacks of the method [10].

In the beginning of 1990s, it is proposed to synchronize electrical current injection with magnetic resonance imaging (MRI) techniques in order to reconstruct current density distribution through the object to be imaged [19-20]. This method is known as magnetic resonance current density imaging (MRCDI) in which electrical current is injected to an object including magnetic resonance (MR) active nuclei in synchrony with an MRI pulse sequence [19-21]. Distribution of the injected current inside the object with respect to the object conductivity creates a magnetic flux density distribution, the z component of which (B_z) induces phase in MR images. By using MR phase imaging methods and Ampere's Law, B_z and current density images are reconstructed, respectively [19-23]. The reconstructed current density images take the advantage of equal sensitivity and high resolution of B_z measurements throughout the field of view (FOV) [19-23]. After the introduction of MRCDI, it is proposed to reconstruct conductivity images by using B_z and surface potential measurements. This method is known as magnetic resonance electrical impedance tomography (MREIT) [24]. MREIT, which combines EIT and magnetic resonance imaging (MRI) modalities in the same platform [24-42], has reached the stage of animal experiments [30, 34-39]. Kim et al. also report conductivity images of a human leg as the results of an in-vivo MREIT experiment [36].

The necessity of injecting electrical current to body via surface electrodes constrains the clinical application of MREIT. Arpınar et al. [40] state that the amount of electrical current injected to a body in MREIT studies is higher than the patient auxiliary current limit of 100 μA mentioned in IEC 60601-2-33

standard [43]. To solve the application problems of MREIT related with injection current, Özparlak and İder propose induced current magnetic resonance electrical impedance tomography (ICMREIT) in a simulation study [44]. In ICMREIT, a coil located near a volume conductor object is excited with LF electrical current ($\bar{J}_{coil}$) in synchrony with an MRI pulse sequence. Due to the coil excitation, a primary magnetic flux density distribution ($\bar{B}_p$) is generated through the object. $\bar{B}_p$, which depends on $\bar{J}_{coil}$ and coil geometry is a known distribution. $\bar{B}_p$ induces LF eddy current ($\bar{J}_{LF}$) in the object to be imaged and $\bar{J}_{LF}$ generates a secondary magnetic flux density ($\bar{B}_s$) distribution through the object. Z component of $\bar{B}_s$ (B_{sz}) accumulates phase in MR signal (Φ_{LF}) and can be reconstructed by post-processing the MR phase (Φ) images. Conductivity images are reconstructed by using B_{sz} measurements and the z component of $\bar{B}_p$ (B_{pz}) [44-45].

As the pioneer of ICMREIT, Özparlak and İder propose an MRI pulse sequence for B_{sz} measurements [44]. This pulse sequence is based on spin-echo and adapted from the AC current density imaging (AC-CDI) pulse sequence proposed by Mikac et al. [23]. In this pulse sequence, $\bar{J}_{coil}$ with a sinusoidal form is applied to a discrete coil after a time interval (T_w) following the 90° excitation radio frequency (RF) pulse. $\bar{J}_{coil}$ induces $\bar{J}_{LF}$ in the object, which is 90° phase lagged compared to $\bar{J}_{coil}$. 180° refocusing RF pulses are applied at zero crossings of $\bar{J}_{LF}$ which results in phase accumulation in MR signal due to B_{sz}. Time instants of 180° refocusing RF pulses correspond to the peaks of $\bar{J}_{coil}$ waveform. Therefore, phase contribution of B_{pz} is zero. After a time interval of T_w following $\bar{J}_{coil}$ waveform, MR signal is read-out [44]. It is proposed to apply

$\bar{J}_{coil}$ twice with opposing polarities and take the difference of the resultant Φ distributions in order to obtain Φ_{LF} which can be expressed as

$$\Phi_{LF} = 2\,(-1)^{N_{cycle}}\gamma\,\left(\,2\,B_{sz\_peak}/\pi\,\right)T_c, \qquad (1.1)$$

where N_{cycle} represents the number of cycles of $\bar{J}_{coil}$ waveform, γ is gyromagnetic ratio of hydrogen, B_{sz_peak} is the peak value of B_{sz} waveform, $2B_{sz\_peak}/\pi$ is the average value of the full wave rectified B_{sz} waveform, and T_c is the time interval of coil excitation. Although the accumulation of Φ_{LF} due to the MRI pulse sequence in [44] is promising, the implementation of this pulse sequence is not straightforward since it requires the application of 180° refocusing RF pulses with a sinusoidally varying $\bar{J}_{coil}$ waveform.

Experimental realization of ICMREIT with a discrete coil [44] is difficult since it requires an MR compatible coil and a state of the art AC current supply for the excitation. Özsüt proposes the utilization of the read-out gradient coil of a 0.15T MRI scanner for inducing $\bar{J}_{LF}$ in a volume conductor [46]. Özsüt uses an MRI pulse sequence similar to the one presented in [44]. He applies a triangular gradient (G_x) after the 90° excitation RF pulse. At time instants on which G_x reach its peaks, 180° refocusing RF pulses are applied which results in accumulation of Φ_{LF} in MR signal. In [46], amplitude of G_x is adjusted and the resultant k-space magnitude images are investigated. It is stated that k-space magnitude image is concentrated in LF region and shifts out of the FOV, for low and high amplitudes of G_x, respectively [46].

Van Lier et al. propose applying conventional spin-echo MRI pulse sequence for inducing $\bar{J}_{LF}$ in a volume conductor and called this method as low

4

frequency-electric properties tomography (LF-EPT) [47]. They apply conventional spin-echo MRI pulse sequence twice with opposing read-out gradient polarities. They state that RF and LF components of the Φ images obtained in two acquisitions have the same and opposite polarities, respectively [47]. By adding and subtracting the resultant Φ images, phase contribution of RF pulses (Φ_{RF}) and Φ_{LF} are obtained. The results of phantom experiments performed on a 3T MRI scanner show that Φ_{RF} and Φ_{LF} profiles passing through the phantoms have parabolic curvature and linear slope, respectively. It is stated that curvature of Φ_{RF} and slope of Φ_{LF} profiles change according to RF and LF conductivity distributions of the phantoms, respectively [47].

Oran et al. propose applying conventional gradient-echo MRI pulse sequence for inducing $\bar{J}_{LF}$ in a volume conductor and called this method as low frequency-magnetic resonance electric properties tomography (LF-MREPT) [48]. They apply conventional gradient-echo MRI pulse sequence twice with opposing read-out gradient polarities and subtract the resultant Φ images in order to obtain Φ_{LF} distribution. They derive a convection reaction based conductivity image reconstruction algorithm in order to reconstruct conductivity images with B_{sz} and B_{pz} distributions. They build a simulation model composed of an x-gradient coil and a block with a cylindrical inhomogeneity. Using the simulated measurements, they reconstruct conductivity images with high accuracy. They build an experimental phantom similar to the one used in the simulation. They perform physical experiments on a 3T clinical MRI scanner. They express that B_{sz} measurements are feasible and $\nabla^2 \overline{B}_s$ has decreasing characteristics through x direction [48].

In a simulation study, de Geeter et al. propose applying a trapezoidal

gradient pulse before the conventional gradient-echo MRI pulse sequence for inducing $\bar{J}_{LF}$ in a volume conductor [49]. They state that Φ_{LF} can be recovered by applying the MRI pulse sequence twice with and without the $\bar{J}_{LF}$ inducing gradient pulse and taking the difference of the resultant Φ images [49]. Due to the Faraday's Law of electromagnetic induction, $\bar{J}_{LF}$ distributions induced during the rise and the fall time of the gradient pulse are opposite of each other. As a result, MR phase contribution of $\bar{J}_{LF}$ is zero since the MR phases accumulated during the rise and the fall time of the gradient pulse cancel out each other.

Eroğlu and Eyüboğlu are the first to propose the utilization of slice selection (z) gradient coil for the realization of ICMREIT [50]. They formulate the forward problem of ICMREIT and perform computer simulations for a numerical model composed of a z-gradient coil around a cylindrical conductor. They calculate Φ_{LF} distributions based on the MRI pulse sequence proposed by Özparlak and İder [44]. They conclude that ICMREIT can be realized with z-gradient coils of MRI scanners without the need for an additional hardware [50]. Eroğlu and Eyüboğlu also compare MREIT and ICMREIT in a simulation study [51] by using sensitivity and distinguishability [52] analyses. They state that sensitivity of ICMREIT measurements is related with radial distance to the center of the conductor, and imaging concentric inhomogeneities with ICMREIT is very difficult. Position dependent sensitivity of ICMREIT measurement is stated as the major drawback of the method compared with MREIT. They state that utilization of z-gradient coil may be a good choice for the experimental realization of ICMREIT [51].

Mandija et al. investigate the use of conventional spin-echo MRI pulse

6

sequence for the experimental realization of ICMREIT [53]. They locate an additional read-out gradient pulse around the 180° RF pulse of the spin-echo MRI pulse sequence and propose applying the pulse sequence twice with opposing read-out gradient polarities. They recover Φ_{RF} and Φ_{LF} distributions by adding and subtracting the acquired Φ images. They state that measured Φ images are prone to geometrical distortions (Δx) which are resulted from imaging imperfections such as inhomogeneity of main magnetic field (B_o) and system eddy current induced in conductors of MRI scanner. They state that Φ_{LF} measurements are affected by RF leakage, $\Phi_{RF\_leak} = \Delta x (\partial \Phi_{RF} / \partial x)$, which is related with conductivity. They apply artificial Δx shifts to the measured Φ images and calculate the shifted Φ_{LF} ($\Phi_{LF}^{shifted}$) distributions. They observe that $\Phi_{LF}^{shifted}$ distributions scale with Δx. However, the effect of Δx shifts is not observed in true Φ_{LF} distributions exhibited by the authors. They conclude that measured Φ_{LF} distributions may also be affected by measurement noise and their ICMREIT implementation is not feasible [53].

Gibbs and Liu propose using a gradient-echo MRI pulse sequence for the experimental realization of ICMREIT [54]. They apply a spoiler gradient with a trapezoidal form before RF excitation. By taking the duration of the spoiler pulse long, in the order of 5 ms, $\overline{J}_{LF}$ induced in the object during the rise time decays to zero and $\overline{J}_{LF}$ induced during the fall time contributes to Φ_{LF} distribution. They conclude that applying a spoiler gradient before RF excitation is not a feasible method for the experimental realization of ICMREIT [54] since induced $\overline{J}_{LF}$ decays to zero immediately due to the negligible inductance of the object to be imaged.

Oran and İder propose using a spin-echo MRI pulse sequence and

z-gradient coil to investigate feasibility of ICMREIT [55]. They formulate the forward and the inverse problems of ICMREIT and try to model Φ_{LF} distribution by utilizing the Φ_{RF_leak} concept proposed by Mandija et al [53]. They apply a spin-echo MRI pulse sequence with opposing slice selection gradient polarities [55]. It is observed that slice selection gradients of 90° and 180° RF pulses of the proposed pulse sequence [55] have opposite polarities which may select different slices of the object to be imaged unless center frequencies of these RF pulses are adjusted accordingly. They conclude that measured Φ_{LF} distributions are affected by Φ_{RF_leak} and their ICMREIT implementation is not feasible [55].

Literature survey shows that MR based LF conductivity imaging is an interesting field of research which deserves to be explored. Because of technical limitations and safety constraints, MR based LF conductivity imaging has not been applied to clinical imaging yet [40, 43]. ICMREIT can be considered as a promising alternative for LF conductivity imaging. However, no convincing experimental proof has been demonstrated up to now although the method [44] was introduced almost a decade ago. We also observe that the experimental studies about ICMREIT [46, 47-48, 53-55] do not use MRI pulse sequences including multi-cycle gradient waveforms as expressed in the original description of the method [44].

In this thesis, it is aimed to investigate ICMREIT starting from modeling and analysis through physical experiments.

In Chapter 2, forward and inverse problems of ICMREIT are formulated. An MRI pulse sequence is proposed for the experimental realization of ICMREIT.

8

In Chapter 3, numerical simulations are described in order to solve the forward and inverse problems of ICMREIT. Distinguishability and sensitivity analyses are introduced in order to investigate the imaging characteristics of ICMREIT. Experimental methods are described in order to validate the proposed method.

In Chapter 4, simulation and experimental results are presented.

In Chapter 5, simulation and experimental results are discussed by considering the existent literature about the subject. In addition, important aspects of the study are summarized.

In Chapter 6, thesis is concluded and future studies are suggested.

CHAPTER 2

THEORY

2.1 Forward Problem of ICMREIT

2.1.1 Definition and Numerical Solution of the Forward Problem

Forward problem of ICMREIT can be described as calculation of B_{sz} distribution through the object to be imaged due to the excitation of a nearby coil with time varying electrical current. Forward problem is described for a three dimensional (3D) geometry as shown in Figure 2.1. In Figure 2.1, Ω_c and Ω are a volume conductor object and an air filled spherical solution domain, σ and ε are the electrical conductivity and the dielectric permittivity of the object which are assumed to be isotropic, ε_o and μ_o are the dielectric permittivity and the magnetic permeability of free space, and $\bar{n}$ is the normal vector on the boundary of Ω ($\partial\Omega$). Time harmonic ($e^{j\omega t}$) electromagnetic fields with an angular frequency of ω are considered in the derivation of the forward problem. The forward problem is described starting from the Ampere's Law [50-51] as

$$\nabla \times \overline{B} = \mu\left[(\sigma + j\omega\varepsilon)\overline{E} + \overline{J}_{coil}\right], \qquad (2.1)$$
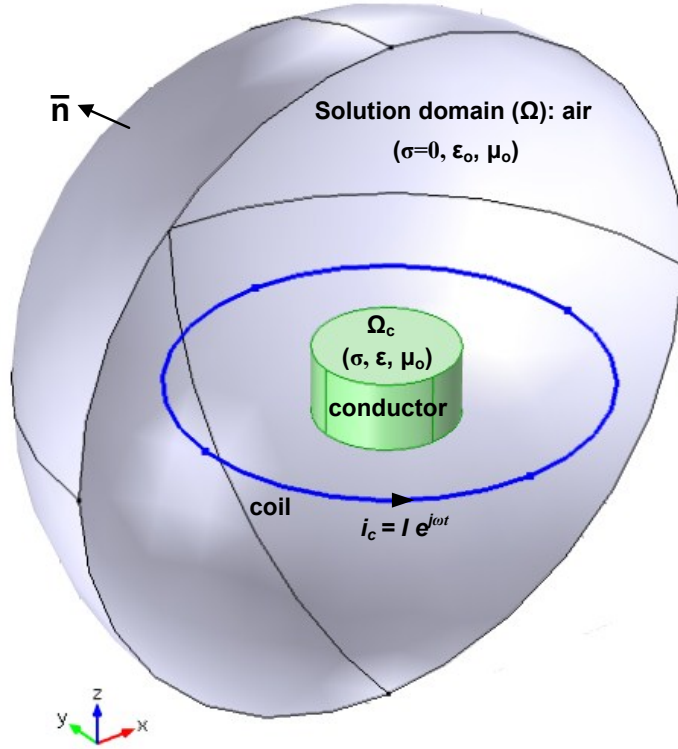
Figure 2.1 Geometrical structure used for the description of the forward problem. Half of the solution domain is not shown for visualization.

where $\overline{B}$ is the magnetic flux density, $\overline{E}$ is the electric field intensity, and $\overline{J}_{coil}$ is the coil current. $\overline{J}_{coil}$ can be expressed as

$$\overline{J}_{coil} = \begin{cases} \frac{N_{coil}I_{coil}}{S_{coil}} \hat{a}_{coil} \dots \dots \dots \dots \text{ on the coil} \\ 0 \dots \dots \dots \dots \text{ otherwise} \end{cases}, \qquad (2.2)$$

where N_{coil}, I_{coil}, S_{coil}, and $\hat{a}_{coil}$ are number of turns, magnitude of the excitation current, cross sectional area, and unit vector of the coil, respectively. $\overline{E}$ and $\overline{B}$ can be expressed as

$$\overline{E} = -j\omega\overline{A} - \nabla V \tag{2.3}$$

and

$$\overline{B} = \nabla \times \overline{A}, \tag{2.4}$$

where $\overline{A}$ and V are the vector magnetic and the scalar electric potentials, respectively. $\overline{A}$ and V can be transformed into new vector magnetic $(\tilde{\overline{A}})$ and scalar electric $(\tilde{V})$ potentials by introducing a scalar field (φ) as

$$\tilde{\overline{A}} = \overline{A} + \nabla\varphi \tag{2.5}$$

and

$$\tilde{V} = V - j\omega\varphi. \tag{2.6}$$

Choosing $\varphi = -\frac{j}{\omega}V$ and using (2.1-2.6) result in

$$(j\omega\sigma - \omega^2\varepsilon)\tilde{\overline{A}} + \mu^{-1}\left(\nabla \times \nabla \times \tilde{\overline{A}}\right) = \overline{J}_{coil} \tag{2.7}$$

In ICMREIT, ω is a low frequency in the order of $2\pi \times 1000$ rad/s. Therefore, quasi-static condition is assumed for the solution of the differential equation shown in (2.7). By this way, electromagnetic fields decay exponentially with distance [51, 56-57]. Considering the quasi-static condition, a magnetic insulation type boundary condition

$$\overline{n} \times \tilde{\overline{A}} = 0 \dots on\ \partial\Omega, \tag{2.8}$$

is used for the solution of (2.7) [50-51, 56-57]. Boundary value problem (BVP) shown in (2.7-2.8) is defined in a FEM solver COMSOL Multiphysics 5.1

(COMSOL AB, Sweden). In order to prevent reflections from $\partial\Omega$, Ω is stretched to a large extent which is called as infinite element domain (Ω_∞) [51, 58-59]. After the description of Ω_∞, the boundary condition shown in (2.8) is applied on the boundary of Ω_∞ ($\partial\Omega_\infty$). BVP shown in (2.7-2.8) is solved for $\bar{\bar{A}}$. Then, $\overline{E}$ and $\overline{B}$ are calculated by using (2.3-2.6). $\overline{J}_{LF}$ is calculated by using the Ohm's Law as

$$\overline{J}_{LF} = \sigma\overline{E} = -j\omega\sigma\bar{\bar{A}}. \tag{2.9}$$

$\overline{B}$ obtained as a result of the solution of BVP in (2.7-2.8) and equations (2.5-2.6) can be expressed as

$$\overline{B} = \overline{B}_p + \overline{B}_s. \tag{2.10}$$

Two simulations are performed in order to extract B_{sz} from $\overline{B}$. At first, true conductivity distribution of the object is used. In the second simulation, conductivity value of the object is equal to zero. By subtracting the z components of the resultant $\overline{B}$ distributions, B_{sz} distribution is obtained [50-51].

2.1.2 Semi-Analytical Solution of the Forward Problem

For a cylindrical conductor, $\overline{J}_{LF}$ can be expressed analytically which can be utilized as a baseline solution [51, 60]. The starting point is Faraday's Law which can be expressed as

$$\oint_L \overline{E}(r,\varphi,z) \cdot \overline{dl} = -\int_S j\omega B_{pz}(r,\varphi,z)\hat{a}_z \cdot \overline{dS}, \tag{2.11}$$

14

where (r, φ, z) are the coordinates in cylindrical coordinate system, L and S are the circumference and the area of the circular cross section of the conductor, respectively. It is assumed that circular cross section of the conductor is perpendicular to the z-axis. Considering the integration path, azimuthal (φ) components of $\overline{E}$ are considered. By using the Ohm's Law and evaluating (2.11) for the cylindrical geometry, $\overline{J}_{LF}$ can be expressed as

$$\overline{J}_{LF}(r, \varphi, z) = -\frac{1}{2}\, j\omega\, r\, \sigma(r, \varphi, z)\, B_{pz}(r, \varphi, z)\, \hat{a}_\varphi. \qquad (2.12)$$

By using the Biot-Savart Law and (2.12), B_{sz} can be calculated as

$$B_{sz}(r, \varphi, z) = \frac{-j\omega\mu_o}{8\pi} \int_{object} \sigma(r')r' B_{pz}(r', \varphi', z') \frac{[r' - r\cos(\varphi - \varphi')]}{R^3} dV',$$

$$(2.13)$$

where (r', φ', z') and (r, φ, z) represent the source and the field points, respectively and R is the distance between the source and the field points. B_{pz} is obtained as a result of the numerical solution of the BVP shown in (2.7-2.8) and (2.5-2.6) when the conductivity of the object is equal to zero. $\overline{J}_{LF}$ is calculated by using (2.12) and the B_{pz} distribution obtained from the numerical solution of the forward problem. Therefore, the method shown in (2.12) is referred to as semi-analytical solution of the forward problem. Reliability of the numerical solution is evaluated by inspecting L_2 norm of $\overline{J}_{LF}$ distributions ($|\overline{J}_{LF}|$) obtained from the semi-analytical and the numerical solutions.

2.2 Inverse Problem of ICMREIT

2.2.1 Definition of the Inverse Problem

Inverse problem of ICMREIT can be defined as the reconstruction of conductivity distribution of the object to be imaged by using B_{sz} measurements and readily known B_{pz} distribution [44-45]. Inverse problem can be derived starting from Ampere's and Faraday's laws which can be expressed as

$$\nabla \times \overline{E} = -j\omega\overline{B} \tag{2.14}$$

and

$$\nabla \times \overline{B} = \mu(\sigma + j\omega\varepsilon)\overline{E}, \tag{2.15}$$

Substituting conservation of magnetic flux

$$\nabla \cdot \overline{B} = 0 \tag{2.16}$$

and (2.15) in a vector identity

$$\nabla \times \nabla \times \overline{B} = \nabla(\nabla \cdot \overline{B}) - \nabla^2\overline{B} \tag{2.17}$$

results in

$$\nabla^2\overline{B} = -\nabla \times \left[\mu(\sigma + j\omega\varepsilon)\overline{E} \right]. \tag{2.18}$$

Substituting (2.14) in (2.18) results in

$$\nabla^2\overline{B} = -\frac{\mu\,\nabla(\sigma+j\omega\varepsilon)}{\mu(\sigma+j\omega\varepsilon)} \times \left(\nabla \times \overline{B}\right) + j\omega\mu\,(\sigma + j\omega\varepsilon)\overline{B}. \tag{2.19}$$

16

In ICMREIT, it is aimed to image σ distribution of biological tissues varying between 0 and 2 S/m [1]. Consider a volume conductor with a σ value of 1 S/m and a relative permittivity (ε_r) value of 78.4, which is equal to the ε_r value of water [61]. For $\omega = 2\pi \times 1000$ rad/s and $\varepsilon_r = 78.4$, $\omega\varepsilon = \omega\varepsilon_r\varepsilon_o = 4.36 \times 10^{-6}$ S/m is much smaller than 1 S/m. Therefore, $\sigma \gg \omega\varepsilon$ is assumed and (2.19) can be expressed as

$$\nabla^2 \overline{B} = -\frac{\nabla\sigma}{\sigma} \times \left(\nabla \times \overline{B}\right) + j\omega\mu\sigma\overline{B}. \tag{2.20}$$

Considering the z component of $\overline{B}$ and substituting (2.10) in (2.20) result in

$$\nabla^2\left[(B_{pz} + B_{sz})\hat{a}_z\right] = -\frac{\nabla\sigma}{\sigma} \times \left[\nabla \times (B_{pz} + B_{sz})\hat{a}_z\right] + j\omega\mu\sigma(B_{pz} + B_{sz})\hat{a}_z,$$

$$\tag{2.21}$$

where B_{pz} is a readily known distribution depending on coil geometry and excitation current, B_{sz} is the measured distribution, and σ is the unknown distribution to be reconstructed. Equation (2.21), which expresses the relationship between σ and $\overline{B}$, is the inverse problem of ICMREIT. For the solution of the inverse problem of ICMREIT, image reconstruction algorithms are presented in the following sections.

2.2.2 E-calculation Algorithm

The relationship between x and y components of $\overline{J}_{LF}$ (J_x and J_y) and $\overline{B}_s$ can be expressed by using Ampere's Law as

$$\nabla \times \overline{B}_s = \mu_o \left(J_x \hat{a}_x + J_y \hat{a}_y \right). \tag{2.22}$$

In MRI, magnetic field components in direction of B_o (z direction) contribute to the phase of MR signal. Therefore, J_x and J_y can be calculated by substituting B_{sz} in (2.22) as

$$J_x = \frac{1}{\mu_o} \frac{\partial B_{sz}}{\partial y} \tag{2.23}$$

and

$$J_y = -\frac{1}{\mu_o} \frac{\partial B_{sz}}{\partial x}. \tag{2.24}$$

$\left| \overline{J}_{LF} \right|$ can be calculated as

$$\left| \overline{J}_{LF} \right| = \sqrt{J_x{}^2 + J_y{}^2}. \tag{2.25}$$

The angle (α) between J_x and J_y can be calculated as

$$\alpha = tan^{-1} \left(\frac{J_y}{J_x} \right). \tag{2.26}$$

Since $B_{pz} \gg B_{sz}$, z component of (2.14) can be expressed as

$$\frac{\partial E_y}{\partial x} - \frac{\partial E_x}{\partial y} = -j\omega B_{pz}, \tag{2.27}$$

where E_x and E_y are x and y components of $\overline{E}$, respectively. E_x and E_y can be expressed in terms of L_2 norm of $\overline{E}$

$$|\overline{E}| = \sqrt{E_x{}^2 + E_y{}^2} \qquad (2.28)$$

and α as

$$E_x = |\overline{E}|cos\alpha \qquad (2.29)$$

and

$$E_y = |\overline{E}|sin\alpha. \qquad (2.30)$$

Substituting (2.29-2.30) in (2.27) results in

$$\frac{\partial|\overline{E}|}{\partial x}sin\alpha + |\overline{E}|\frac{\partial sin\alpha}{\partial x} - \frac{\partial|\overline{E}|}{\partial y}cos\alpha - |\overline{E}|\frac{\partial cos\alpha}{\partial x} = -j\omega B_{pz}. \qquad (2.31)$$

In (2.31), α and B_{pz} are known distributions, whereas $|\overline{E}|$ is an unknown distribution. Equation (2.31) is discretized by using finite difference method (FDM) [62]. Field of view (FOV) is divided into $N \times N$ pixels. Central difference is used for the pixels that are not located at the boundary of the slice to be imaged. For the pixels located at the left and the upper boundary of the slice, forward difference is used. For the pixels located at the right and the lower boundary of the slice, backwards difference is used. As a result, a matrix equation is obtained as

$$[A]_{N^2 \times N^2}\begin{bmatrix} |\overline{E_1}| \\ |\overline{E_2}| \\ \vdots \\ |\overline{E_{N^2}}| \end{bmatrix}_{N^2 \times 1} = -\omega\begin{bmatrix} B_{p1} \\ B_{p2} \\ \vdots \\ B_{pN^2} \end{bmatrix}_{N^2 \times 1}, \qquad (2.32)$$

where the sub-indices $1, 2, \dots N^2$ represent a pixel inside FOV. $|\overline{E}|$ is calculated

by solving (2.32). σ value in a specific pixel is reconstructed by using the Ohm's Law as

$$\sigma(i,j) = \frac{|\bar{J}_{LF}(i,j)|}{|\bar{E}(i,j)|}, \qquad (2.33)$$

where (i,j) are the pixel indices. $\sigma(i,j)$ values reconstructed with (2.33) may approach to infinity if $|\bar{E}(i,j)|$ values approach to zero. In order to avoid this situation, $|\bar{E}(i,j)|$ is limited by using

$$|\bar{E}(i,j)| = \epsilon_{lim}, if \; |\bar{E}(i,j)| \leq \epsilon_{lim}, \qquad (2.34)$$

where ϵ_{lim} is the lower limit of $|\bar{E}(i,j)|$ values. The reconstruction method expressed in (2.22-2.34) is called as E-calculation algorithm since the proposed method is based on the calculation of $|\bar{E}|$.

2.2.3 J-derivative Algorithm

The relationship between E_x, E_y and B_{pz} is shown in (2.27). By using the Ohm's Law, (2.27) can be expressed in terms of resistivity (ρ), J_x, and J_y as

$$\frac{\partial}{\partial x}(\rho J_y) - \frac{\partial}{\partial y}(\rho J_x) = -j\omega B_{pz}. \qquad (2.35)$$

Assuming homogenous ρ distributions, (2.35) can be expressed as

$$\rho\left(\frac{\partial J_y}{\partial x} - \frac{\partial J_x}{\partial y}\right) = -j\omega B_{pz}. \qquad (2.36)$$

20

ρ can be reconstructed by using J_x and J_y distributions calculated with (2.23-2.24) and readily known B_{pz} distribution. σ is reconstructed by using

$$\sigma = \rho^{-1} \tag{2.37}$$

at each pixel inside the FOV. Since σ is reconstructed by using the spatial derivatives of J_x and J_y, the name of the proposed image reconstruction method is chosen as J-derivative algorithm.

J-derivative algorithm can be expanded to anisotropic conductivity distributions ($\underline{\sigma}$). Let us consider a $\underline{\sigma}$ distribution as a tensor of four elements as

$$\underline{\sigma} = \begin{bmatrix} \sigma_{xx} & \sigma_{xy} \\ \sigma_{yx} & \sigma_{yy} \end{bmatrix}. \tag{2.38}$$

By choosing $\sigma_{xy} = \sigma_{yx}$, the resistivity tensor ($\underline{\rho}$) can be expressed as

$$\underline{\rho} = \begin{bmatrix} \rho_{xx} & \rho_{xy} \\ \rho_{xy} & \rho_{yy} \end{bmatrix} = \underline{\sigma}^{-1} = \begin{bmatrix} \sigma_{xx} & \sigma_{xy} \\ \sigma_{xy} & \sigma_{yy} \end{bmatrix}^{-1}. \tag{2.39}$$

By using the Ohm's Law, the relationship between $\overline{E}$ and $\overline{J}_{LF}$ can be expressed as

$$\begin{bmatrix} E_x \\ E_y \end{bmatrix} = \begin{bmatrix} \rho_{xx} & \rho_{xy} \\ \rho_{xy} & \rho_{yy} \end{bmatrix} \begin{bmatrix} J_x \\ J_y \end{bmatrix}. \tag{2.40}$$

Substituting (2.40) in (2.35) results in

$$\frac{\partial}{\partial x}\left(\rho_{xy}J_x + \rho_{yy}J_y\right) - \frac{\partial}{\partial y}\left(\rho_{xx}J_x + \rho_{xy}J_y\right) = -\omega B_{pz}. \qquad (2.41)$$

Neglecting the spatial derivatives of ρ, (2.41) can be expressed as

$$-\frac{\partial J_x}{\partial y}\rho_{xx} + \left(\frac{\partial J_x}{\partial x} - \frac{\partial J_y}{\partial y}\right)\rho_{xy} + \frac{\partial J_y}{\partial x}\rho_{yy} = -\omega B_{pz}, \qquad (2.42)$$

where ρ_{xx}, ρ_{xy}, and ρ_{yy} are three unknown distributions. In order to reconstruct the unknown distributions, two equations are necessary in addition to (2.42). These additional equations should be linearly independent. For this requirement, three coils that have linearly independent B_{pz} distributions are necessary. For an ICMREIT system including three linearly independent coil structures and the $(i,j)^{th}$ pixel inside FOV, an equation system can be obtained as

$$-\frac{\partial J_{x1}(i,j)}{\partial y}\rho_{xx}(i,j) + \left(\frac{\partial J_{x1}(i,j)}{\partial x} - \frac{\partial J_{y1}(i,j)}{\partial y}\right)\rho_{xy}(i,j) + \frac{\partial J_{y1}(i,j)}{\partial x}\rho_{yy}(i,j) = -j\omega B_{pz1}(i,j)$$

$$-\frac{\partial J_{x2}(i,j)}{\partial y}\rho_{xx}(i,j) + \left(\frac{\partial J_{x2}(i,j)}{\partial x} - \frac{\partial J_{y2}(i,j)}{\partial y}\right)\rho_{xy}(i,j) + \frac{\partial J_{y2}(i,j)}{\partial x}\rho_{yy}(i,j) = -j\omega B_{pz2}(i,j),$$

$$-\frac{\partial J_{x3}(i,j)}{\partial y}\rho_{xx}(i,j) + \left(\frac{\partial J_{x3}(i,j)}{\partial x} - \frac{\partial J_{y3}(i,j)}{\partial y}\right)\rho_{xy}(i,j) + \frac{\partial J_{y3}(i,j)}{\partial x}\rho_{yy}(i,j) = -j\omega B_{pz3}(i,j)$$

$$(2.43)$$

where the sub-indices $k = 1,2,3$ represent the distributions of three linearly independent coil structures. In matrix form, (2.43) can be expressed as

$$[A_{ij}]_{3\times3}\left[\overline{\rho_{ij}}\right]_{3\times1} = -j\omega\left[\overline{b_{ij}}\right]_{3\times1}. \qquad (2.44)$$

A_{ij}, $\overline{\rho_{ij}}$, and $\overline{b_{ij}}$ can be expressed as

$$[A_{ij}] = \begin{bmatrix} -\dfrac{\partial J_{x1}\,(i,j)}{\partial y} & \left(\dfrac{\partial J_{x1}\,(i,j)}{\partial x} - \dfrac{\partial J_{y1}\,(i,j)}{\partial y}\right) & \dfrac{\partial J_{y1}\,(i,j)}{\partial x} \\[2mm] -\dfrac{\partial J_{x2}\,(i,j)}{\partial y} & \left(\dfrac{\partial J_{x2}(i,j)}{\partial x} - \dfrac{\partial J_{y2}\,(i,j)}{\partial y}\right) & \dfrac{\partial J_{y2}\,(i,j)}{\partial x} \\[2mm] -\dfrac{\partial J_{x3}\,(i,j)}{\partial y} & \left(\dfrac{\partial J_{x3}\,(i,j)}{\partial x} - \dfrac{\partial J_{y3}(i,j)}{\partial y}\right) & \dfrac{\partial J_{y3}\,(i,j)}{\partial x} \end{bmatrix}, \qquad (2.45)$$

$$\left[\overline{\rho_{ij}}\right] = [\rho_{xx}(i,j) \quad \rho_{xy}(i,j) \quad \rho_{yy}(i,j)]^{T}, \qquad (2.46)$$

and

$$\left[\overline{b_{ij}}\right] = [B_{pz1}(i,j) \quad B_{pz2}(i,j) \quad B_{pz3}(i,j)]^{T}. \qquad (2.47)$$

$\underline{\rho}$ and $\underline{\sigma}$ are calculated by using (2.39) after the calculation of $\overline{\rho_{ij}}$ as a result of the solution of (2.44) at each pixel inside the FOV.

2.3 An MRI Pulse Sequence for the Experimental Realization of ICMREIT

In recent experimental studies, feasibility of ICMREIT is investigated by using conventional spin-echo [53, 55] and gradient-echo [54] MRI pulse sequences. These pulse sequences include a single gradient pulse for inducing $\overline{J}_{LF}$ in a volume conductor, which results in a small period of time (T_c) for the accumulation of Φ_{LF} in MR signal. Since Φ_{LF} is directly related with T_c as expressed in (1.1), the MRI pulse sequences given in [53-55] are not capable of accumulating measurable Φ_{LF} in MR signal as the authors express. In this study, it is aimed to design and implement an MRI pulse sequence for ICMREIT which includes multiple gradient and suitable 180° refocusing RF pulses in order to accumulate measurable Φ_{LF} in MR signal [63-65] as shown in Figure 2.2.
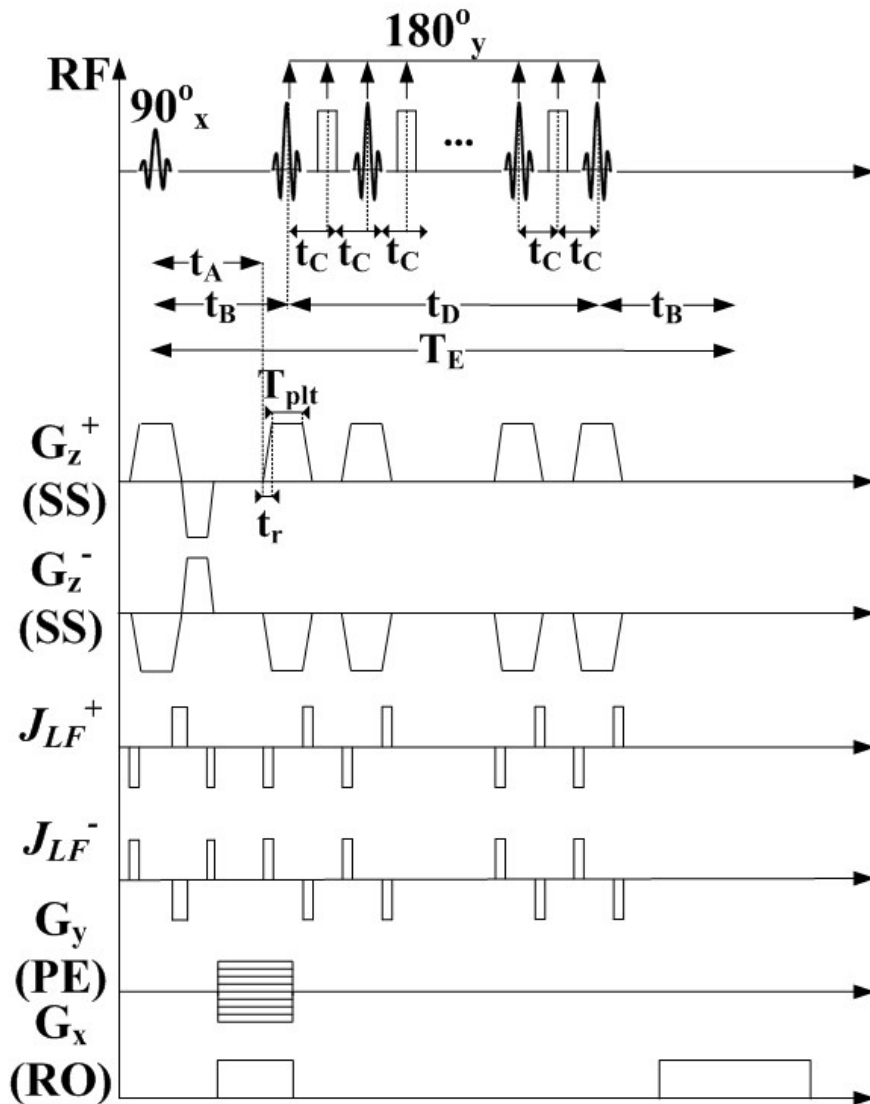
Figure 2.2 An MRI pulse sequence for the experimental realization of ICMREIT. SS, PE, and RO refer to slice selection, phase encoding and read-out, respectively [64-65].

The MRI pulse sequence shown in Figure 2.2 aims to form a spin echo. At first, spins are selectively excited with a 90° RF pulse which is followed by a periodic and monopolar gradient waveform (G_z) applied to the slice selection

(z) gradient coil of the MRI scanner after an interval of t_A [63-65]. In general, the periodic gradient waveform in Figure 2.2 can be applied to x, y, or z-gradient coils separately or the waveform can be applied to x-y, y-z, x-z, and x-y-z, pairs together [63]. The magnitude of G_z waveform is determined by considering the slice thickness (ST). In order to prevent phase cancellation effects of the $\bar{J}_{LF}$ pulses induced in the object during the ramps (t_r) of G_z waveform, soft 180° RF pulses are applied in the middle of the plateau (T_{plt}) of each gradient pulse and hard 180° RF pulses are applied after the gradient pulses. Since the interval between the soft and the hard 180° RF pulses (t_C) is much smaller than the interval between the 90° and the first 180° RF pulse (t_B), spin echoes are not formed during the interval of repetitive 180° RF pulses (t_D) [64-65]. Odd number of 180° RF pulses is used in order to form a measurable spin echo after an interval of t_B following the last 180° RF pulse [44, 63-65]. Echo signal is read-out at echo-time (T_E) which can be expressed as

$$T_E = 2t_B + t_D. \tag{2.48}$$

Φ_{LF} accumulated during the G_z waveform can be expressed as

$$\Phi_{LF} = (N_{cycle} + 1)\gamma\, B_{sz\_peak} T_s, \tag{2.49}$$

where N_{cycle} is the number of cycles of the gradient waveform, ($N_{cycle} + 1$) is the number of soft 180° RF pulses including the refocusing RF pulse of the conventional spin-echo pulse sequence, B_{sz_peak} is the peak value of B_{sz}, and $T_s = 2 \times t_r$ is the duration of $\bar{J}_{LF}$ pulses in a single cycle of G_z waveform [64-65]. As shown in (2.49), sensitivity of Φ_{LF} measurements increases as a function of N_{cycle} which results in increased t_D interval. Due to the refocusing

of spins by repetitive 180° RF pulses, transverse relaxation during t_D is limited. However, increased t_D interval reduces the magnitude of MR signal and signal to noise ratio (SNR) due to the longitudinal relaxation effects, which may be a severe problem for in-vivo applications [65]. It could be concluded that there is a tradeoff between signal quality and sensitivity of Φ_{LF} measurements.

Total phase (Φ) obtained as a result of the proposed pulse sequence is composed of the phase related with RF pulses (Φ_{RF}) and Φ_{LF}. In order to measure Φ_{LF}, the proposed pulse sequence is applied twice with G_z^+ and G_z^- waveforms which results in Φ^+ and Φ^- distributions, respectively. In both applications, the same number of RF and gradient pulses is applied. Therefore, the contribution of Φ_{RF} to Φ^+ and Φ^- is the same. Similarly, Φ_{LF} components of Φ^+ and Φ^- have the same magnitude. However, the polarity of Φ_{LF} components of Φ^+ and Φ^- is opposite of each other. Considering these facts, Φ^+ and Φ^- can be expressed as

$$\Phi^+ = \Phi_{RF} + \Phi_{LF} \tag{2.50}$$

and

$$\Phi^- = \Phi_{RF} - \Phi_{LF}. \tag{2.51}$$

Using (2.50-2.51), Φ_{LF} and Φ_{RF} can be calculated as

$$\Phi_{LF} = \frac{\Phi^+ - \Phi^-}{2} \tag{2.52}$$

and

$$\Phi_{RF} = \frac{\Phi^+ + \Phi^-}{2}. \tag{2.53}$$

2.4 Summary

In this chapter, forward and inverse problems of ICMREIT are described by using Maxwell's equations. Forward problem of ICMREIT is described as the calculation of B_{sz} distribution throughout a volume conductor object due to the excitation of a nearby coil with time varying electrical current. A 3D geometry is considered for the description of the forward problem and the mathematical derivation is performed by using Ampere's Law, A-V formulation, and temporal gauge, as shown in (2.1-2.6). In the end, a differential equation that relates $\bar{\bar{A}}$ with the known distributions of the forward problem is obtained as shown in (2.7). In order to solve the differential equation shown in (2.7), it is proposed to use the magnetic insulation type boundary condition as shown in (2.8). By this way, a BVP is obtained as shown in (2.7-2.8) and this BVP is defined and solved in a FEM solver, COMSOL Multiphysics 5.1 (COMSOL AB, Sweden). After the solution of the BVP for $\bar{\bar{A}}$, $\bar{E}$, $\bar{B}$ and $\bar{J}_{LF}$ are calculated by using (2.3-2.6) and (2.9).

$\bar{B}$ obtained as a result of the solution of the BVP shown in (2.7-2.8) represents the full magnetic flux density distribution which can be expressed as the summation of $\bar{B}_p$ and $\bar{B}_s$ as shown in (2.10). In order to extract B_{sz}, two simulations are performed in which σ distributions of the object is made equal to the true σ value and zero. By subtracting z components of the resultant $\bar{B}$ distributions obtained from the two simulations, B_{sz} is extracted. In order to inspect the reliability of the numerical solution, a semi-analytical solution is derived for a simple cylindrical geometry as shown in (2.11-2.13).

Inverse problem of ICMREIT is described as the reconstruction of σ

distributions of the object by using B_{sz} measurements and readily known B_{pz} distribution. The inverse problem is derived by using Ampere's and Faraday's laws with the conservation of magnetic flux, and a vector identity as shown in (2.14-2.19). In order to solve the inverse problem, E-calculation and J-derivative image reconstruction algorithms are proposed.

E-calculation algorithm is based on the calculation of the angle between x and y components of $\bar{J}_{LF}$ and $\overline{E}$, as shown in (2.26). By using the angle and $|\overline{E}|$ definitions with the z component of Faraday's Law, a differential equation that relates $|\overline{E}|$ with the measured and readily known distributions is obtained as shown in (2.31). The differential equation shown in (2.31) is discretized by using FDM and solved for $|\overline{E}|$. In the final step, σ is reconstructed by using the Ohm's Law as shown in (2.33). E-calculation algorithm does not use homogenous σ distribution assumption ($\nabla\sigma = 0$). Therefore, it will not suffer from boundary artifacts related with $\nabla\sigma = 0$ assumption. E-calculation algorithm is based on the calculation of $|\overline{E}|$ by utilizing the inverse of an $[A]_{N^2 \times N^2}$ matrix which depends on the B_{sz} measurements. The condition number of $[A]_{N^2 \times N^2}$ may increase for small and noisy B_{sz} measurements. For taking the inverse of $[A]_{N^2 \times N^2}$ matrices with high condition numbers, regularization methods should be utilized instead of direct inversion.

J-derivative algorithm expresses the relationship between the x and y components of $\bar{J}_{LF}$ and $\overline{E}$ by using the Ohm's Law and uses the z component of Faraday's Law in order to obtain the relationship between ρ with the measured and readily known distributions as shown in (2.35). By using $\nabla\sigma = 0$ assumption, J-derivative algorithm proposes to reconstruct ρ with a simple

scalar equation shown in (2.36). In the final step, σ is reconstructed by using the reciprocal of ρ at each pixel inside the FOV, as shown in (2.37). As shown in (2.38-2.47), J-derivative algorithm can be expanded to anisotropic σ reconstructions by using coil configurations with linearly independent B_{pz} distributions. $\nabla\sigma = 0$ assumption of the J-derivative algorithm results in boundary artifacts around the inhomogeneities. However, the simple structure of the algorithm may provide robust response for small and noisy B_{sz} measurements.

After the forward and inverse problems, an MRI pulse sequence is proposed for the experimental realization of ICMREIT, as shown in Figure 2.2. The proposed MRI pulse sequence is based on spin-echo and includes multiple SS gradient and 180° RF pulses. By locating the gradient and 180° RF pulses strategically, Φ_{LF} is accumulated in MR images. Φ_{LF} accumulation interval of the proposed MRI pulse sequence for ICMREIT is much greater than the recently proposed spin-echo based MRI pulse sequences for ICMREIT [53, 55], since it includes multiple SS gradient and 180° RF pulses. Large Φ_{LF} accumulation interval can be considered as a distinctive property of the proposed MRI pulse sequence for ICMREIT.

29

CHAPTER 3

METHODS

3.1 Numerical Simulations

Simulation models for z-gradient and y-gradient coils are created by using a FEM solver, COMSOL Multiphysics 5.1 (COMSOL AB, Sweden) and shown in Figure 3.1. The z-gradient coil shown in Figure 3.1 (a) is adapted from the model proposed by Tas [66] and composed of 24 infinitely thin circular coils with a diameter of 70 cm. Locations and excitation current polarities of the circular coils are listed in Table 3.1. The z-gradient coil shown in Figure 3.1 (a) is excited with sinusoidally varying electrical current which has a magnitude of 87.6 A and a frequency (f) of 1 kHz. Gradient strength (GS) of the z-gradient coil is 4.8 mT/m along the z-axis. f is determined by considering the gradient waveforms shown in Figure 3.2 and the slew rate (SR) of the utilized MRI scanner (MAGNETOM Trio, Siemens AG, Erlangen Germany). SR can be expressed as

$$SR = \frac{GS}{t_r} \tag{3.1}$$

where t_r is the ramp time of a gradient pulse as shown in Figure 3.2 (a).
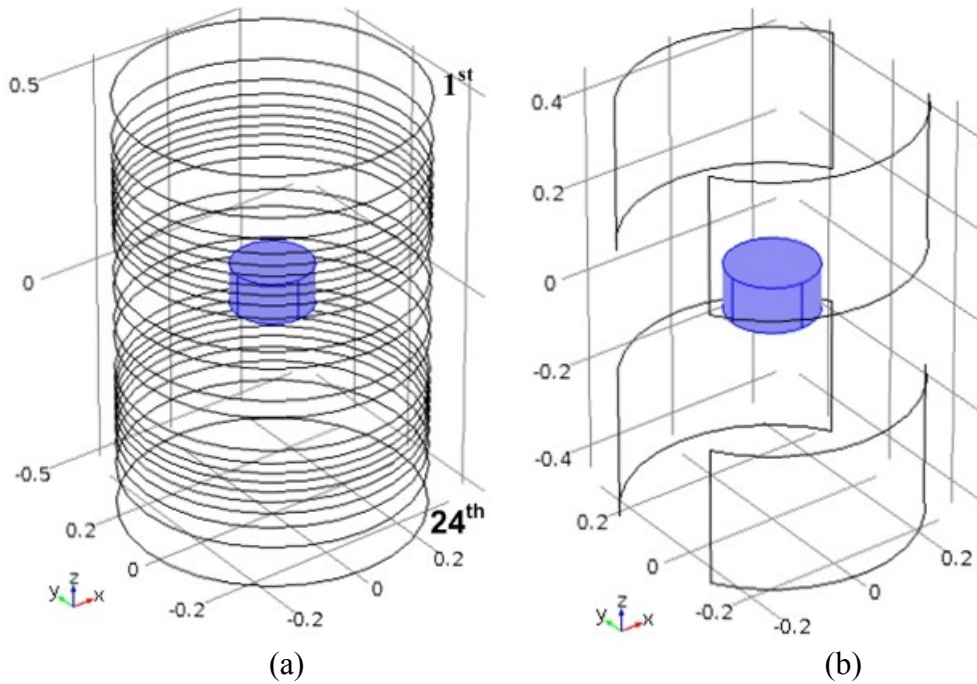
Figure 3.1 Simulation models for z-gradient (a) and y-gradient (b) coils around cylindrical conductors.

At 1 kHz, the period (T) of a sinusoidal gradient is 1 ms. If T is approximated with $4 \times t_r$ as shown in Figure 3.2 (b), $t_r = 250$ µs is obtained. Considering the calculated GS of 4.8 mT/m and $t_r = 250$ µs, SR is calculated as 19.2 T/m/s which is smaller than the maximum SR of 170 T/m/s for the utilized MRI scanner.

The y-gradient coil shown in Figure 3.1 (b) is composed of four infinitely thin saddle coils, the centers of which are located at $z = 20$ cm $z = -20$ cm planes. Height and length of each saddle coil are 30 cm and 20π cm, respectively. Direction of the excitation current of the y-gradient coil is CW and CCW for the saddle coils located in $y > 0$ and $y < 0$ regions.

Table 3.1 Locations and excitation current polarities of the components of the
z-gradient coil shown in Figure 3.1.

Coil No	Location on z axis (cm)	Polarity of excitation current	Coil No	Location on z axis (cm)	Polarity of excitation current	Coil No	Location on z axis (cm)	Polarity of excitation current
1	-52.8	CW	9	-.20.0	CW	17	22.5	CCW
2	-41.7	CW	10	-16.7	CW	18	24.9	CCW
3	-36.5	CW	11	-8.4	CCW	19	27.3	CCW
4	-32.9	CW	12	-4.1	CCW	20	29.9	CCW
5	-29.9	CW	13	4.1	CW	21	32.9	CCW
6	-27.3	CW	14	8.4	CW	22	36.5	CCW
7	-24.9	CW	15	16.7	CCW	23	41.7	CCW
8	-22.5	CW	16	20.0	CCW	24	52.8	CCW

Note: CW and CCW are referred to as clockwise and counter clockwise
directions, respectively. Locations and excitation current polarities of the
components of the z-gradient coil are adapted from the model proposed by Tas
[66].
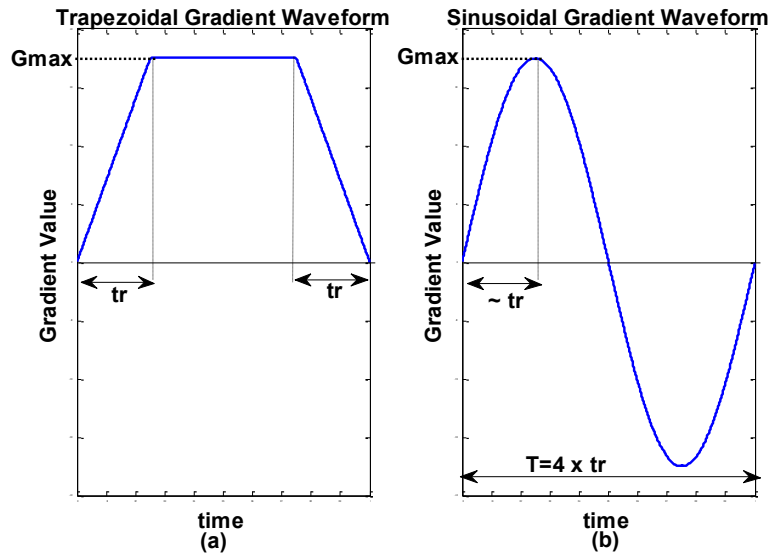
Figure 3.2 Trapezoidal (a) and sinusoidal (b) gradient waveforms.

The y-gradient coil shown in Figure 3.1 (b) is excited with sinusoidally varying electrical current which has a magnitude of 716.6 A and a frequency of 1 kHz. *GS* of the y-gradient coil along the y-axis is 4.8 mT/m.

Phantom models used in simulations are shown in Figure 3.3.

(a)   (b)   (c)
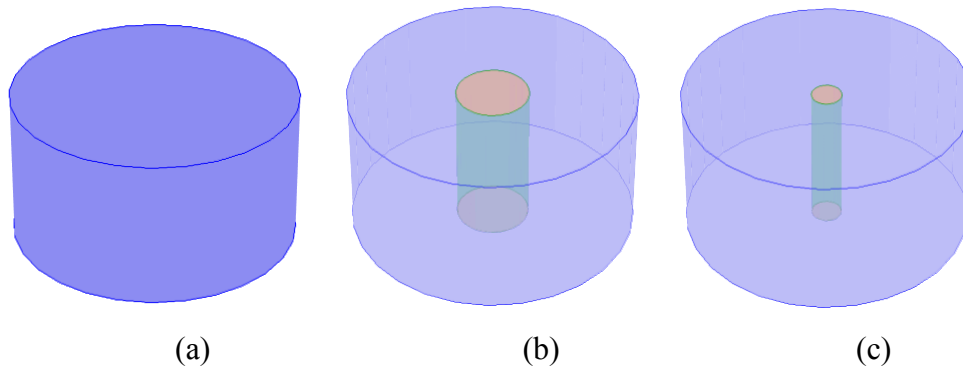
Figure 3.3 Cylindrical phantoms with uniform (a) and inhomogenous (b-c) σ distributions.

As shown in Figure 3.3, cylindrical phantom models are used in the simulations. Height and diameter of the cylinders are 10 cm and 19 cm, respectively. All of the phantoms have isotropic σ and ε distributions. As shown in Figure 3.3 (a), the first phantom, which is referred to as Phantom 1, is a uniform cylinder with a σ value of 1 S/m. As shown in Figure 3.3 (b-c), cylindrical inhomogeneities with two different diameters are located inside the second and the third phantoms, respectively. Diameters of the large and the small inhomogeneities shown in Figure 3.3 (b-c) are 4.8 cm and 2 cm, respectively. Height of both inhomogeneities is 10 cm. The large and the small inhomogeneities are located at four different positions inside the second and the third phantoms, respectively. The second and the third phantoms including the large and the small inhomogeneities are referred to as Phantom 2a-d and

34

Phantom 3a-d, respectively. ε_r value of the phantoms is 78.4. Properties of the phantoms are listed in Table 3.2.

Table 3.2 Properties of the simulation phantoms.

Phantom	d_{ih} (mm)	Δx_{ph-ih} (mm)	σ_b (S/m)	σ_{ih} (S/m)
1	-	-	1	-
2a	48	2.75	0.75	0.45
2b	48	60.7	0.75	0.45
2c	48	19.2	0.75	1.2
2d	48	48.2	0.75	1.2
3a	20	2.75	0.75	0.45
3b	20	60.7	0.75	0.45
3c	20	19.2	0.75	1.2
3d	20	48.2	0.75	1.2

Note: d_{ih}, Δx_{ph-ih}, σ_b, and σ_{ih} refer to diameter of the inhomogeneity, distance between the center of the phantom and the inhomogeneity, σ value of the background and the inhomogeneity, respectively.

Simulation models are created by using the gradient coils shown in Figure 3.1 and the phantoms listed in Table 3.2. Phantoms are located between $z = 0$ and $z = 10$ cm planes, as shown in Figure 3.1. Simulation data is obtained for the transverse slice located at $z = 9$ cm. FOV is 25×25 cm^2 and divided into 128×128 pixels. B_{pz} values of the z-gradient coil change between $0 \leq B_{pz} \leq 0.48$ mT for $0 \leq z \leq 10$ cm which results in a GS value of 4.8 mT/m. On the selected slice, B_{pz} values of the z-gradient coil are close to 0.43 mT and B_{pz} values of the y-gradient coil change between

-0.456 $\leq B_{pz} \leq$ 0.456 mT, for -9.5 $\leq y \leq$ 9.5 cm which results in a *GS* value of 4.8 mT/m.

Z-gradient coil is used with all of the phantoms listed in Table 3.2. Y-gradient coil is used with Phantom 1. Coil and phantoms are located in an air filled spherical domain with a diameter of 1.6 m and extended to infinite element domain with a pole distance of 2.77 m in order to prevent boundary reflections [58-59, 65]. During the simulations, σ value of air filled domain cannot be made zero since the zero conductivity distributions result in singular computation matrices and non-convergent solutions. In this study, σ value of air is taken as 0.001 S/m in order have convergent solutions [51]. The selected air conductivity value of 0.001 S/m does not affect the calculations, since it is 1000 and 750 times smaller than the σ_b values of the uniform and the inhomogeneous phantoms, respectively. Simulation models are meshed adaptively by using edge, triangular, and tetrahedral elements. Solution is obtained iteratively by using "Magnetic Fields" interface of the AC-DC module of COMSOL 5.1 (COMSOL AB Sweden). Flexible generalized mean residual algorithm with a residual of 10^{-2} is utilized for the iterative solutions. Maximum and minimum element size values of the models are 30.4 cm and 2.4 mm, respectively. Number of elements (N_e), number of iterations (N_i) for the solutions to converge, and degrees of freedoms (DOF) solved for the simulation models are listed in Table 3.3.

B_{sz} and $\overline{J}_{LF}$ distributions are obtained by solving the BVP shown in (2.7-2.8) and using (2.9) for simulation model 1 as shown in Table 3.3. Reliability of the numerical solution is investigated by comparing $\overline{J}_{LF}$ distributions obtained from the numerical simulations and the semi-analytical solution of the forward problem shown in (2.12).

36

Table 3.3 Parameters of the numerical simulation models.

Model	Coil	Ph.	N_e			N_i	DOF
			N_{edge}	N_{tri}	N_{teth}		
1	z	1	1161	1200	24202	43	285230
2a	z	2a	1238	1896	30921	49	363670
2b	z	2b	1248	2020	30566	43	359570
2c	z	2c	1254	2026	31979	42	376170
2d	z	2d	1250	1988	31584	43	371430
3a	z	3a	1254	2000	32400	49	381020
3b	z	3b	1263	2020	32918	43	387070
3c	z	3c	1263	2048	33071	49	388820
3d	z	3d	1256	1986	32501	44	382230
4	y	1	325	1462	12940	20	100439

Note: $N_{edge}, N_{tri}, N_{teth}$ refer to the number of edge, triangular, and tetrahedral elements, respectively.

Φ_{LF} distributions are reconstructed by using the calculated B_{sz} distributions and (2.49). In Φ_{LF} calculations, $N_{cycle} = 20$ and $T_s = 600$ µs are considered for the MRI pulse sequence proposed for ICMREIT shown in Figure 2.2.

Scott et al. report SNR levels varying between 50-60 dB for injected current related MR phase measurements in MRCDI [20]. We consider these SNR values in our study and add Gaussian noise to the simulated Φ_{LF} distributions at SNR= 50 dB and 60 dB. J_x and J_y distributions can be reconstructed by using the Φ_{LF} distributions, (2.23-2.24) and (2.49) as

$$J_x = \frac{1}{\mu_o}\frac{\partial B_{sz}}{\partial y} = \frac{1}{\mu_o[(N_{cycle}+1)\gamma\,T_s]}\frac{\partial \Phi_{LF}}{\partial y} \qquad (3.2)$$

and

$$J_y = -\frac{1}{\mu_o}\frac{\partial B_{sz}}{\partial x} = -\frac{1}{\mu_o[(N_{cycle}+1)\gamma\ T_s]}\frac{\partial \Phi_{LF}}{\partial x}. \tag{3.3}$$

White noise is amplified by the derivatives in (3.2-3.3). Therefore, Φ_{LF} distributions are filtered by using the method shown in Figure 3.4, the first step of which is to obtain the geometric information by using the reference σ distributions (σ_{ref}) of the phantoms and an edge detection algorithm with Prewitt's method [65, 67]. B_{sz} is calculated by using Φ_{LF} and (2.49). A row and a column of Φ_{LF} is chosen and second order curve fitting is applied between the edge points of the chosen Φ_{LF} profiles. The choice of the curve fitting method can be explained by considering the semi-analytical solution of the forward problem, which is shown in (2.12) and that presents the linear relationship between $\bar{J}_{LF}$ and r. Considering the azimuthal angle (φ) and (2.12), J_x, J_y, x and y can be expressed as

$$J_x = \left|\bar{J}_{LF}\right|sin\varphi = \frac{1}{2}\,\omega\,r\,\sigma\,\left|B_{pz}\right|sin\varphi, \tag{3.4}$$

$$J_y = \left|\bar{J}_{LF}\right|cos\varphi = \frac{1}{2}\,\omega\,r\,\sigma\,\left|B_{pz}\right|cos\varphi, \tag{3.5}$$

$$x = rcos\varphi, \tag{3.6}$$

and

$$y = rsin\varphi. \tag{3.7}$$

Using (3.3, 3.5)

$$B_{sz} = -\mu_o \int J_y dx = -\frac{1}{2}\mu_o\omega\sigma\left|B_{pz}\right| \int rcos\varphi\ dx \tag{3.8}$$

is obtained.

38

Edge

Φ_{LF}

E_x

E_y

$1/\ (N_{cycle}+1)\ \gamma\ T_s$

B_{sz}

Take the ith row and the jth column and apply curve fitting between edge points

B_{sz}
Edge
$B_{sz\text{-}y}$

B_{sz} (nT)

y (cm)

B_{sz}
Edge
$B_{sz\text{-}x}$

B_{sz} (nT)

x (cm)

$B_{sz\text{-}y}$

$B_{sz\text{-}x}$

$1/\mu_o \times \partial\ (.)\ /\ \partial y$

J_x

$-1/\mu_o \times \partial\ (.)\ /\ \partial x$

J_y

Image Reconstruction Algorithm (J-derivative or E-Calculation)

σ_{rec}
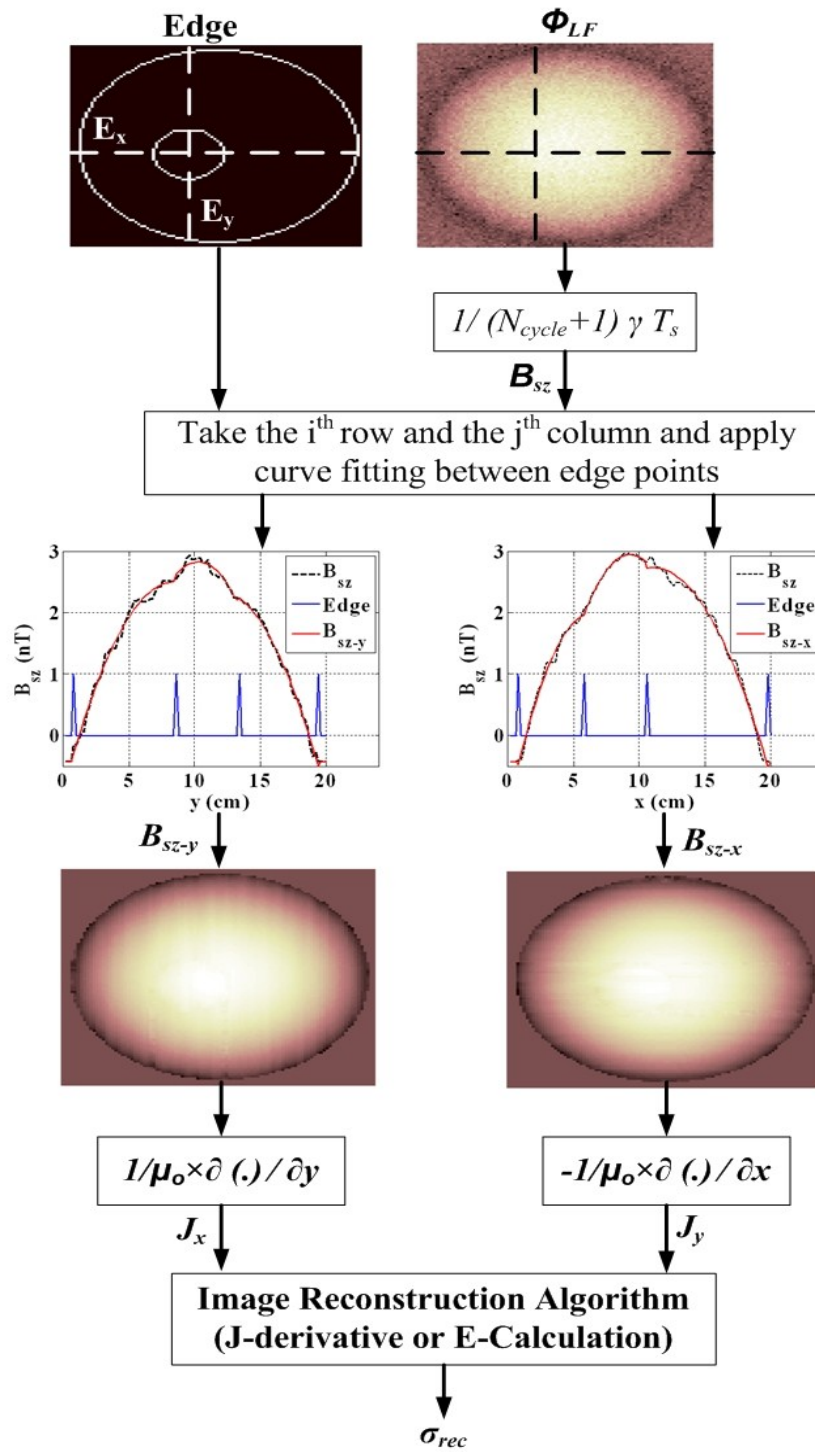
Figure 3.4 Denoising filter and image reconstruction process for ICMREIT [65]. σ_{rec} represents the reconstructed conductivity image.

Substituting (3.6) in (3.8) results in

$$B_{sz} = -\frac{1}{4}\mu_o \omega\sigma \left|B_{pz}\right| x^2 + C. \tag{3.9}$$

As shown in (3.9), horizontal B_{sz} profiles have second order characteristics. The analysis shown in (3.4-3.9) can be applied for the vertical B_{sz} profiles. Due to the quadratic relationship between B_{sz} profiles and spatial coordinates as shown in (3.9), B_{sz} profiles are fitted to a second order polynomial. The analysis shown in (3.4-3.9) is applicable for the z-gradient coil which has a relatively uniform B_{pz} distribution in the selected xy slice to be imaged. On the other hand, B_{pz} distribution of the y-gradient coil along y axis depends on y coordinates. Using this fact, (3.2), and (3.4), vertical B_{sz} profiles of the y-gradient coil can be obtained as

$$B_{sz} = -\mu_o \int J_x dy = \frac{1}{2}\mu_o \omega\sigma GS \int yr\sin\varphi \, dy. \tag{3.10}$$

Substituting (3.7) in (3.10) results in

$$B_{sz} = -\frac{1}{6}\mu_o \omega\sigma \, GS \, y^3 + C. \tag{3.11}$$

Considering (3.9, 3.11), horizontal (x) and vertical (y) B_{sz} profiles of the y-gradient coil are fitted to second order and third order polynomials, respectively. By filtering all of the rows and the columns of the B_{sz} distribution, filtered B_{sz} images in x (B_{sz-x}) and y directions (B_{sz-y}) are obtained. J_x and J_y distributions are calculated by using (3.2-3.3) with B_{sz-x} and B_{sz-y} images. By using the calculated J_x and J_y distributions with J-derivative and E-Calculation

algorithms, presented in the previous chapter, $\left|\bar{J}_{LF}\right|$ and σ_{rec} images are reconstructed. Conductivity reconstruction error (ϵ_σ) is calculated by using

$$\epsilon_\sigma = \sqrt{\frac{1}{N_p}\Sigma_{k=1}^{N_p}\frac{[\sigma(k)-\sigma_{rec}(k)]^2}{[\sigma(k)]^2}} \times 100\ \% ,\qquad (3.12)$$

where k is the pixel index, N_p is the number of pixels inside FOV, σ and σ_{rec} are the true and the reconstructed conductivity distributions, respectively [68]. By substituting true and reconstructed $\left|\bar{J}_{LF}\right|$ distributions instead of σ and σ_{rec} in (3.12), error of the reconstructed $\left|\bar{J}_{LF}\right|$ distributions (ϵ_J) is calculated.

3.2 Distinguishability and Sensitivity Analyses

Distinguishability and sensitivity analyses are performed in order to investigate imaging characteristics of ICMREIT [51]. For the analyses, simulation data is obtained from the z-gradient coil model presented in Figure 3.1 (a). Using the results obtained from the sensitivity and the distinguishability analyses, feasibility of ICMREIT is evaluated [51].

Predicting the outputs of electrical impedance imaging (EII) systems quantitatively is a useful tool for evaluating the feasibility of the methods. Isaacson proposes distinguishability analysis in order to demonstrate the ability of injected current EIT systems to expose the conductivity difference of an inhomogeneity from the background and utilizes the analysis to optimize the current injection pattern [52, 69]. Seagar et al. demonstrate the limitations of EII systems by using the concepts of spatial resolution, conductivity resolution, and conductivity contrast [70]. Eyüboglu et al. [71] and Köksal et al. [72] use

distinguishability analysis in order to optimize coil excitation patterns for discrete coil ICEIT systems. In [52, 71-72], it is expressed that two conductivity distributions, σ_1 and σ_2 are distinguishable with a measurement precision of ϵ if and only if

$$\|V(\theta, \sigma_1) - V(\theta, \sigma_2)\| \geq \epsilon \qquad (3.13)$$

is satisfied. In (3.13), V is the surface electrical potential measured on the boundary of the conductors and θ is the angular position of the measurement electrode. Using (3.13), distinguishability function (D) [52, 70-71] is defined as

$$D = \|V(\theta, \sigma_1) - V(\theta, \sigma_2)\|. \qquad (3.14)$$

In MREIT and ICMREIT, the measured quantity is the MR phase due to B_z created by the injected or the induced current distributions. Considering B_z measurements, Altunel et al. describe D for MREIT [73] as

$$D = \|B_z(r, \theta, \sigma_1) - B_z(r, \theta, \sigma_2)\|, \qquad (3.15)$$

where (r, θ) are the coordinates in cylindrical coordinate system. Definition of (3.14) can be used for ICMREIT since the measured quantities of both MREIT and ICMREIT are the same [51]. The cross sectional geometries of the cylindrical conductors used in this study are shown in Figure 3.5. In Figure 3.5, P and ρ_{ih} are the radius of the conductors and the conductivity inhomogeneities, $\Delta\sigma$ is the difference between σ_b and σ_{ih}. Using the definition in (3.14), it can be expressed that a pixel of σ_2 and σ_3 are distinguishable from the same pixel of σ_1 with a measurement precision of ϵ if and only if
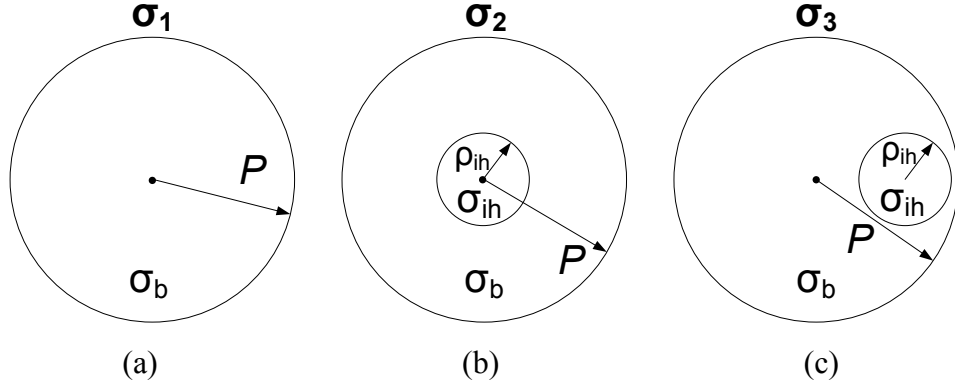
Figure 3.5 Cross sectional geometries of the cylindrical conductors. σ_1, σ_2, and σ_3 represent uniform (a) and inhomogeneous conductivity distributions with concentric (b) and eccentric (c) inhomogeneities [51].

$$|\Delta B_z(x,y)| = |B_z(x,y,\sigma_i) - B_z(x,y,\sigma_1)| > \epsilon, \ldots i = 1,2, or\ 3 \qquad (3.16)$$

is satisfied [51]. In (3.15), $|\cdot|$ is the absolute value function. Considering the inhomogeneities (ih) in Figure 3.5 (b-c) as

$$ih = \{(x_1,\ y_1),\ (x_2,\ y_2), \ldots (x_N,\ y_N)\}, \qquad (3.17)$$

where $(x_i,\ y_i), i = 1,2, \ldots N$ represent the Cartesian coordinates of the pixels inside the inhomogeneity, it can be expressed that $\frac{M}{N} \times 100\,\%$ of the inhomogeneity is said to be distinguishable from the background if M pixels of the inhomogeneity satisfy (3.16). By this way, D can be described [51] as

$$D = \frac{M}{N} \times 100\,\%. \qquad (3.18)$$

For an inhomogeneity with a cross sectional area of S_{ih} and located at (x,y), the surface average of (3.16) can be expressed as

$$|\Delta B_z(x,y)|_{avg} = \frac{1}{S_{ih}} \int_{S_{ih}} |\Delta B_z(x,y)| \, dS. \tag{3.19}$$

If S_{ih} approaches to the area of a single pixel, (3.19) can be used as sensitivity measure of ICMREIT to a conductivity perturbation located at (x,y) [51].

In this study, the z-gradient coil presented in Figure 3.1 (a) is utilized. Coil current is adjusted such that B_{pz} value of the selected slice is 2 mT. The simulation objects have cylindrical shape with a diameter of 20 cm and a height of 10 cm [51]. In order to investigate sensitivity of ICMREIT, the center of a cylindrical conductivity inhomogeneity (C_{ih}) with a diameter of 1 cm and a height of 10 cm is located between $0 < x < 9$ cm as shown in Figure 3.6.
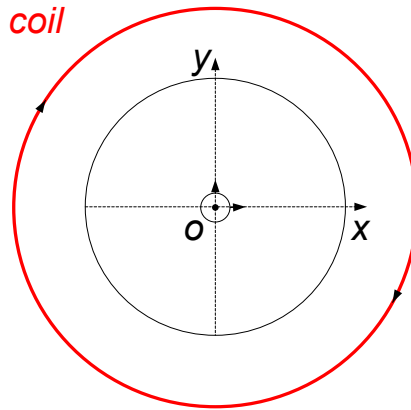
Figure 3.6 Cross sectional geometry of a z-gradient coil around a cylindrical conductor including a cylindrical inhomogeneity. A single component of the z-gradient coil is shown [51].

In sensitivity and distinguishability analyses, σ_b is 1 S/m. $\Delta\sigma$ is adjusted between $-0.999 \leq \Delta\sigma \leq 1$ S/m. Sensitivity of ICMREIT is investigated by using (3.19). Distinguishability analysis is performed by using (3.18) and the

same σ_b and $\Delta\sigma$ values used in sensitivity analyses. Height of σ_1, σ_2, σ_3 and the inhomogeneities is 10 cm. For σ_3, C_{ih} is located at $x = 4$ cm. ρ_{ih} is adjusted between $1 \le \rho_{ih} \le 9$ cm and $1 \le \rho_{ih} \le 5$ cm for σ_2 and σ_3, respectively. Sadleir et al. state that noise level (ϵ) of B_z measurements in MREIT experiments at 3T can be decreased to 0.25 nT, for a voxel size of $3 \times 3 \times 3$ mm^3 [74]. In this study, ϵ is chosen as 1 nT considering the measurement noise information given in [74].

3.3 Physical Experiments

In physical experiments, a Plexiglas cylindrical phantom with a diameter of 19 cm and a height of 10 cm is used as shown in Figure 3.7.
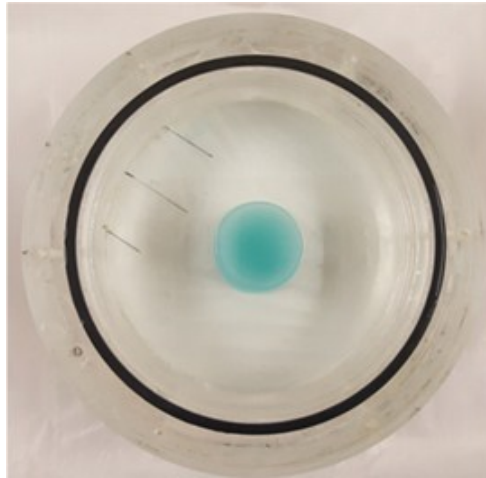
Figure 3.7 Top view of the experimental phantom used in ICMREIT experiments.

The phantom in Figure 3.7 is filled with liquid solutions composed of copper-sulfate (CuSO$_4$) and sodium-chloride (NaCl) dissolved in distilled water.

Cylindrical inhomogeneities in gel form and composed of Agarose, TX-151, CuSO$_4$, NaCl, and distilled water are located inside the phantom filled with liquid solutions. Diameter and height of the inhomogeneities are 4.8 cm and 10 cm, respectively. Properties of the solutions and the inhomogeneities are listed in Table 3.4.

Table 3.4 Properties of the solutions and the inhomogeneities.

Material	Distilled water (ml)	Agarose[1] (g)	TX-151[2] (g)	CuSO$_4$ (g)	NaCl (g)	σ (S/m)
Sltn. 1	100	-	-	0.05	0.67	0.83
Sltn. 2	100	-	-	0.05	1.2	1.48
Sltn. 3	100	-	-	0.05	0.55	0.75
Inh. 1	100	1	1	0.05	0.125	0.45
Inh. 2	100	1	1	0.05	0.8	1.2

Note: Sltn. and Inh. refer to the solution and the inhomogeneity.

[1] Agar bacteriological (Agar No. 1) LP0011B, Oxoid Limited, Hampshire, RG248PW, UK.

[2] TX 151 Solidifying powder, Balmar LLC, Lafayette, LA, 70507, USA.

As shown in Table 3.4, phantoms filled with Sltn.1 and Sltn. 2 are referred to as Phantom 1a and Phantom 1b, respectively. Phantom 1a-b do not include the inhomogeneities. Inh. 1 and Inh. 2 are located at four different positions inside the phantom filled with Sltn 3. These phantoms are referred to as Phantom 2a-2d. Properties of the experimental phantoms are listed in Table 3.5.

The experimental phantoms are located inside the MRI scanner as shown in Figure 3.8. As shown in Figure 3.8, the gradient iso-center is located at $z = 0.5$ cm and the selected slice is at $z = 9$ cm.

Table 3.5 Properties of the experimental phantoms.

Phantom	Components	Δx_{ph-ih} (mm)	σ_b (S/m)	σ_{ih} (S/m)
1a	Sltn. 1	-	0.83	-
1b	Sltn. 2	-	1.48	
2a	Sltn. 3 + Inh.1	2.75	0.75	0.45
2b	Sltn. 3 + Inh.1	60.7	0.75	0.45
2c	Sltn. 3 + Inh.2	19.2	0.75	1.2
2d	Sltn. 3 + Inh.2	48.2	0.75	1.2
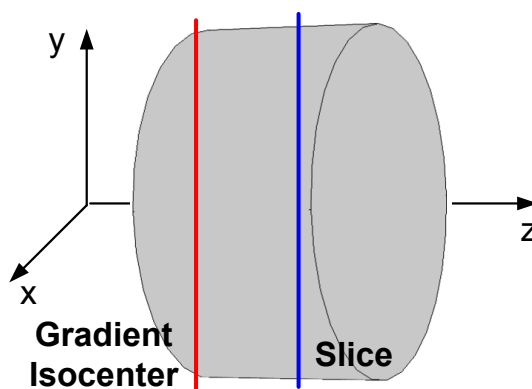
Figure 3.8 Location of the experimental phantoms inside the MRI scanner [65].

The MRI pulse sequence shown in Figure 2.2 is used for the experimental realization of ICMREIT. Properties of the MRI pulse sequence are summarized in Table 3.6. MR magnitude, Φ^+, and Φ^- images are acquired by using the proposed pulse sequence twice with G_z^+ and G_z^- waveforms. Φ_{LF} is obtained by using (2.52) and the acquired Φ^+ and Φ^- images. $|\bar{J}_{LF}|$ and σ_{rec} images are reconstructed by using the procedure shown in Figure 3.4.

Table 3.6 Properties of the MRI pulse sequence proposed for ICMREIT [65].

T_R (s)	N_{cycle}	t_r (µs)	GS (mT/m)	Image Slice	ST (mm)	FOV (cm×cm)	Spatial Sampling (pix×pix)
0.5	20	300	4.8	xy	5	25×25	128×128

Note: T_R, ST, and xy represent the pulse repetition rate, slice thickness, and transverse slice, respectively.

In the image reconstruction process, edge detection is performed by using the acquired MR magnitude images. ϵ_σ is calculated by using (3.12).

3.4 Summary

In this chapter, it is aimed to describe the simulation and experimental methods used in this thesis. At first, simulation models for z-gradient and y-gradient coils around homogeneous and inhomogeneous phantoms with a cylindrical shape are described. It is stated that the spatial derivatives of the measured B_{sz} distributions during the image reconstruction process will result in erroneous σ reconstructions due to the amplification of the noise. In order to reduce the effect of noise in measured B_{sz} distributions and reconstruct σ images with acceptable accuracy, a denoising filter based on edge detection and curve fitting is proposed as shown in Figure 3.4. Distinguishability and sensitivity analysis are described in order to evaluate the basic imaging characteristics of ICMREIT. Physical experiments are described by demonstrating the properties of the experimental set-up. At first, physical properties of the experimental phantoms are described. The location of the experimental phantoms, the gradient iso-center, and the image slice are shown

in Figure 3.8 and the properties of the proposed MRI pulse sequence for ICMREIT are listed in Table 3.6 in order to visualize the experimental set-up.

CHAPTER 4

RESULTS

4.1 Simulation Results

4.1.1 Simulation 1

In this simulation, model 1, which includes the z-gradient coil with Phantom 1, is used. By utilizing this model, it is aimed to exhibit the imaging characteristics of ICMREIT for the z-gradient coil around a uniform conductor. Φ_{LF} distribution and profile passing through the center of the selected slice are shown in Figure 4.1. As shown in Figure 4.1, characteristics of the horizontal Φ_{LF} profile are similar to a quadratic function. Slope of the Φ_{LF} profile increases towards the boundary of the phantom. Difference between the maximum and the minimum of Φ_{LF} ($\Delta\Phi_{LF}$) values is 12 mrad.

$|\bar{J}_{LF}|$ distributions obtained from the numerical and the semi-analytical solutions are shown in Figure 4.2. As shown in Figure 4.2, $|\bar{J}_{LF}|$ distributions obtained from the numerical and the semi-analytical solutions are almost the same. Error between the two solutions is close to zero.
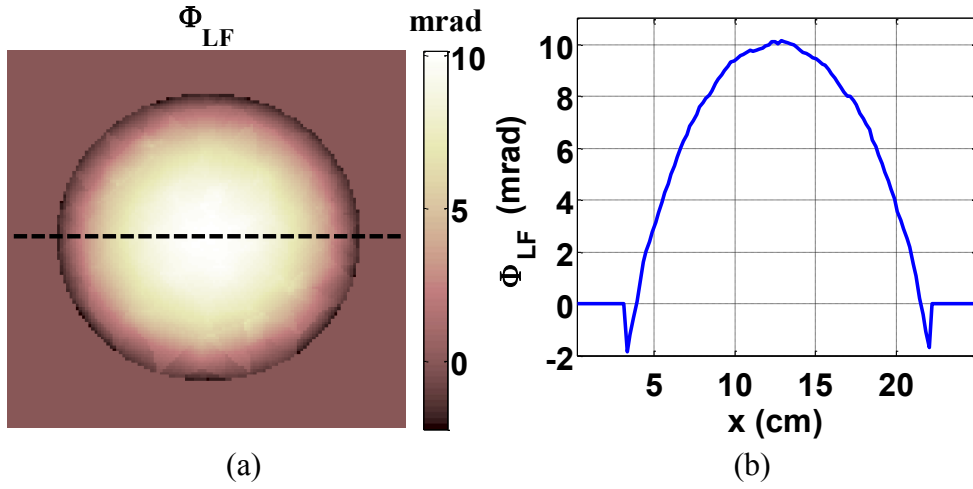
Figure 4.1 Φ_{LF} distribution (a) and profile (b) of model 1.

Due to the small error between the numerical and the semi-analytical solutions, $|\bar{J}_{LF}|$ distributions obtained from the numerical solution of the forward problem are taken as true distributions in the rest of this chapter. It is observed that there is a linear relationship between $|\bar{J}_{LF}|$ and r.

Reconstructed $|\bar{J}_{LF}|$ images and profiles of model 1 are shown in Figure 4.3. As shown in Figure 4.3, reconstructed $|\bar{J}_{LF}|$ values at SNR= 60 dB and SNR= 50 dB are close to the true $|\bar{J}_{LF}|$ values.

σ_{rec} images reconstructed with J-derivative and E-calculation algorithms are shown in Figure 4.4. As shown in Figure 4.4 (a, c, e), σ_{rec} values reconstructed with J-derivative algorithm are close to true σ values. Deviations from the true σ values are observed around the boundary of the selected slice. As shown in Figure 4.4 (b, d, f), σ_{rec} values reconstructed with E-calculation algorithm oscillate around the true σ values. Magnitude of the oscillations increases towards the boundary and the center of the selected slice.

52
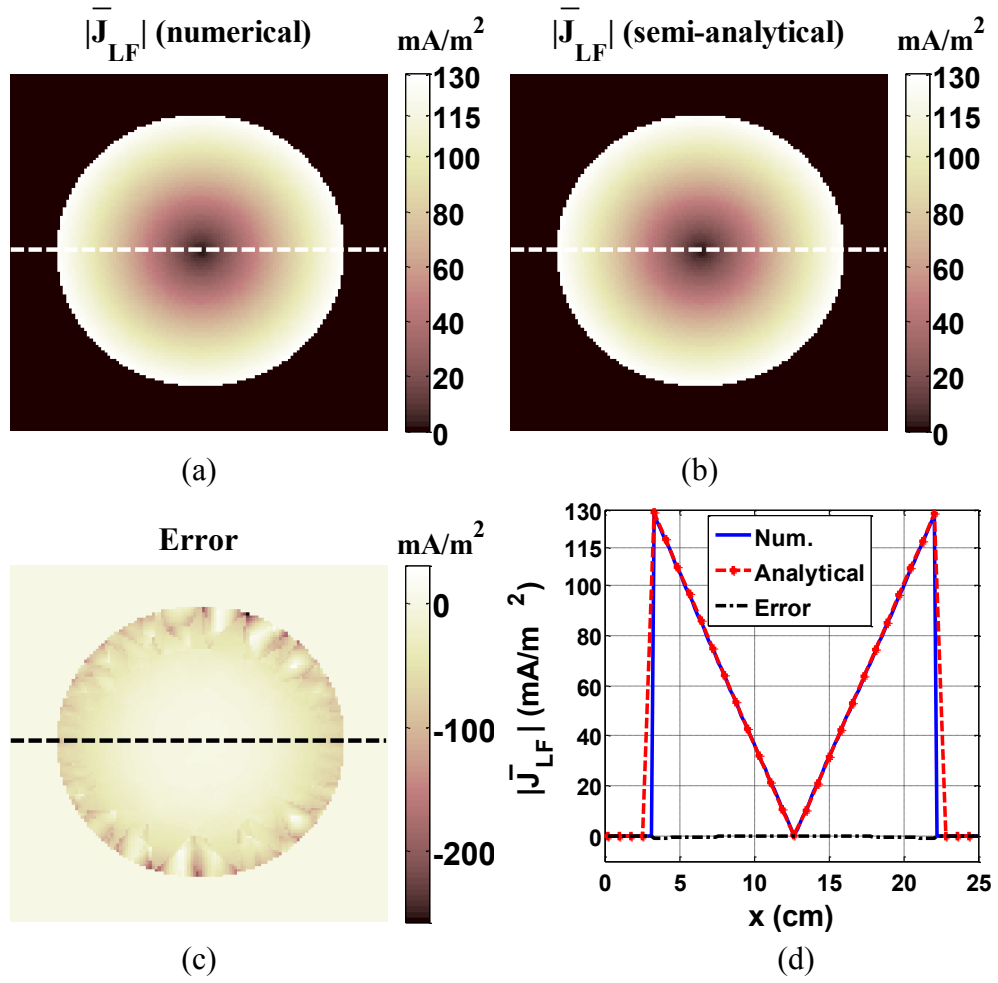
Figure 4.2 $\left|\bar{J}_{LF}\right|$ distributions obtained from the numerical (a) and the semi-analytical (b) solutions of the forward problem for model 1, error between the numerical and the semi analytical solutions (c), and horizontal $\left|\bar{J}_{LF}\right|$ profiles passing through the selected slice (d).

$\Delta\Phi_{LF}$, maximum (max), and average (avg) values of the true $\left|\bar{J}_{LF}\right|$ ($\left|\bar{J}_{LF}\right|_{max}$ and $\left|\bar{J}_{LF}\right|_{avg}$) distribution, ϵ_J, and ϵ_σ values of model 1 are listed in Table 4.1.
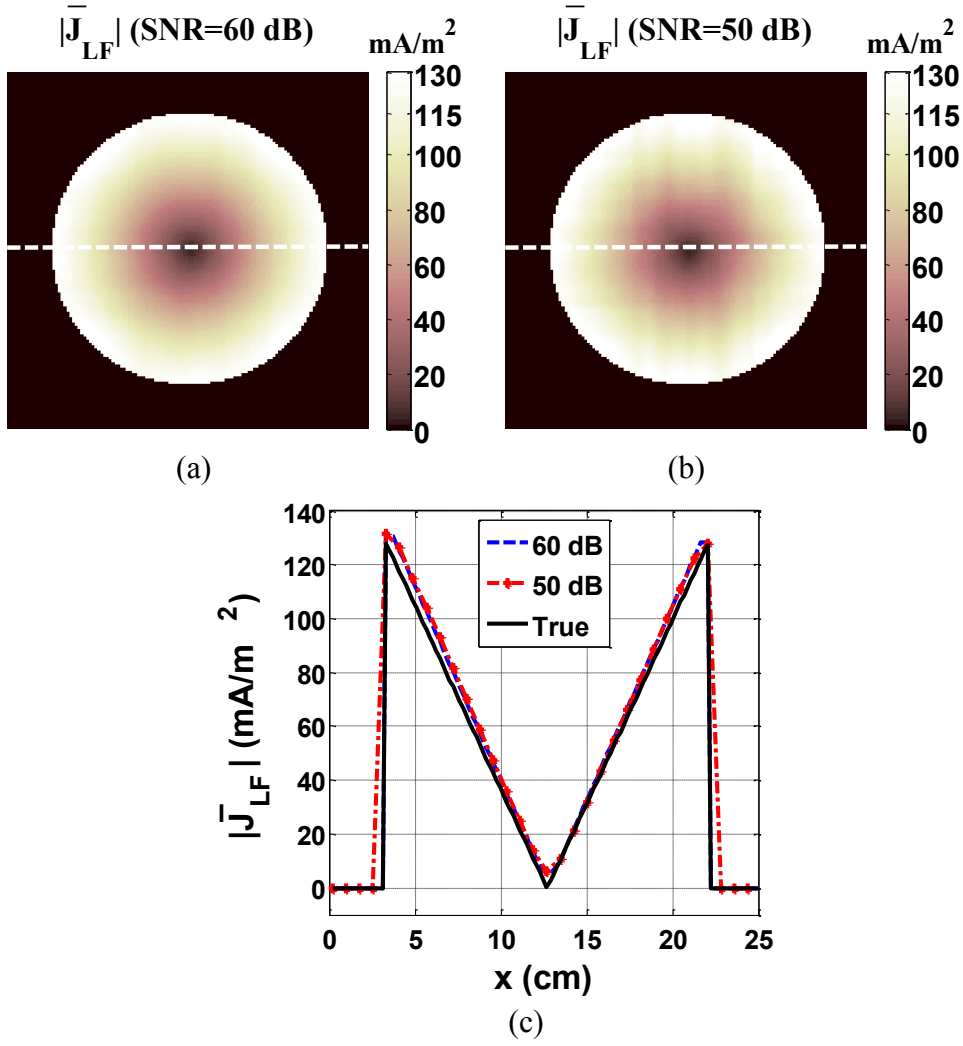
Figure 4.3 Reconstructed $\left|\bar{J}_{LF}\right|$ images (a-b) and profiles (c) of model 1.

Table 4.1 $\Delta\Phi_{LF}$, $\left|\bar{J}_{LF}\right|_{max}$, $\left|\bar{J}_{LF}\right|_{avg}$, ϵ_J, and ϵ_σ values of model 1.

$\Delta\Phi_{LF}$ (mrad)	$\left|\bar{J}_{LF}\right|_{max}$	$\left|\bar{J}_{LF}\right|_{avg}$	ϵ_J (%)		$\epsilon_{\sigma-1}$ (%)		$\epsilon_{\sigma-2}$ (%)	
			SNR (dB)					
	(mA/m^2)		50	60	50	60	50	60
12	130.4	39.3	17.3	16.9	13.2	11.5	30.3	21.0

*$\epsilon_{\sigma-1}$ and $\epsilon_{\sigma-2}$ refer to the ϵ_σ values of J-derivative and E-calculation image reconstruction algorithms.

54
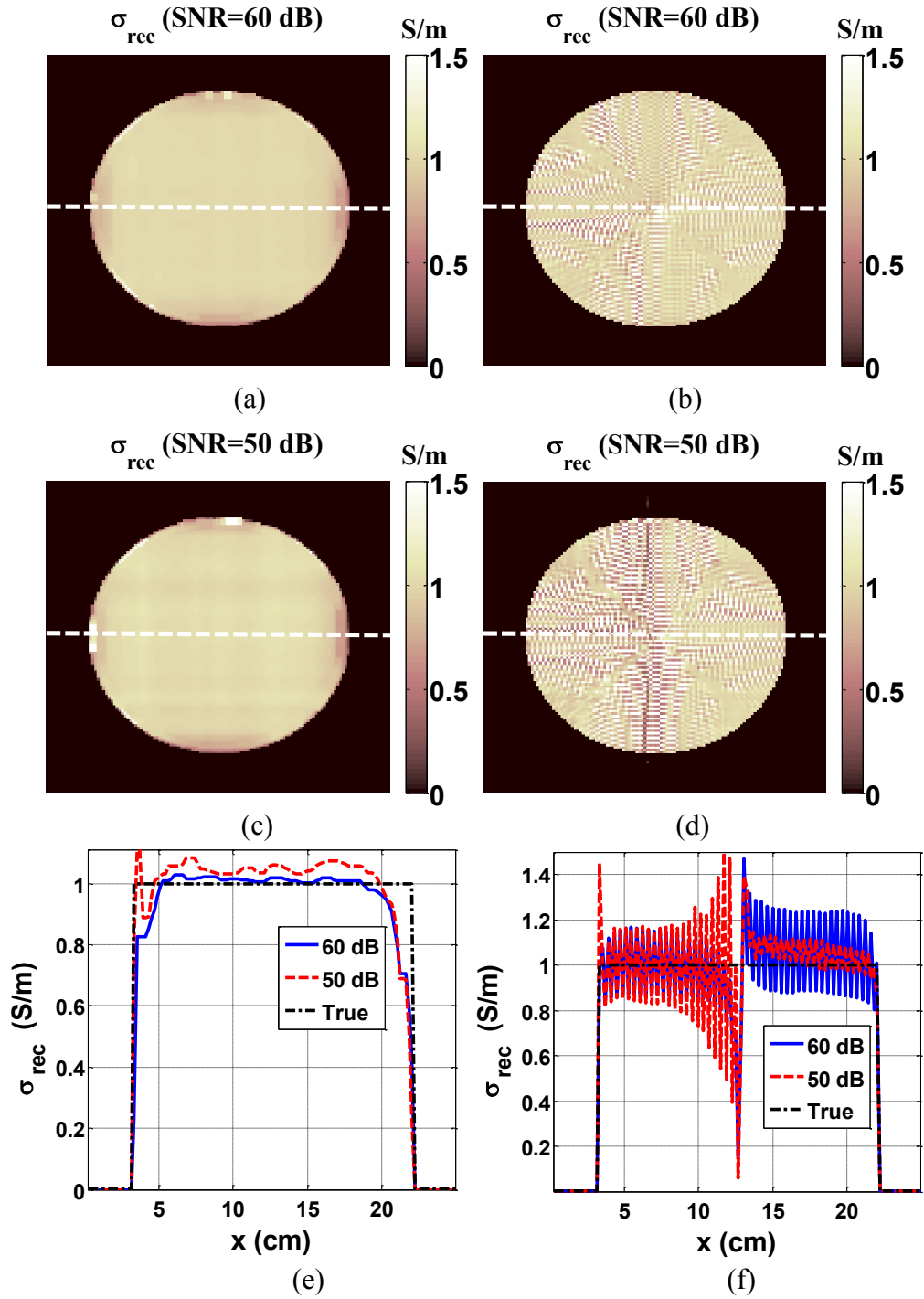
Figure 4.4 σ_{rec} images of model 1 reconstructed with J-derivative (a, c, e) and

E-calculation (b, d, f) algorithms.

4.1.2 Simulation 2

In this simulation, model 4, which includes the y-gradient coil with Phantom 1, is used. By utilizing this model, it is aimed to exhibit the imaging characteristics of ICMREIT for the y-gradient coil around a uniform conductor. Φ_{LF} distribution and profile passing through the center of the selected slice are shown in Figure 4.5.

$$\Phi_{LF} \quad \text{mrad}$$

(a)   (b)
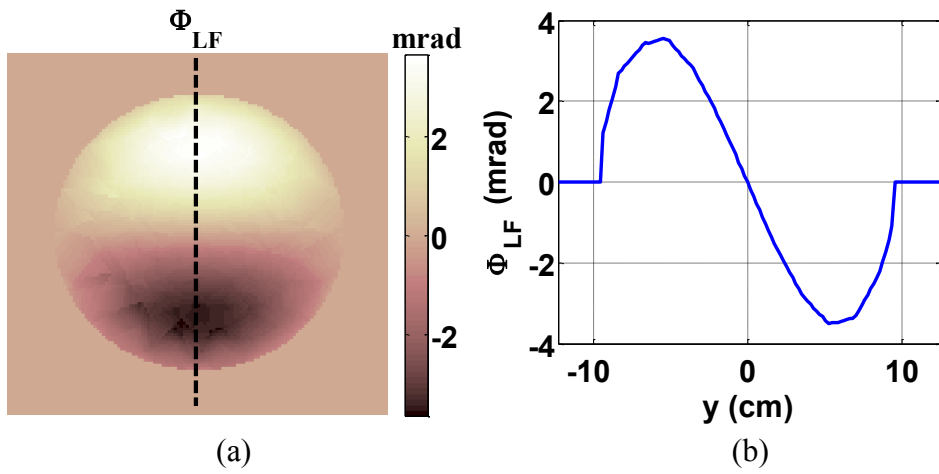
Figure 4.5 Φ_{LF} distribution (a) and profile (b) of model 4.

As shown in Figure 4.5, characteristics of the vertical Φ_{LF} profile are similar to a cubic function. Slope of the Φ_{LF} profile increases towards the boundary and the center of the selected slice. $\Delta\Phi_{LF}$ is 7.04 mrad.

Reconstructed $|\bar{J}_{LF}|$ images and profiles of model 4 are shown in Figure 4.6. As shown in Figure 4.6, reconstructed $|\bar{J}_{LF}|$ distributions do not represent the exact characteristics of the true $|\bar{J}_{LF}|$ distributions. The effect of noise is visible for the $|\bar{J}_{LF}|$ distribution reconstructed at SNR= 50 dB. Reconstruction error increases towards the boundaries.

56
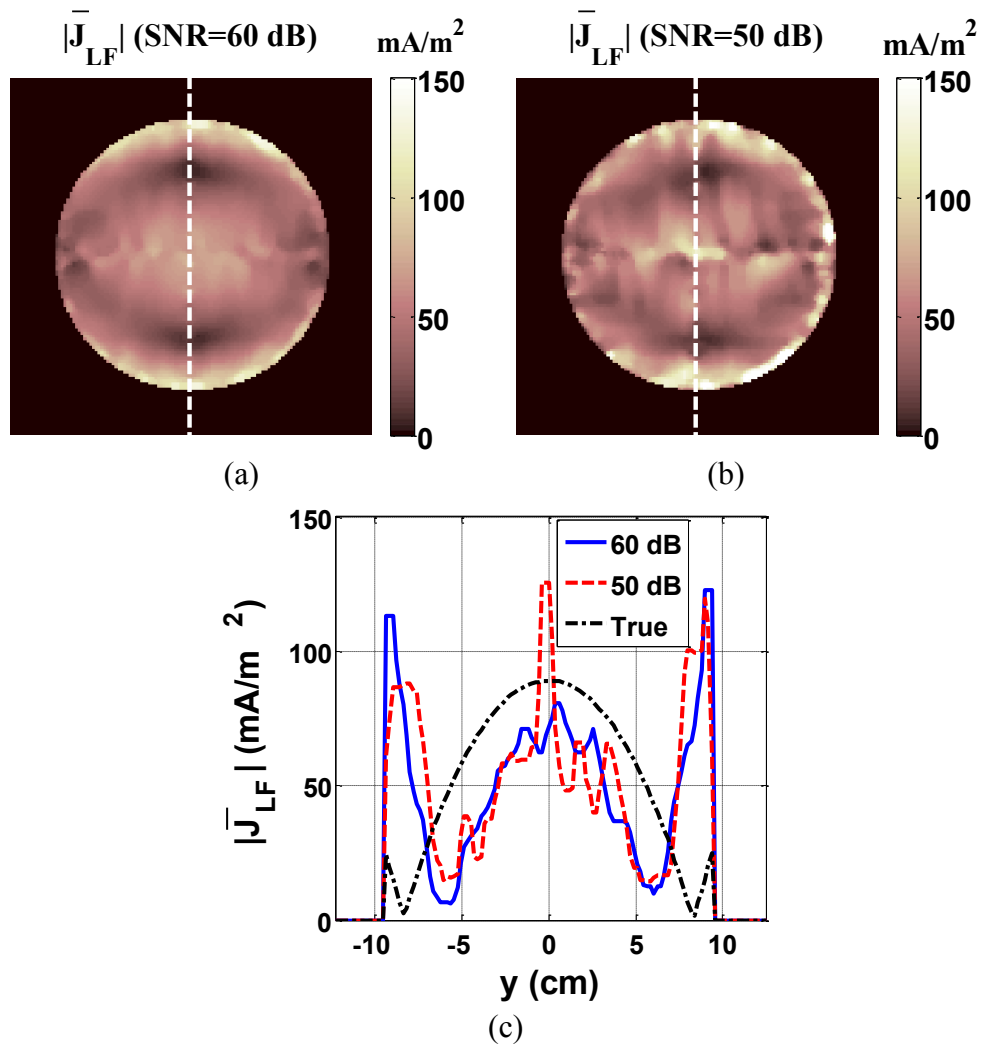
Figure 4.6 Reconstructed $\left|\bar{J}_{LF}\right|$ images (a-b) and profiles (c) of model 4.

σ_{rec} images reconstructed with J-derivative algorithm are shown in Figure 4.7. As shown in Figure 4.7, σ_{rec} values oscillate around the true σ values. Very high σ_{rec} values are observed at y=0 line. Magnitude of oscillations increases towards the boundary and the center of the selected slice.
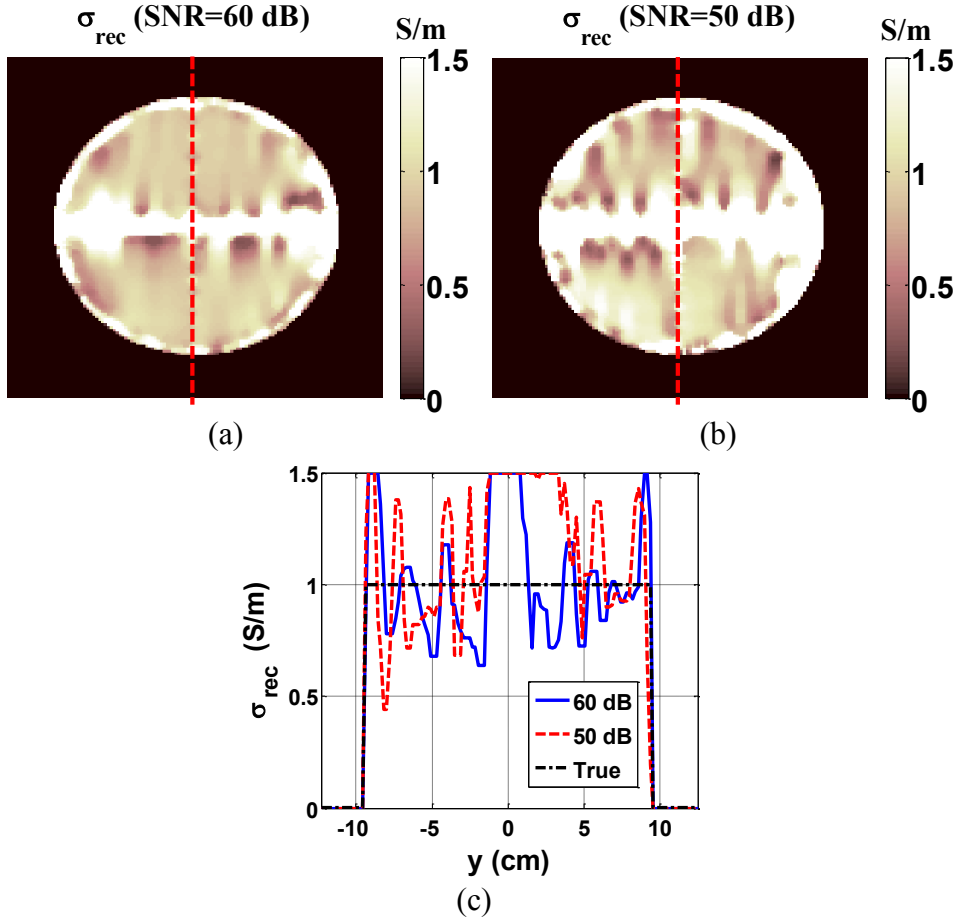
Figure 4.7 σ_{rec} images of model 4 reconstructed with J-derivative algorithm.

$\Delta\Phi_{LF}$, $\left|\bar{J}_{LF}\right|_{max}$, $\left|\bar{J}_{LF}\right|_{avg}$, ϵ_J, and ϵ_σ values of model 4 are listed in Table 4.2.

Table 4.2 $\Delta\Phi_{LF}$, $\left|\bar{J}_{LF}\right|_{max}$, $\left|\bar{J}_{LF}\right|_{avg}$, ϵ_J, and ϵ_σ values of model 4.

$\Delta\Phi_{LF}$ (mrad)	$\left|\bar{J}_{LF}\right|_{max}$	$\left|\bar{J}_{LF}\right|_{avg}$	ϵ_J (%)		ϵ_σ (%)	
			SNR (dB)			
	(mA/m^2)		50	60	50	60
7.04	89.3	20.3	410.9	379.2	36.7	30.4

58

4.1.3 Simulation 3

In this simulation, model 2a-d, which include the z-gradient coil with Phantom 2a-d, are used. By utilizing these models, it is aimed to exhibit the imaging characteristics of ICMREIT for the z-gradient coil around inhomogeneous phantoms. Φ_{LF} distributions and profiles passing through the center of the inhomogeneities are shown in Figure 4.8.

As shown in Figure 4.8, Φ_{LF} profiles have second order characteristics in the background and the inhomogeneities of the phantom, similar to the characteristics obtained for the uniform phantom. $\Delta\Phi_{LF}$ values are close to 9 mrad, which is 75 % of the $\Delta\Phi_{LF}$ value obtained for the uniform phantom. As shown in Figure 4.8 (b, d, f, h), inhomogeneities are visible in the horizontal Φ_{LF} profiles. Slope of Φ_{LF} profiles decreases inside the resistive inhomogeneities and increases inside the conductive inhomogeneities as shown in Figure 4.8 (b, d) and Figure 4.8 (f, h), respectively.

Reconstructed $|\bar{J}_{LF}|$ images and profiles of model 2a-d are shown in Figure 4.9-4.10. As shown in Figure 4.9, the inhomogeneities are visible in reconstructed $|\bar{J}_{LF}|$ distributions. As shown in Figure 4.10, reconstructed $|\bar{J}_{LF}|$ values are close to the true $|\bar{J}_{LF}|$ values. Sharp changes are observed at the boundary of the inhomogeneities. Reconstruction error increases inside the eccentric inhomogeneities and the small regions located between the boundary of the eccentric inhomogeneities and the selected slice. Slope of $|\bar{J}_{LF}|$ profiles decreases inside the resistive inhomogeneities and increases inside the conductive inhomogeneities as shown in Figure 4.10 (a-b) and Figure 4.10 (c-d), respectively.

59
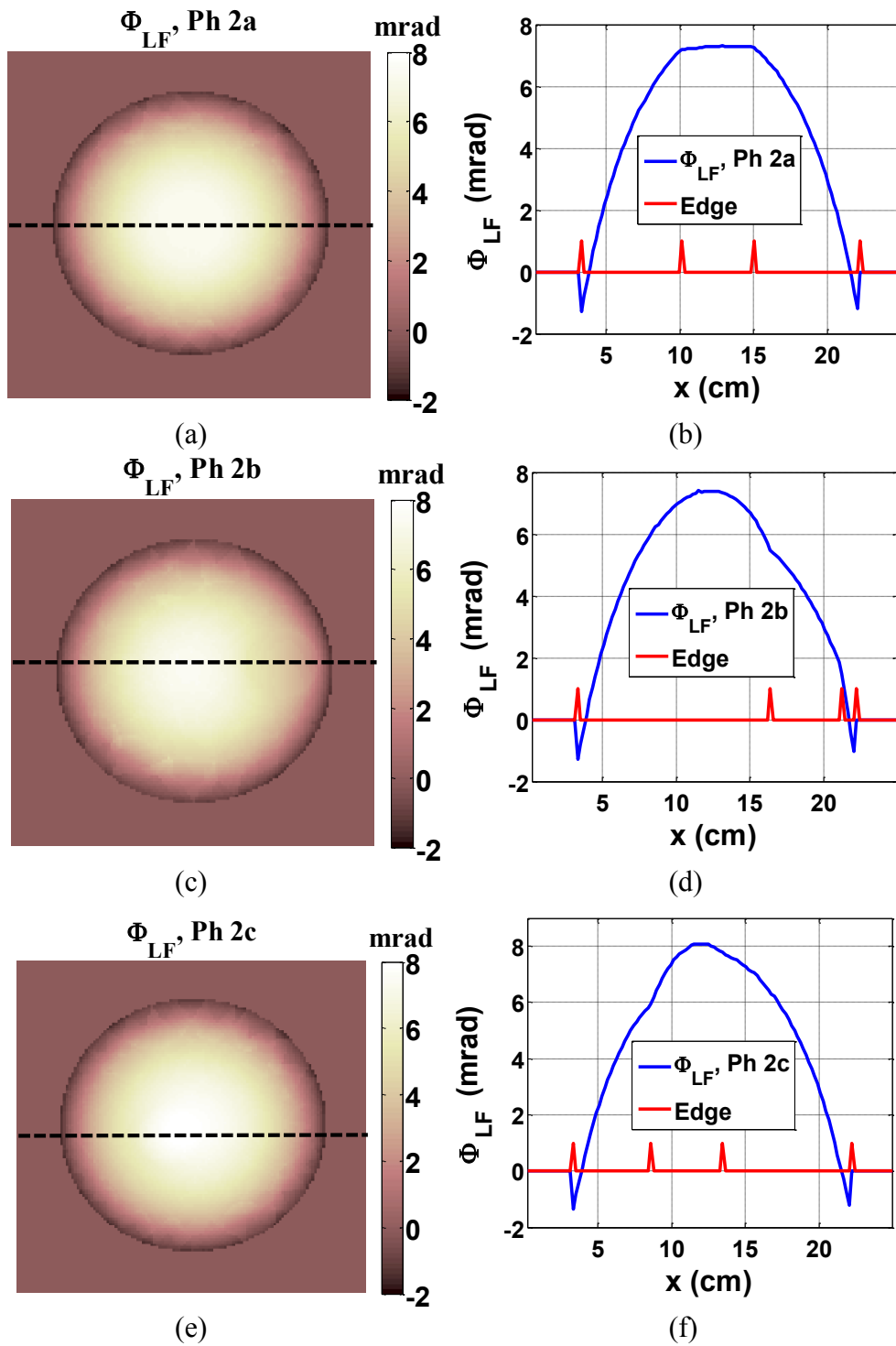
Figure 4.8 Φ_{LF} distributions and profiles of models 2a (a-b), 2b (c-d), and 2c (e-f).

Φ_{LF}, Ph 2d

(g)　　　　　　　　　　　　　　　(h)

Figure 4.8 (Continued) Φ_{LF} distributions and profiles of models 2d (g-h).

$|\bar{J}_{LF}|$ (SNR=60 dB)　　　　　$|\bar{J}_{LF}|$ (SNR=50 dB)

(a)　　　　　　　　　　　　　　　(b)
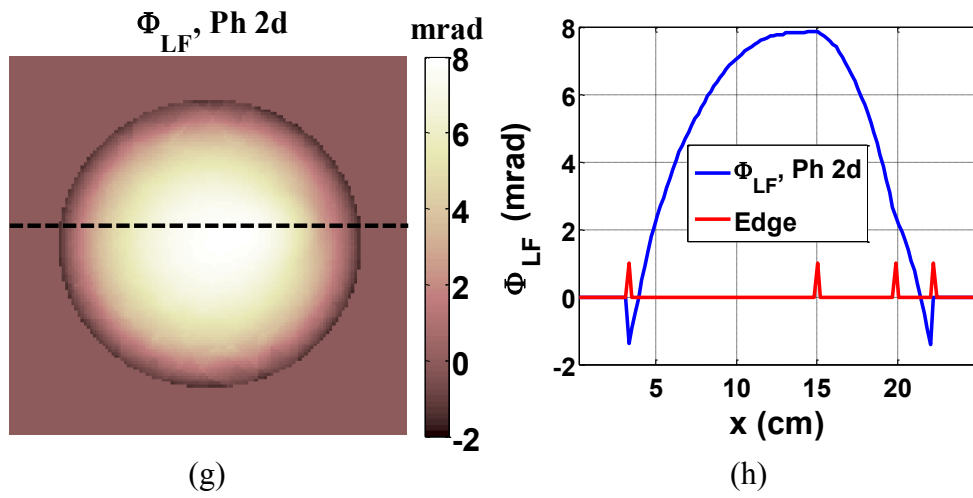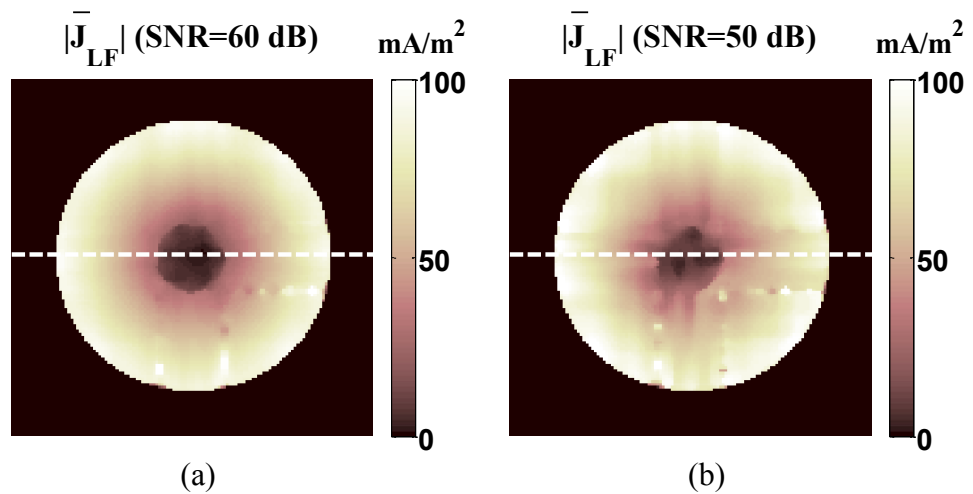
Figure 4.9 Reconstructed $|\bar{J}_{LF}|$ images for model 2a (a-b).

$|\bar{J}_{LF}|$ (SNR=60 dB)   mA/m^2

$|\bar{J}_{LF}|$ (SNR=50 dB)   mA/m^2

(c)

(d)

$|\bar{J}_{LF}|$ (SNR=60 dB)   mA/m^2

$|\bar{J}_{LF}|$ (SNR=50 dB)   mA/m^2

(e)

(f)

$|\bar{J}_{LF}|$ (SNR=60 dB)   mA/m^2

$|\bar{J}_{LF}|$ (SNR=50 dB)   mA/m^2

(g)

(h)
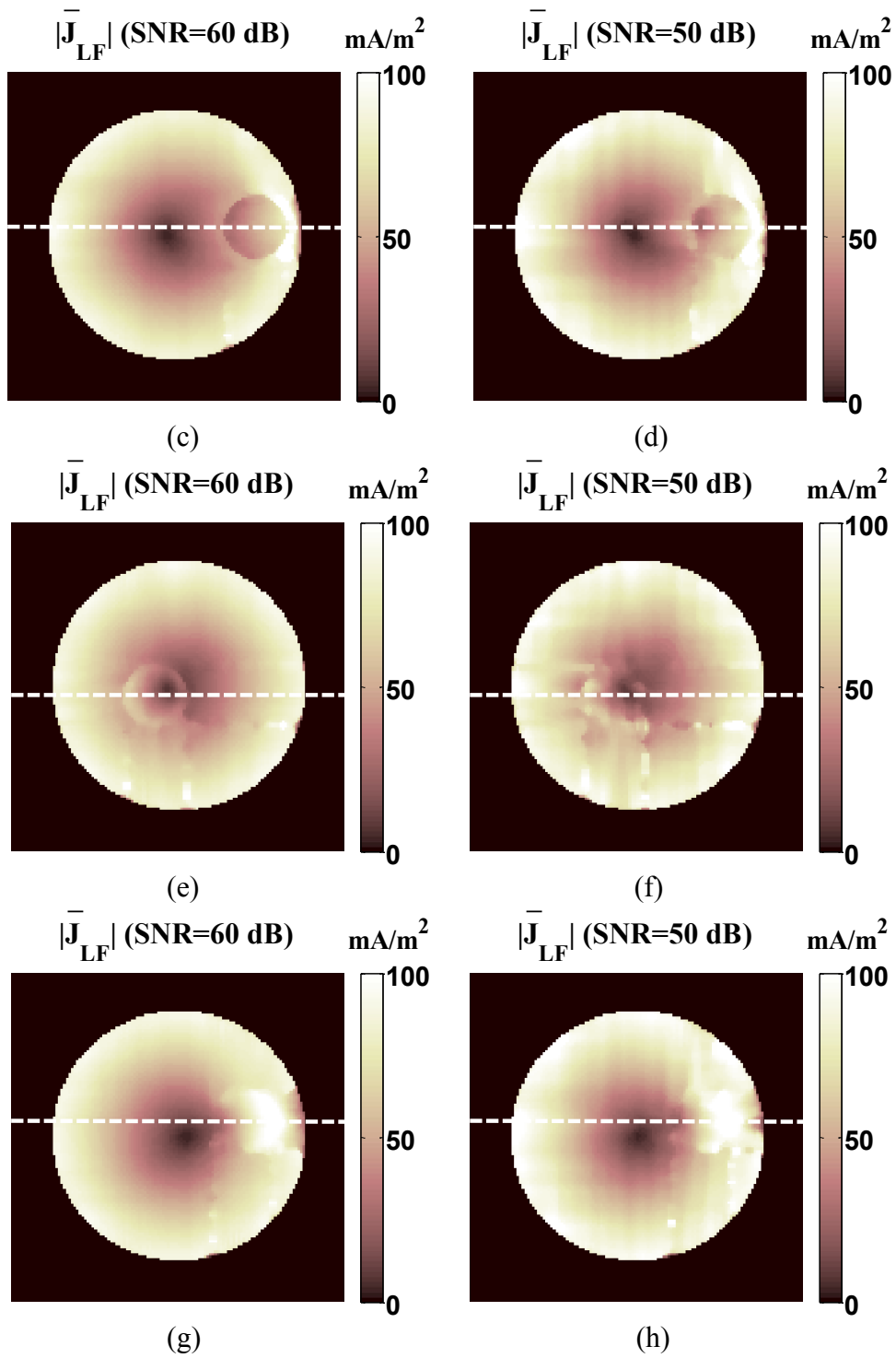
Figure 4.9 (Continued) Reconstructed $|\bar{J}_{LF}|$ images for model 2b (c-d), 2c (e-f), and 2d (g-h).
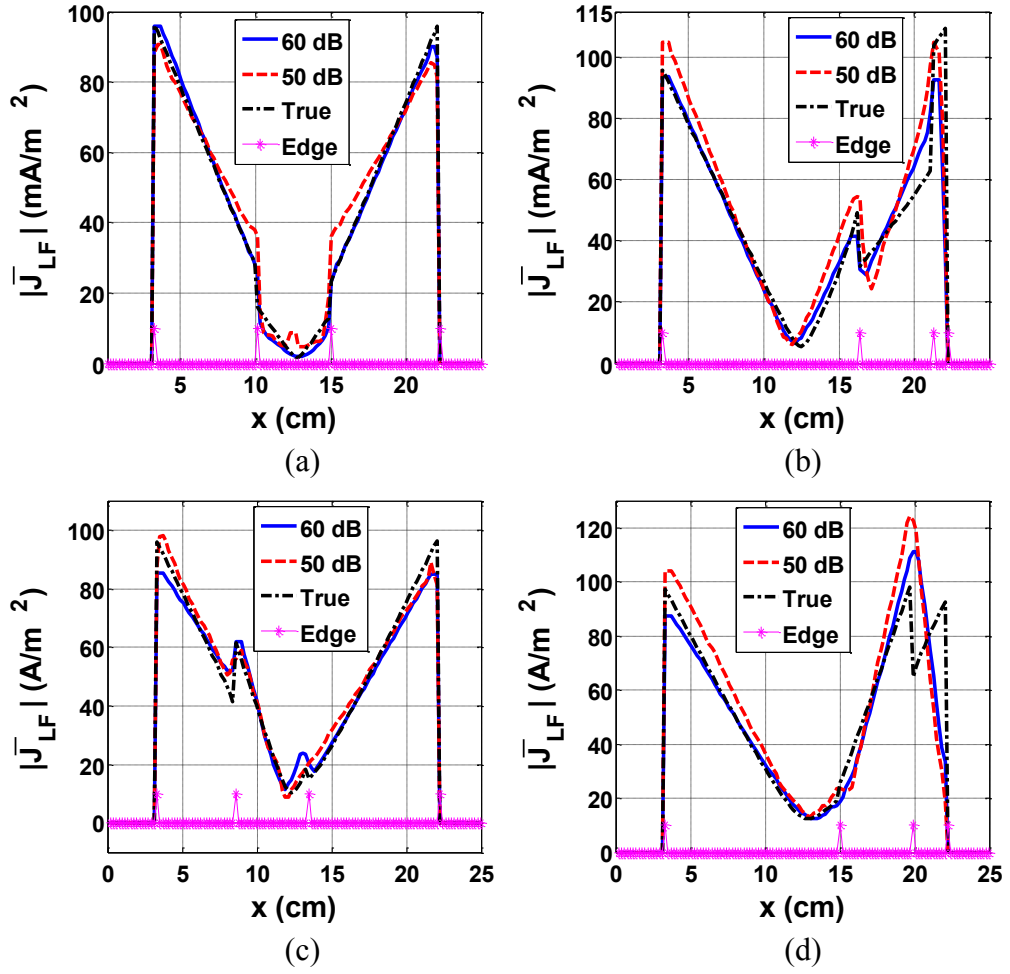
Figure 4.10 Reconstructed $\left|\bar{J}_{LF}\right|$ profiles for model 2a (a), 2b (b), 2c (c), and 2d (d).

σ_{rec} images and profiles reconstructed with J-derivative algorithm are shown in Figure 4.11-4.12. As shown in Figure 4.11, inhomogeneities are visible in σ_{rec} images. As shown in Figure 4.12, σ_{rec} values are close to the true σ values. Boundary artifacts are observed around the inhomogeneities. These artifacts are carried over the horizontal and vertical profiles passing through the boundary of the inhomogeneities.
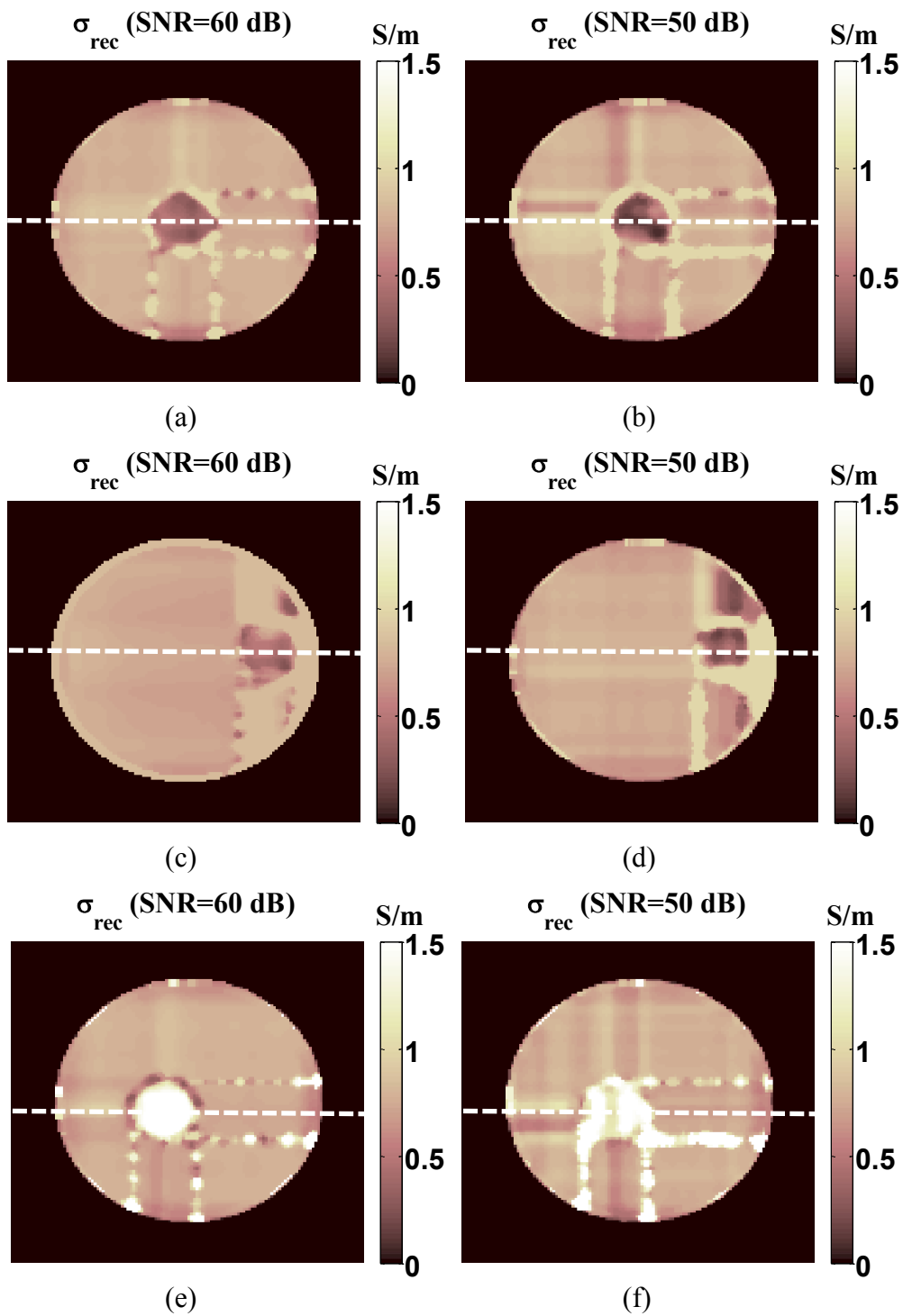
Figure 4.11 σ_{rec} images reconstructed for model 2a (a-b), 2b (c-d), and 2c (e-f).

σ_{rec} (SNR=60 dB)

σ_{rec} (SNR=50 dB)

(g)

(h)
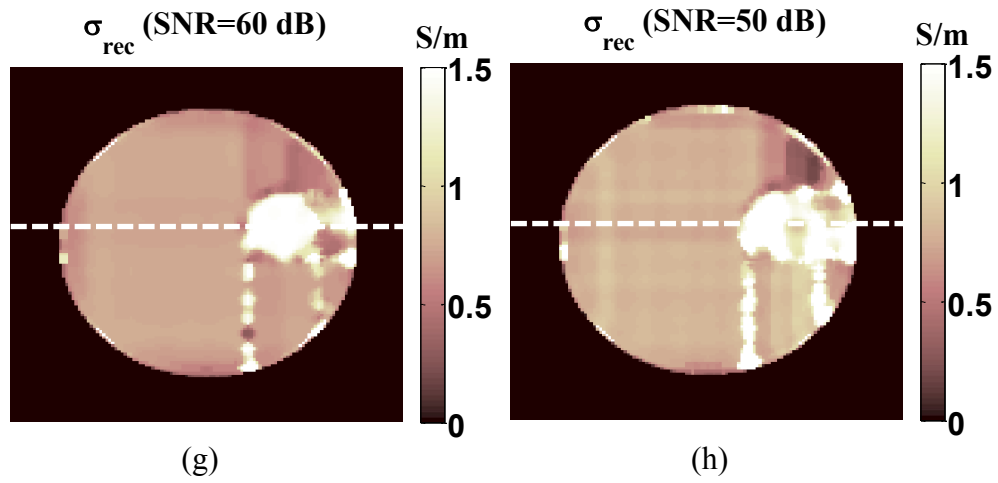
Figure 4.11 (Continued) σ_{rec} images reconstructed for model 2d (g-h).

(a)

(b)

(c)

(d)
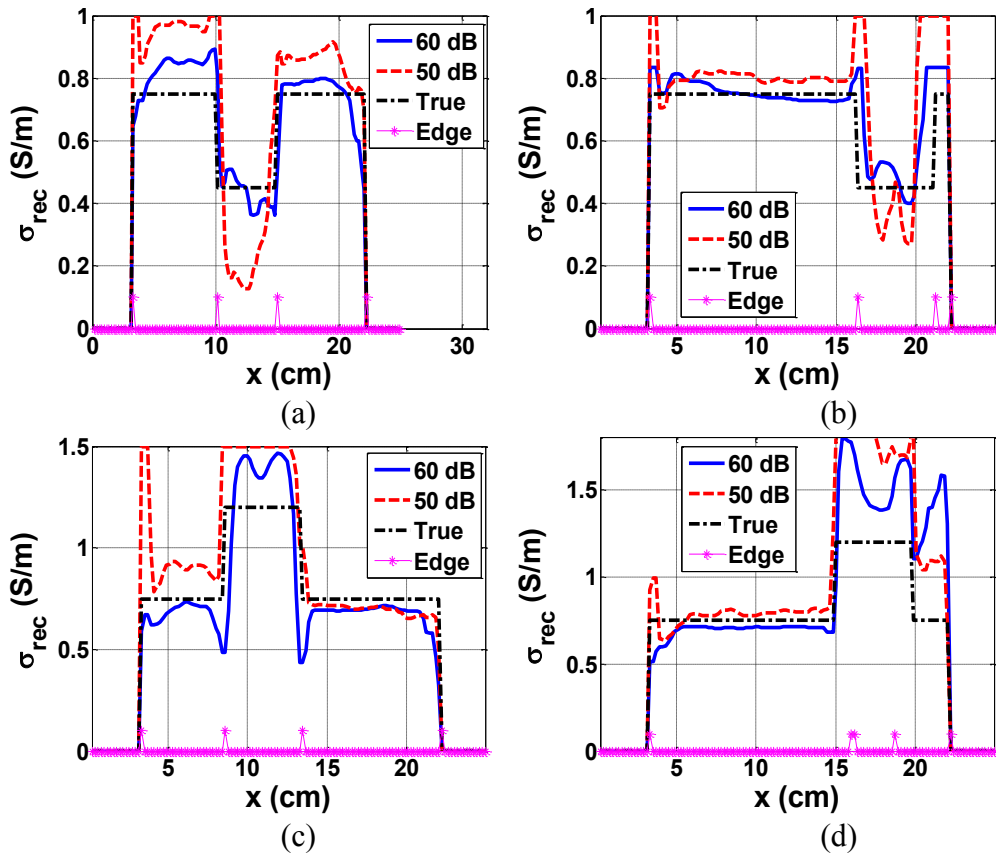
Figure 4.12 σ_{rec} profiles reconstructed for model 2a (a), 2b (b), 2c (c), and 2d (d).

$\Delta\Phi_{LF}$, $\left|\overline{J}_{LF}\right|_{max}$, $\left|\overline{J}_{LF}\right|_{avg}$, ϵ_J, and ϵ_σ of model 2a-d are listed in Table 4.3.

Table 4.3 $\Delta\Phi_{LF}$, $\left|\overline{J}_{LF}\right|_{max}$, $\left|\overline{J}_{LF}\right|_{avg}$, ϵ_J, and ϵ_σ values of model 2a-d.

Model	$\Delta\Phi_{LF}$ (mrad)	$\left|\overline{J}_{LF}\right|_{max}$	$\left|\overline{J}_{LF}\right|_{avg}$	ϵ_J (%)		$\epsilon_{\sigma-g}$ (%)		$\epsilon_{\sigma-l}$ (%)	
				SNR (dB)					
		(mA/m^2)		50	60	50	60	50	60
2a	8.6	97.8	29.3	30.9	14.7	24.8	19.3	70.3	53.5
2b	8.7	110.2	28.6	15.0	12.0	28.1	14.9	86.5	48.0
2c	9.4	97.9	29.8	21.3	18.3	32.7	22.3	24.7	22.1
2d	9.3	100.1	30.2	20.7	12.6	23.2	17.1	33.8	27.5

*$\epsilon_{\sigma-g}$ and $\epsilon_{\sigma-l}$ refer to the global ϵ_σ values of the whole slice and the local ϵ_σ values of the inhomogeneities, respectively.

4.1.4 Simulation 4

In this simulation, model 3a-d, which include the z-gradient coil with Phantom 3a-d, are used. By utilizing these models, it is aimed to exhibit the imaging characteristics of ICMREIT for the z-gradient coil around a conductor with small conductivity inhomogeneities. Φ_{LF} distributions and profiles passing through the center of the inhomogeneities are shown in Figure 4.13. As shown in Figure 4.8 and Figure 4.13, characteristics of Φ_{LF} distributions obtained for the phantoms including a small inhomogeneity are similar to the corresponding characteristics of the phantoms including a large inhomogeneity. Inhomogeneities are visible in the Φ_{LF} profiles passing through the inhomogeneities.
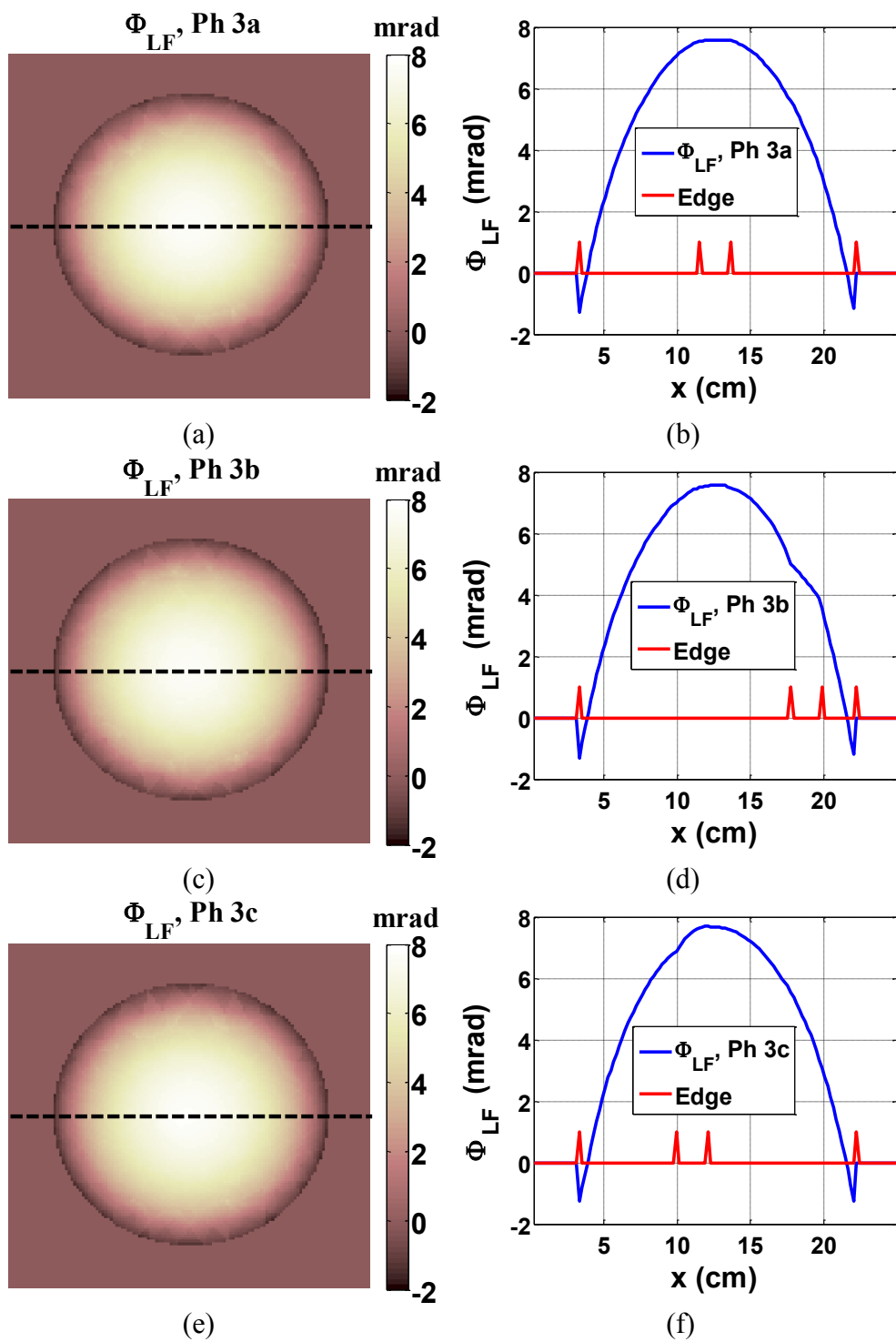
Figure 4.13 Φ_{LF} distributions and profiles of model 3a (a-b), 3b (c-d), and 3c (e-f).

Φ_{LF}, Ph 3d

(g)   (h)
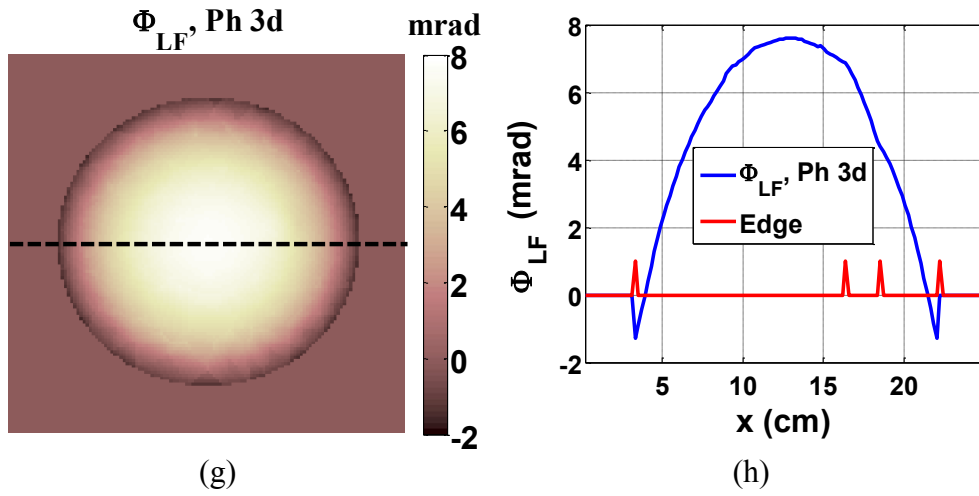
Figure 4.13 (Continued) Φ_{LF} distributions and profiles of model 3d (g-h).

Reconstructed $|\bar{J}_{LF}|$ images and profiles of model 3a-d are shown in Figure 4.14-4.15. As shown in Figure 4.14, visibility of eccentric inhomogeneities is greater than visibility of concentric inhomogeneities. As shown in Figure 4.15, background of the reconstructed and the true $|\bar{J}_{LF}|$ distributions are close to each other. However, reconstruction error increases inside the eccentric inhomogeneities and the regions between the eccentric inhomogeneities and the boundary of the phantom. Slope of $|\bar{J}_{LF}|$ profiles decreases inside the resistive inhomogeneities and increases inside the conductive inhomogeneities as shown in Figure 4.15 (a-b) and Figure 4.15 (c-d), respectively.

σ_{rec} images and profiles reconstructed with J-derivative algorithm are shown in Figure 4.16-4.17.

68
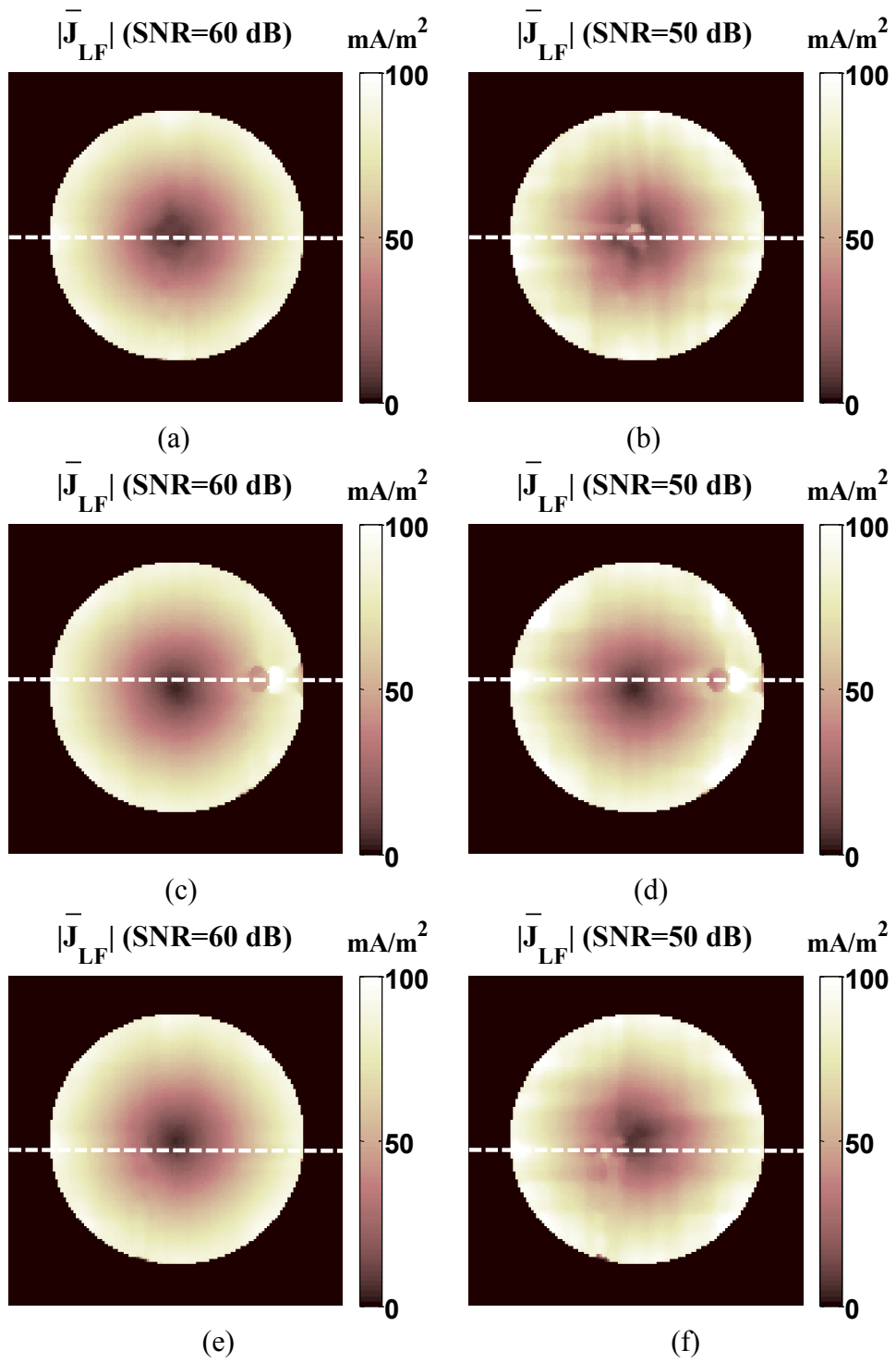
Figure 4.14 Reconstructed $|\bar{J}_{LF}|$ images for model 3a (a-b), 3b (c-d), and 3c (e-f).

$|\bar{J}_{LF}|$ (SNR=60 dB)   mA/m^2 $|\bar{J}_{LF}|$ (SNR=50 dB)   mA/m^2

(e)   (f)
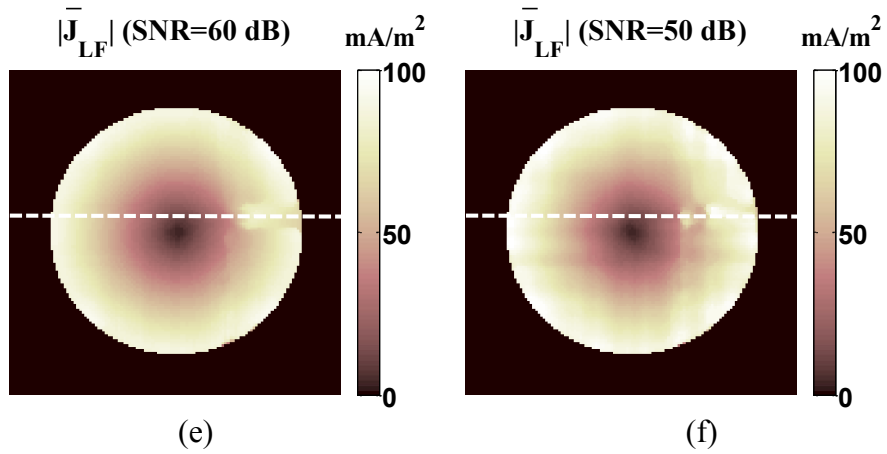
Figure 4.14 (Continued) Reconstructed $|\bar{J}_{LF}|$ images for model 3d (g-h).

(a)

(b)

(c)

(d)
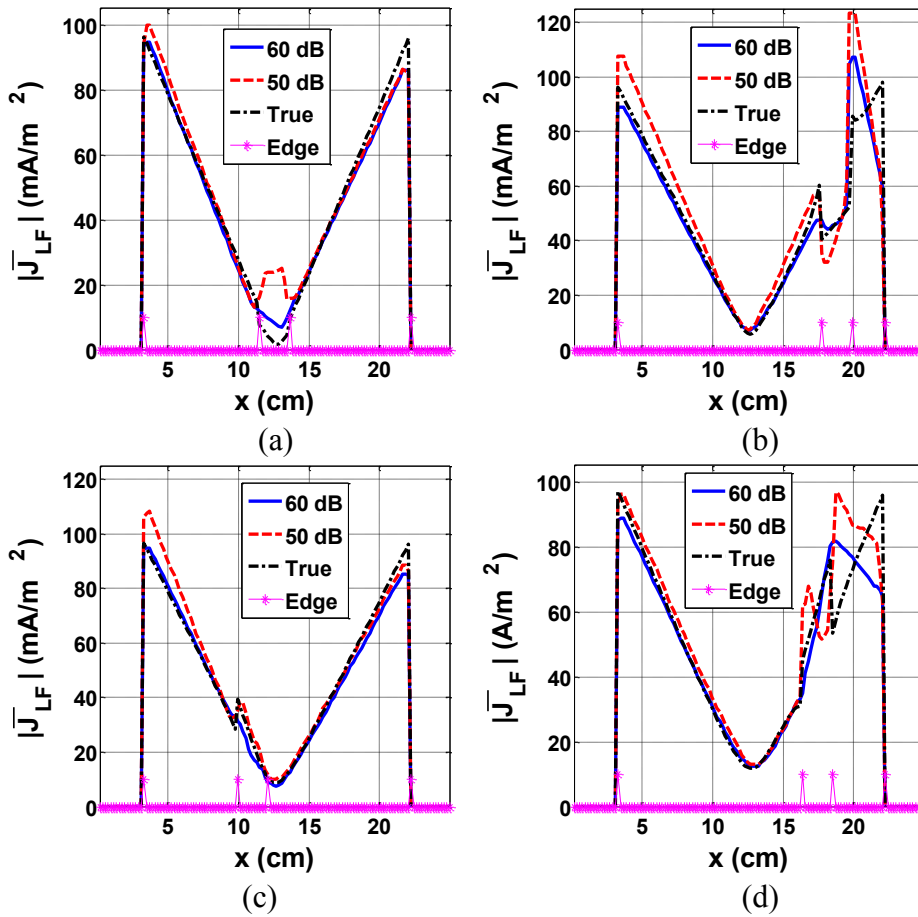
Figure 4.15 Reconstructed $|\bar{J}_{LF}|$ profiles for model 3a (a), 3b (b), 3c (c), and
3d (d).

70
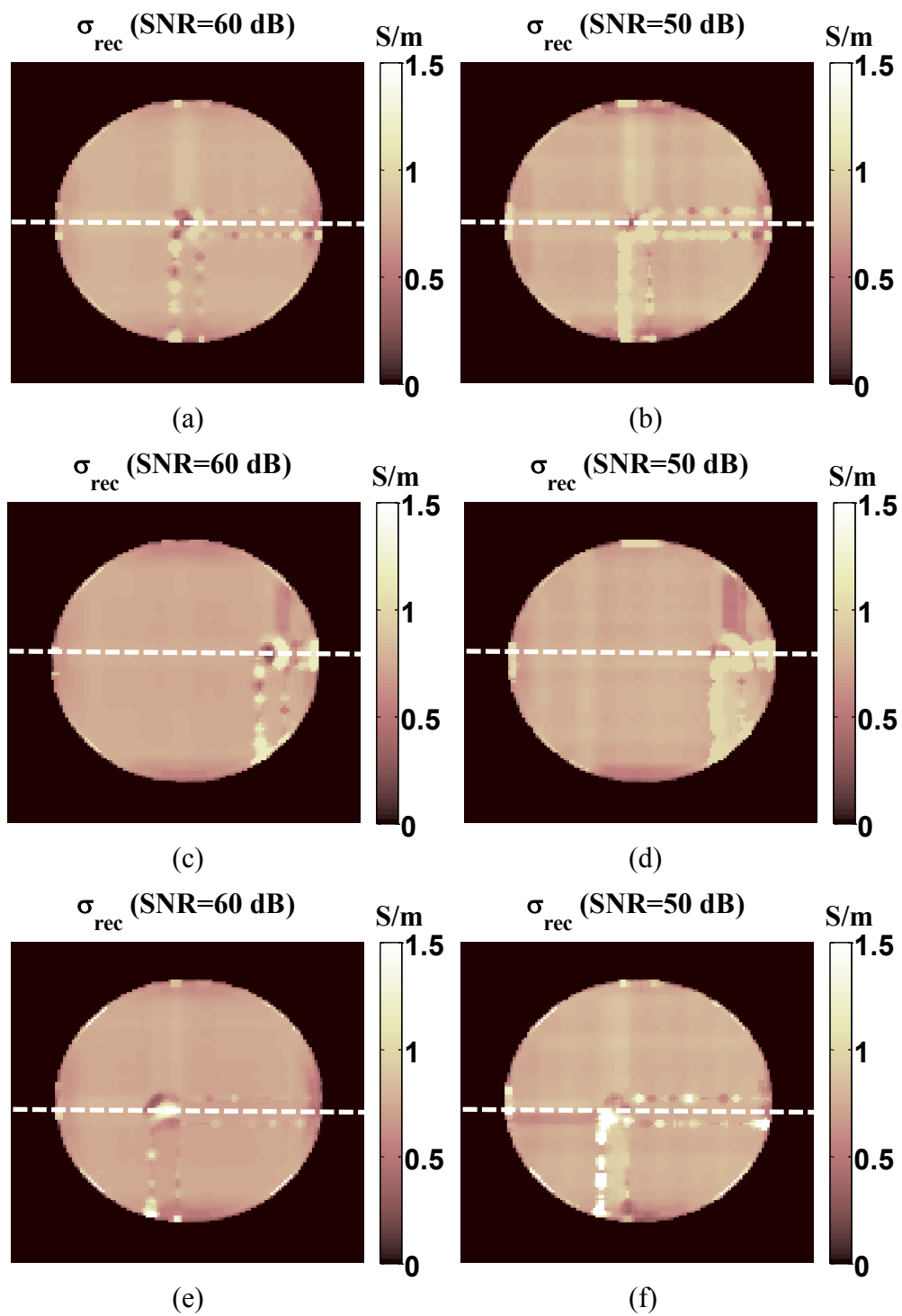
Figure 4.16 σ_{rec} images reconstructed for model 3a (a-b), 3b (c-d), and 3c (e-f).

(g)   (h)
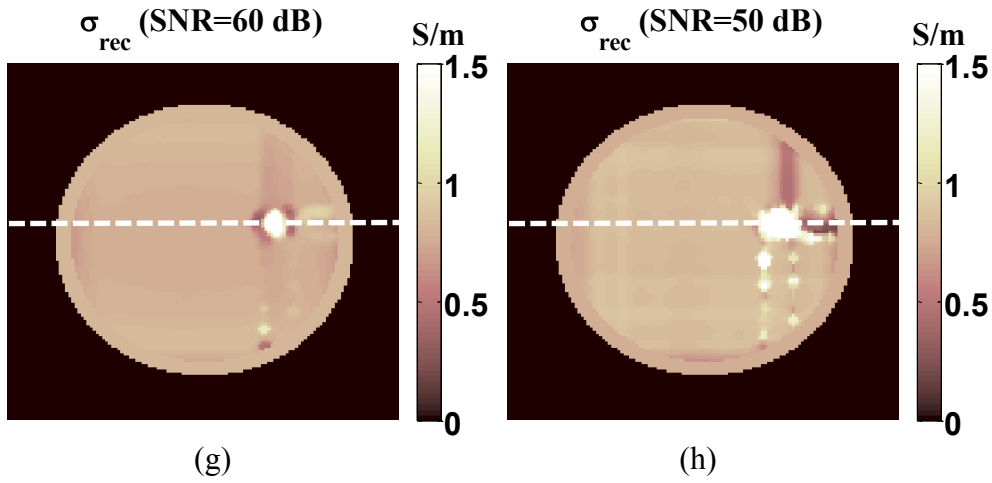
Figure 4.16 (Continued) σ_{rec} images reconstructed for model 3d (g-h).

(a)   (b)

(c)   (d)
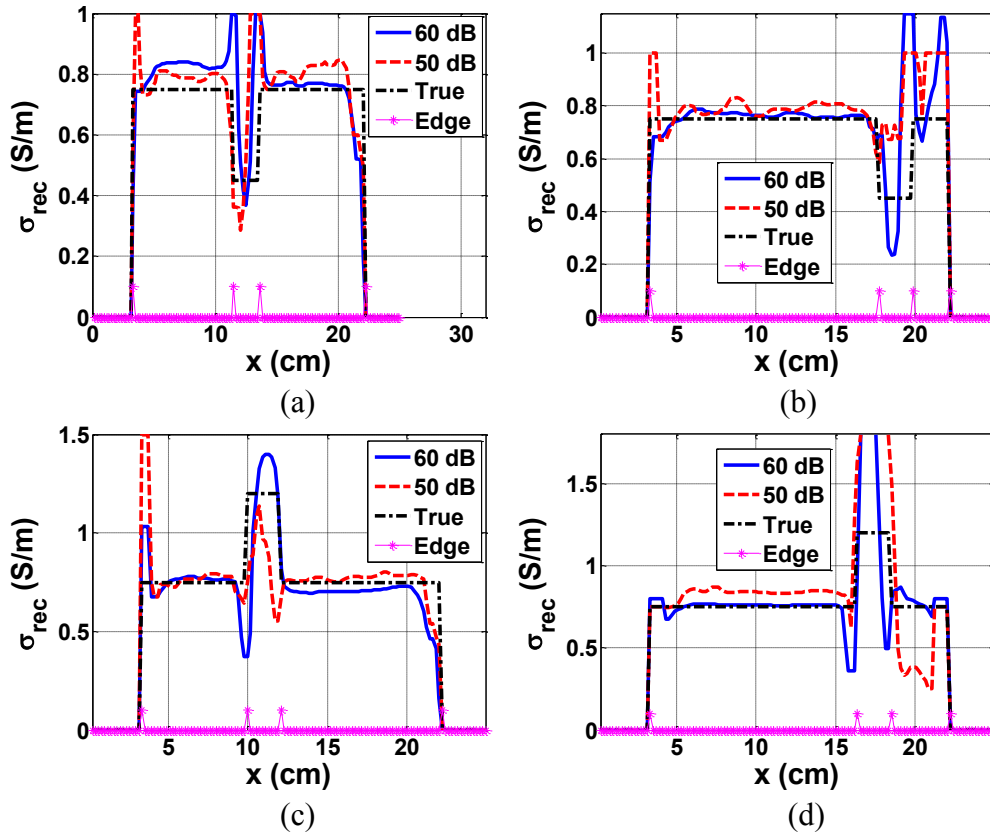
Figure 4.17 σ_{rec} profiles reconstructed for model 3a (a), 3b (b), 3c (c), and 3d (d).

As shown in Figure 4.16, visibility of the inhomogeneities is low especially for σ_{rec} images reconstructed at SNR=50 dB. As shown in Figure 4.17, σ_{rec} profiles are close to the true σ profiles in the background of the phantom. As shown in Figure 4.17, σ_{rec} values exhibit the resistive and the conductive properties of the inhomogeneities, although deviations from the true σ values are observed. Boundary artifacts are observed around the inhomogeneities which are carried over the horizontal and the vertical profiles passing through the boundary of the inhomogeneities.

$\Delta\Phi_{LF}$, $\left|\bar{J}_{LF}\right|_{max}$, $\left|\bar{J}_{LF}\right|_{avg}$, ϵ_J, and ϵ_σ values of model 3a-d are summarized in Table 4.4.

Table 4.4 $\Delta\Phi_{LF}$, $\left|\bar{J}_{LF}\right|_{max}$, $\left|\bar{J}_{LF}\right|_{avg}$, ϵ_J, and ϵ_σ values of model 3a-d.

Mod.	$\Delta\Phi_{LF}$ (mrad)	$\left|\bar{J}_{LF}\right|_{max}$	$\left|\bar{J}_{LF}\right|_{avg}$	ϵ_J (%)		$\epsilon_{\sigma-g}$ (%) SNR (dB)		$\epsilon_{\sigma-l}$ (%)	
		(mA/m^2)		50	60	50	60	50	60
3a	8.8	97.8	29.4	116.8	28.8	18.5	14.5	89.0	73.7
3b	8.9	99.3	29.3	22.1	18.5	18.2	17.5	102.4	98.2
3c	9.0	97.8	29.5	16.5	9.1	18.3	15.1	31.1	23.7
3d	8.9	97.9	29.5	10.2	8.9	12.6	7.9	24.3	19.3

4.2 Results of the Distinguishability and the Sensitivity Analyses

As mentioned in Chapter 3, sensitivity analysis is performed by locating a small cylindrical inhomogeneity at different locations on x axis and adjusting the conductivity of the inhomogeneity. $|\Delta B_z(x,y)|_{avg}$ as a function of C_{ih} and $\Delta\sigma$ is shown in Figure 4.18.
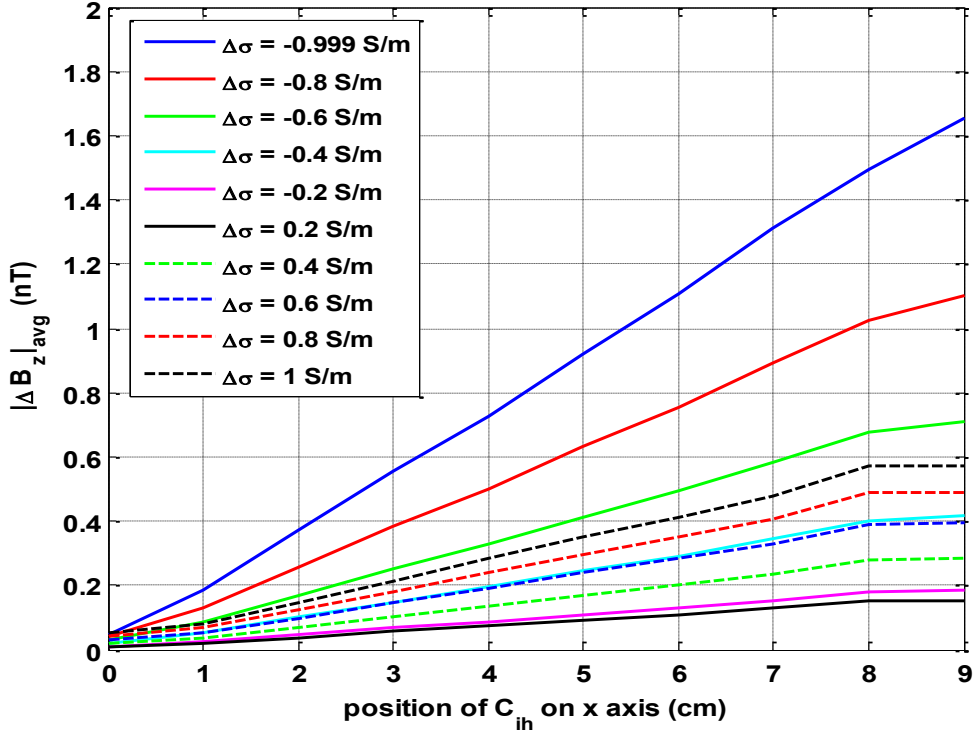
Figure 4.18 $|\Delta B_z(x,y)|_{avg}$ as a function of $\Delta\sigma$ and location of C_{ih}.

As shown in Figure 4.18, $|\Delta B_z(x,y)|_{avg}$ increases as a function of the distance between the center of the conductor and C_{ih}. $|\Delta B_z(x,y)|_{avg}$ changes between $0.03 \leq |\Delta B_z(x,y)|_{avg} \leq 0.71$ nT and $0.03 \leq |\Delta B_z(x,y)|_{avg} \leq 0.39$ nT for $\Delta\sigma$ =-0.6 S/m and $\Delta\sigma$ =0.6 S/m, respectively. It is observed that sensitivity of ICMREIT to central conductivity perturbations are smaller than sensitivity of ICMREIT to eccentric conductivity perturbations. The maximum and the minimum $|\Delta B_z(x,y)|_{avg}$ values are obtained for $C_{ih} = 9$ cm and $C_{ih} = 0$ cm, respectively. The ratio between the minimum and the maximum $|\Delta B_z(x,y)|_{avg}$ values ($R_{min/max}$) are below 10 % for all $\Delta\sigma$ levels. $R_{min/max}$ values are obtained as 2.99 %, 3.91 %, 7.87 %, and 8.90 % for $\Delta\sigma$ =-1, -0.6, 0.6, and 1 S/m, respectively.

As shown in Figure 4.18, sensitivity of ICMREIT to resistive ($\Delta\sigma < 0$) perturbations is greater than the sensitivity of ICMREIT to conductive ($\Delta\sigma > 0$) perturbations. $|\Delta B_z(x,y)|_{avg}$ changes between $0.04 \leq |\Delta B_z(x,y)|_{avg} \leq 1$ nT and $0.03 \leq |\Delta B_z(x,y)|_{avg} \leq 0.49$ nT for $\Delta\sigma = -0.8$ S/m and $\Delta\sigma = 0.8$ S/m, respectively.

After the sensitivity analysis, distinguishability analysis is performed. Distinguishability of ICMREIT measurements as a function of $\Delta\sigma$ ve ρ_{ih} are shown in Figure 4.19-4.20. As shown in Figure 4.19 (a), D values obtained for the resistive and the conductive inhomogeneities are at the same level. D values change as a function of $\Delta\sigma$ and ρ_{ih}. For $|\Delta\sigma| \geq 0.4$ S/m and $\rho_{ih} \geq 5$ cm, D is greater than 60 %. For $|\Delta\sigma| \geq 0.6$ S/m and $\rho_{ih} \geq 6$ cm, D is greater than 80 %. For $|\Delta\sigma| \leq 0.2$ S/m and $\rho_{ih} \leq 4$ cm, D is smaller than 20 %. As shown in Figure 4.19 (b), variation of D is symmetric around $\Delta\sigma = 0$ S/m. It is observed that the concentric inhomogeneity is invisible between $-0.5 \leq \Delta\sigma \leq 0.5$ S/m and $-0.2 \leq \Delta\sigma \leq 0.2$ S/m for $\rho_{ih} = 2$ cm and $\rho_{ih} = 3$ cm, respectively. The variation of D in Figure 4.19 shows that distinguishability of a concentric inhomogeneity increases as $\Delta\sigma$ and ρ_{ih} increase.

As shown in Figure 4.20 (a), D values obtained for the resistive eccentric inhomogeneities are greater than the D values obtained for the conductive eccentric inhomogeneities. D values are between $7.64 \leq D \leq 87.95$ % and $32.48 \leq D \leq 90.33$ % for $\Delta\sigma = 0.4$ S/m and $\Delta\sigma = -0.4$ S/m, respectively. It is also observed that D values obtained for the eccentric inhomogeneities are greater than the D values obtained for the concentric inhomogeneities. As shown in Figure 4.20 (b), the eccentric inhomogeneity is invisible between $-0.2 \leq \Delta\sigma \leq 0.3$ S/m and $-0.1 \leq \Delta\sigma \leq 0.1$ S/m for $\rho_{ih} = 1$ cm and $\rho_{ih} = 2$ cm, respectively.
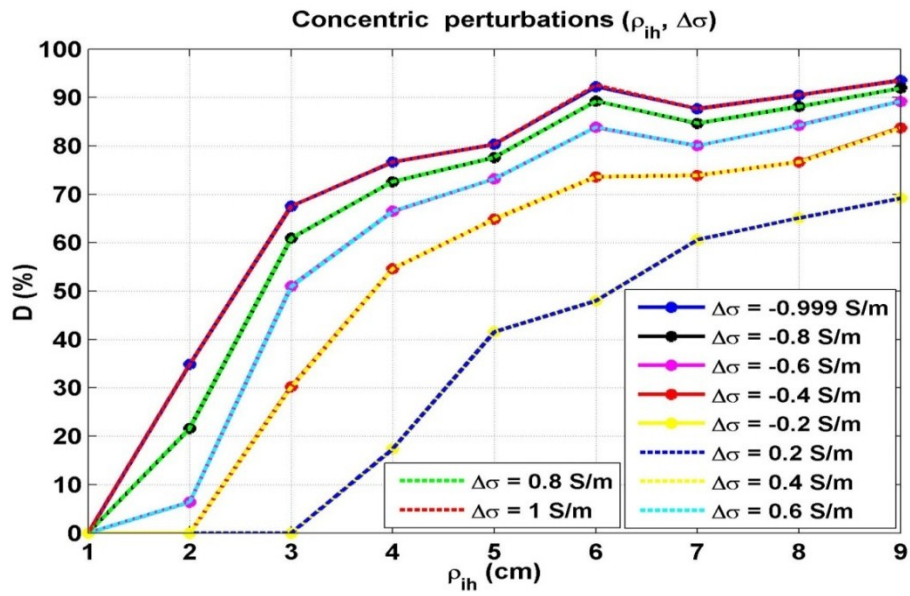
(a)
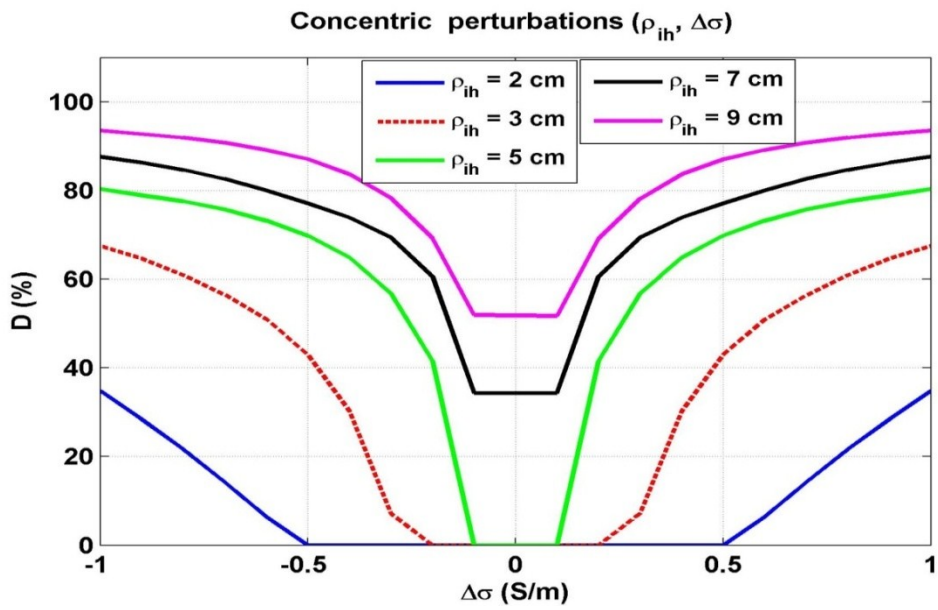
(b)

Figure 4.19 Variation of D as a function of ρ_{ih} and $\Delta\sigma$ for a conductor including a concentric inhomogeneity (σ_2).
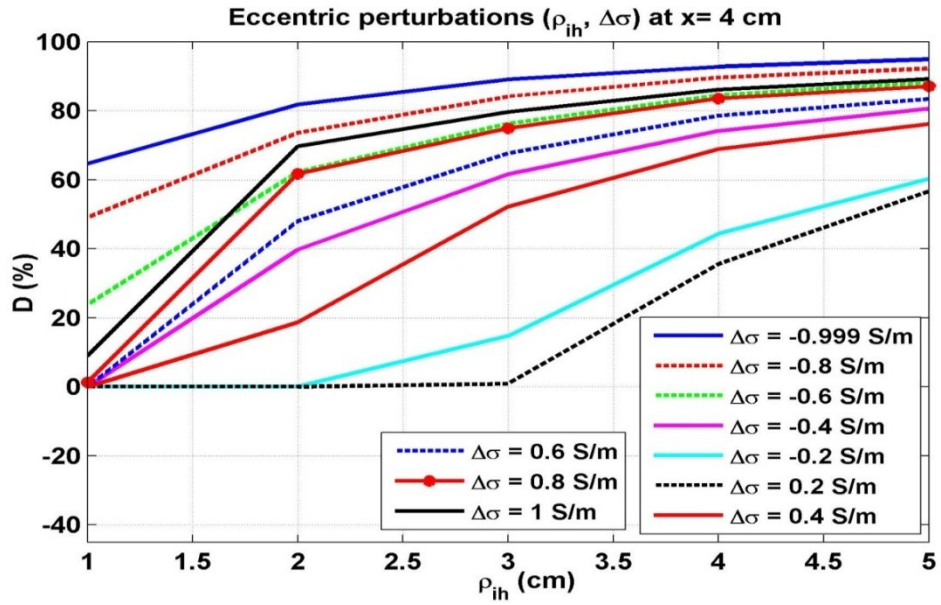
(a)
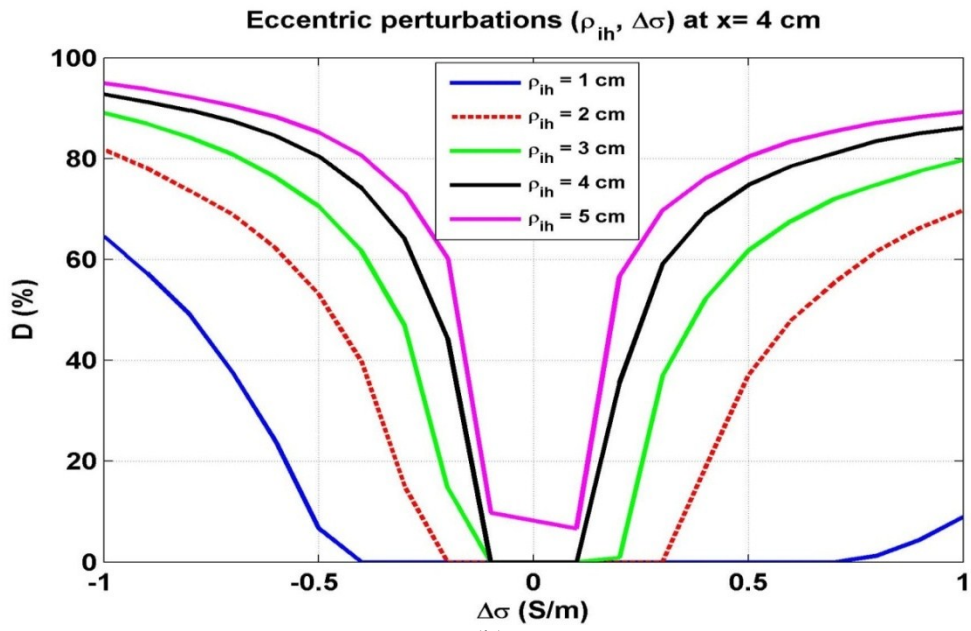
(b)

Figure 4.20 Variation of D as a function of ρ and $\Delta\sigma$ for a conductor including

an eccentric inhomogeneity (σ_3).

As shown in Figure 4.20 (b), D values increase as a function of ρ_{ih}. D is

non-zero for $\rho_{ih} > 2$ cm. D is between $39.75 \leq D \leq 93.15$ % and $57.8 \leq D \leq 94.76$ % for $\rho_{ih}=4$ cm and $\rho_{ih}=5$ cm, respectively.

4.3 Experimental Results

4.3.1 Experiment 1

In this experiment, Phantoms 1a-b, which include saline solutions of 0.75 S/m and 1.48 S/m, are used. It is aimed to exhibit the experimental performance of ICMREIT for uniform phantoms. MR magnitude images and profiles passing through the center of the selected slice and the center profile of the k-space magnitude images are shown in Figure 4.21.

As shown in Figure 4.21 (a-c), MR magnitude values of Phantom 1a and Phantom 1b are close to 0.17 and 0.02 arbitrary units (a.u.), respectively. Ring patterns are observed for the MR magnitude image of Phantom 1b. As shown in Figure 4.21 (d), k-space magnitude images are concentrated in low frequency region and have maximum values of 0.048 and 0.0056 a.u. for Phantoms 1a and 1b, respectively. It is observed that MR and k-space magnitude values of Phantom 1b are a single order of magnitude smaller than the corresponding values of Phantom 1a.

Φ_{LF} distributions and profiles acquired for Phantom 1a-b are shown in Figure 4.22. As shown in Figure 4.22 (a-c), characteristics of the Φ_{LF} distribution obtained for Phantom 1a are similar to the corresponding characteristics obtained for simulation model 1, which is composed of a z-gradient coil around a uniform conductor.

78
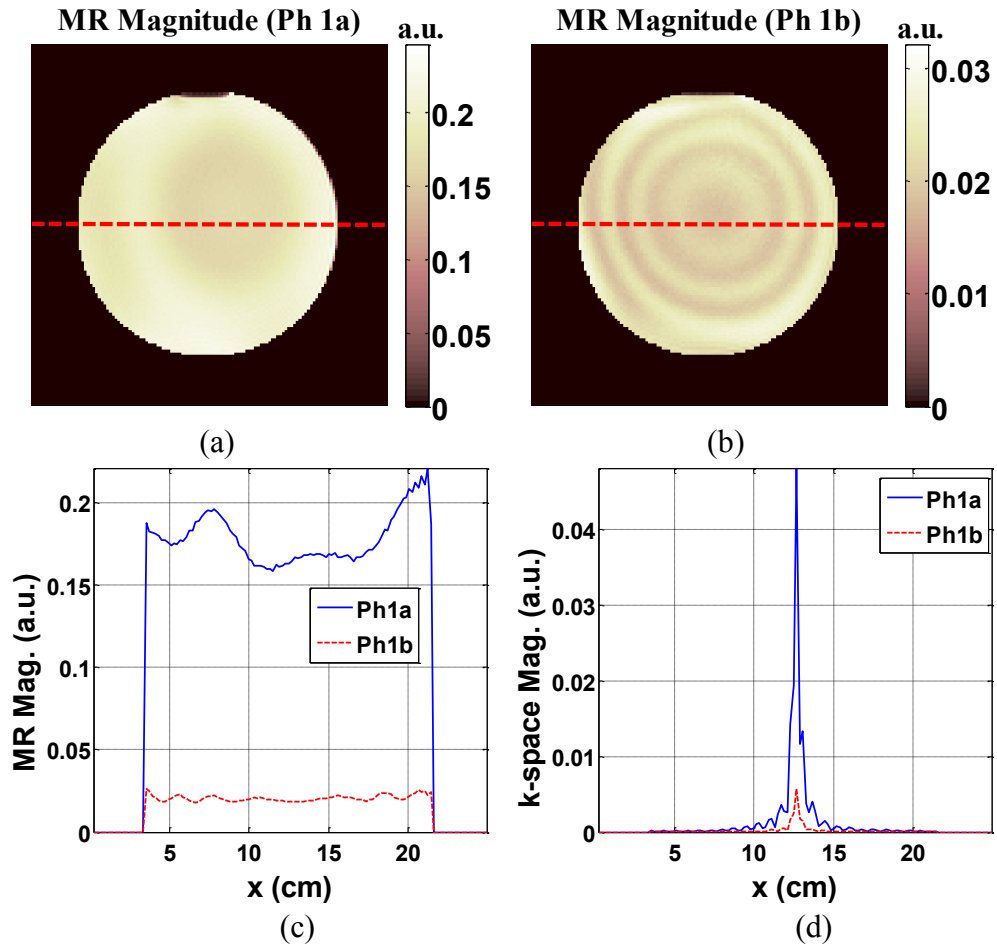
Figure 4.21 MR magnitude images (a-b) and profiles (c) passing through the center of the selected slice and the center profile of the k-space magnitude images (d).

As shown in Figure 4.22 (a, c), slope of Φ_{LF} profile increases towards the boundary of the phantom. $\Delta\Phi_{LF}$ of Phantom 1a is observed as 65 and 137 mrad on the left and right parts of the Φ_{LF} profile. As shown in Figure 4.22 (b, c), characteristics of the Φ_{LF} distribution obtained for Phantom 1b are noisy. Ring patterns are observed in Φ_{LF} distribution, similar to the MR magnitude image shown in Figure 4.21 (b).
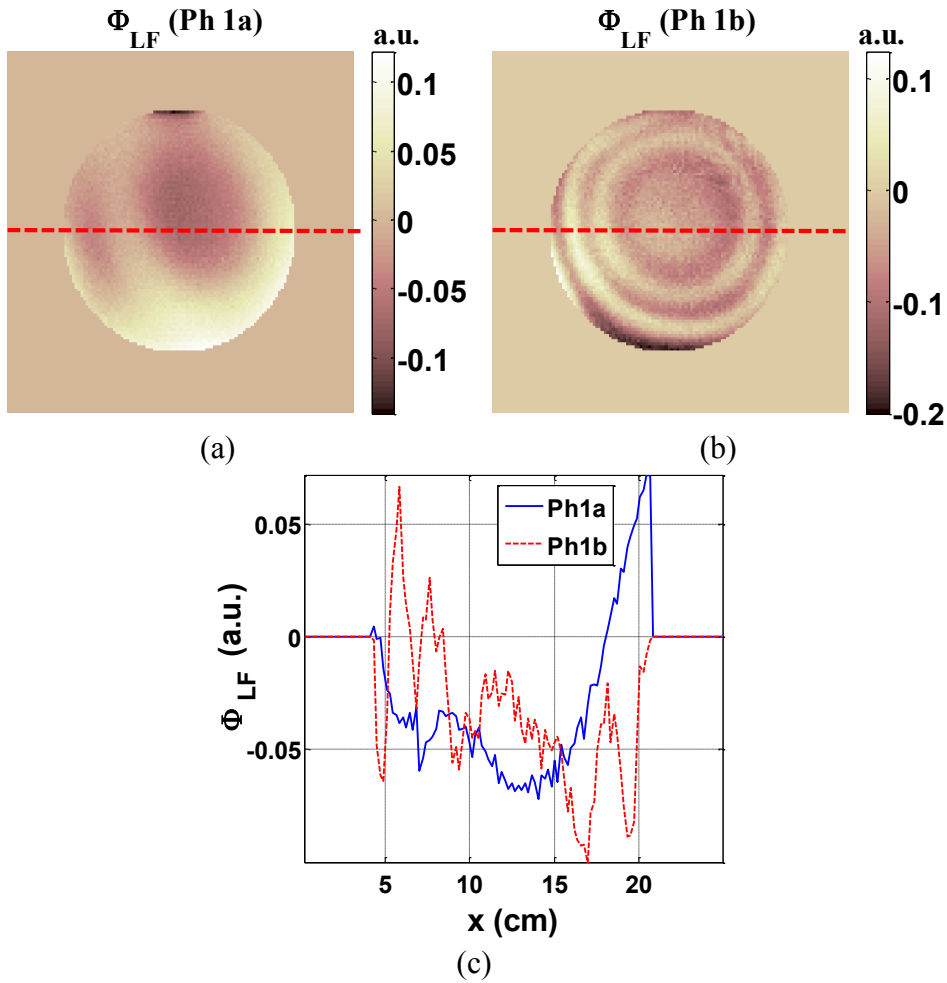
Figure 4.22 Φ_{LF} distributions (a-b) and profiles (c) acquired for Phantom 1a-b.

By using the measured Φ_{LF} distribution for Phantom 1a and J-derivative image reconstruction algorithm, $|\bar{J}_{LF}|$ and σ_{rec} images are reconstructed as shown in Figure 4.23. As shown in Figure 4.2 and Figure 4.23 (a, c), characteristics of the reconstructed $|\bar{J}_{LF}|$ image for Phantom 1a are similar to the corresponding characteristics obtained for simulation model 1. As shown in Figure 4.23 (c), $|\bar{J}_{LF}|$ changes between 50 and 300 mA/m^2 as a function of r.

80
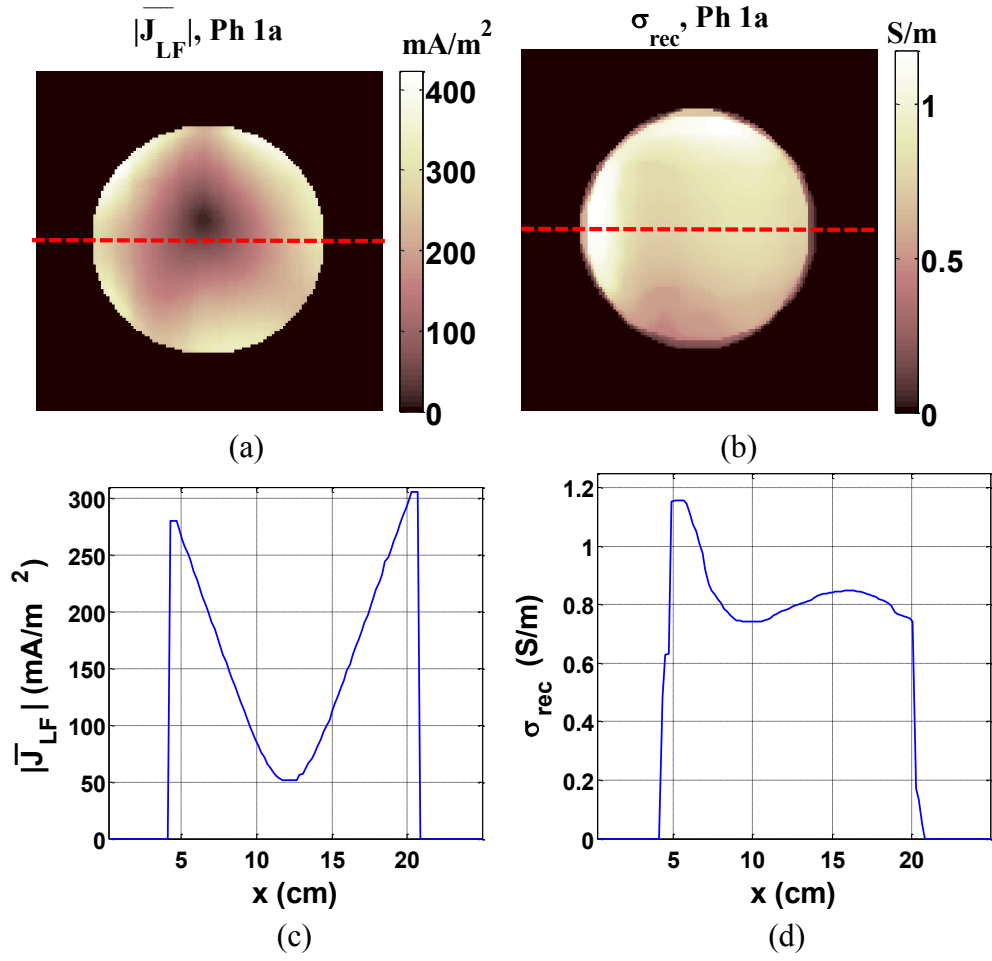
Figure 4.23 $\left|\bar{J}_{LF}\right|$ (a, c) and σ_{rec} (b, d) images and profiles reconstructed for Phantom 1a.

As shown in Figure 4.23 (b, d), σ_{rec} values are close to the true σ value of 0.83 S/m. Deviations from the true σ values are observed around the boundary of the selected slice.

$\Delta\Phi_{LF}$, $\left|\bar{J}_{LF}\right|_{max}$, $\left|\bar{J}_{LF}\right|_{avg}$, and ϵ_{σ} values of Phantom 1a are summarized in Table 4.5.

Table 4.5 $\Delta\Phi_{LF}$, $\left|\bar{J}_{LF}\right|_{max}$, $\left|\bar{J}_{LF}\right|_{avg}$, and ϵ_σ values of Phantom 1a.

$\Delta\Phi_{LF}$ (mrad)	$\left\|\bar{J}_{LF}\right\|_{max}$ (mA/m^2)	$\left\|\bar{J}_{LF}\right\|_{avg}$	ϵ_σ (%)
65	422.9	73.8	32.3

4.3.2 Experiment 2

In this experiment, Phantom 2a-d, which include saline solutions of 0.75 S/m and cylindrical inhomogeneities in gel form and composed of Agarose, TX-151, $CuSO_4$, NaCl, and distilled water are used. It is aimed to exhibit the experimental performance of ICMREIT for inhomogeneous phantoms [65]. MR magnitude images acquired for Phantom 2a-d are shown in Figure 4.24.

As shown in Figure 4.24, geometrical structure of the phantoms and the inhomogeneities are visible in MR magnitude images. MR magnitude values of the background and the inhomogeneities are 0.06 and 0.12 a.u., respectively.

Φ_{LF} distributions and profiles acquired for Phantom 2a-d are shown in Figure 4.25. As shown in Figure 4.25, the inhomogeneities are visible in measured Φ_{LF} distributions. As shown in Figure 4.25 (b, d), slope of Φ_{LF} profiles decreases inside the resistive inhomogeneities. On the other hand, slope of Φ_{LF} profiles increases inside the conductive inhomogeneities, as shown in Figure 4.25 (f, h). It is also observed that Φ_{LF} measurements are noisy at the boundary of inhomogeneities.
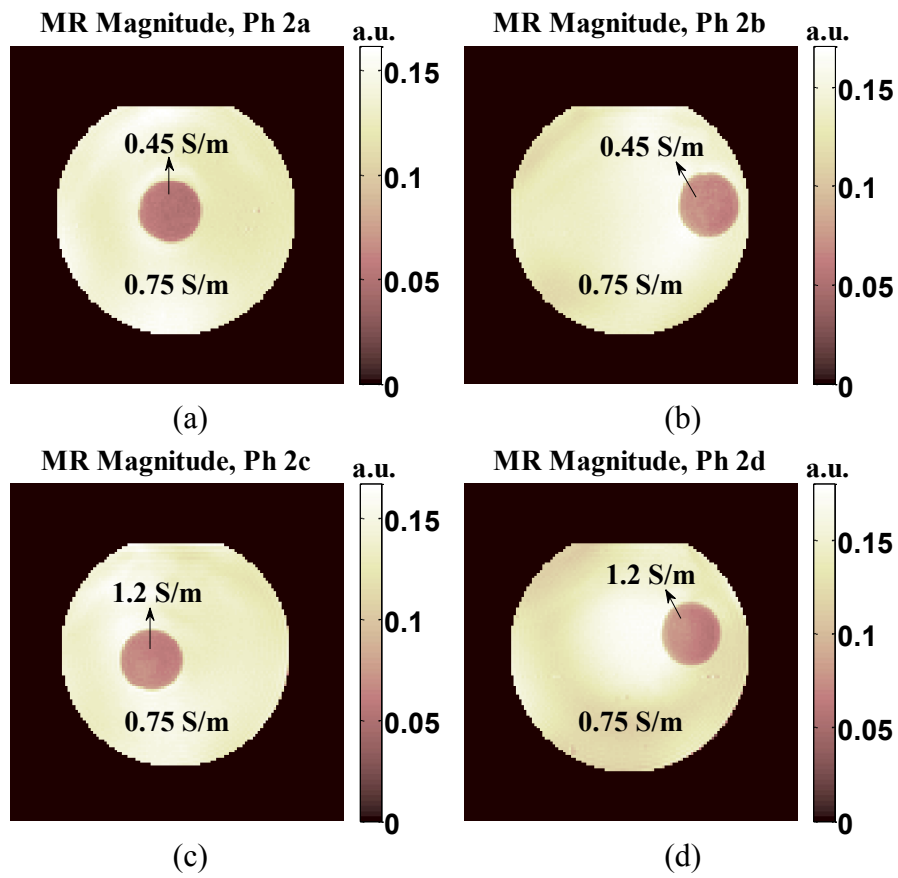
Figure 4.24 MR magnitude images acquired for Phantom 2a-d.
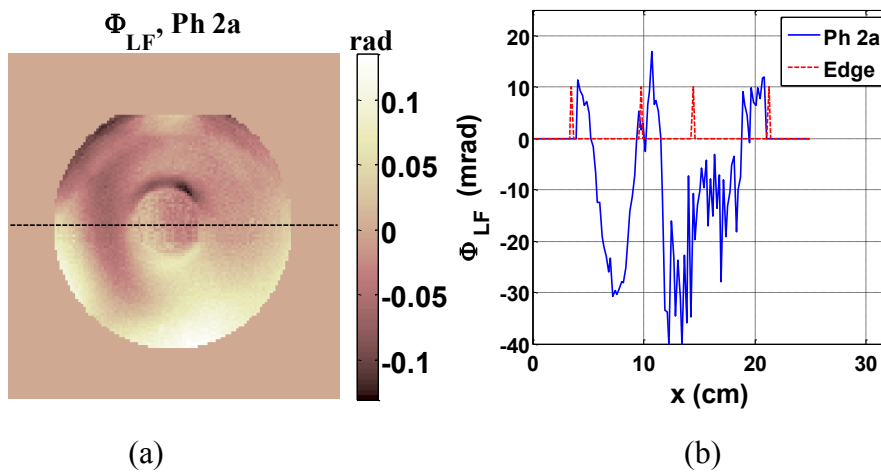
Figure 4.25 Φ_{LF} distributions and profiles acquired for Phantom 2a.
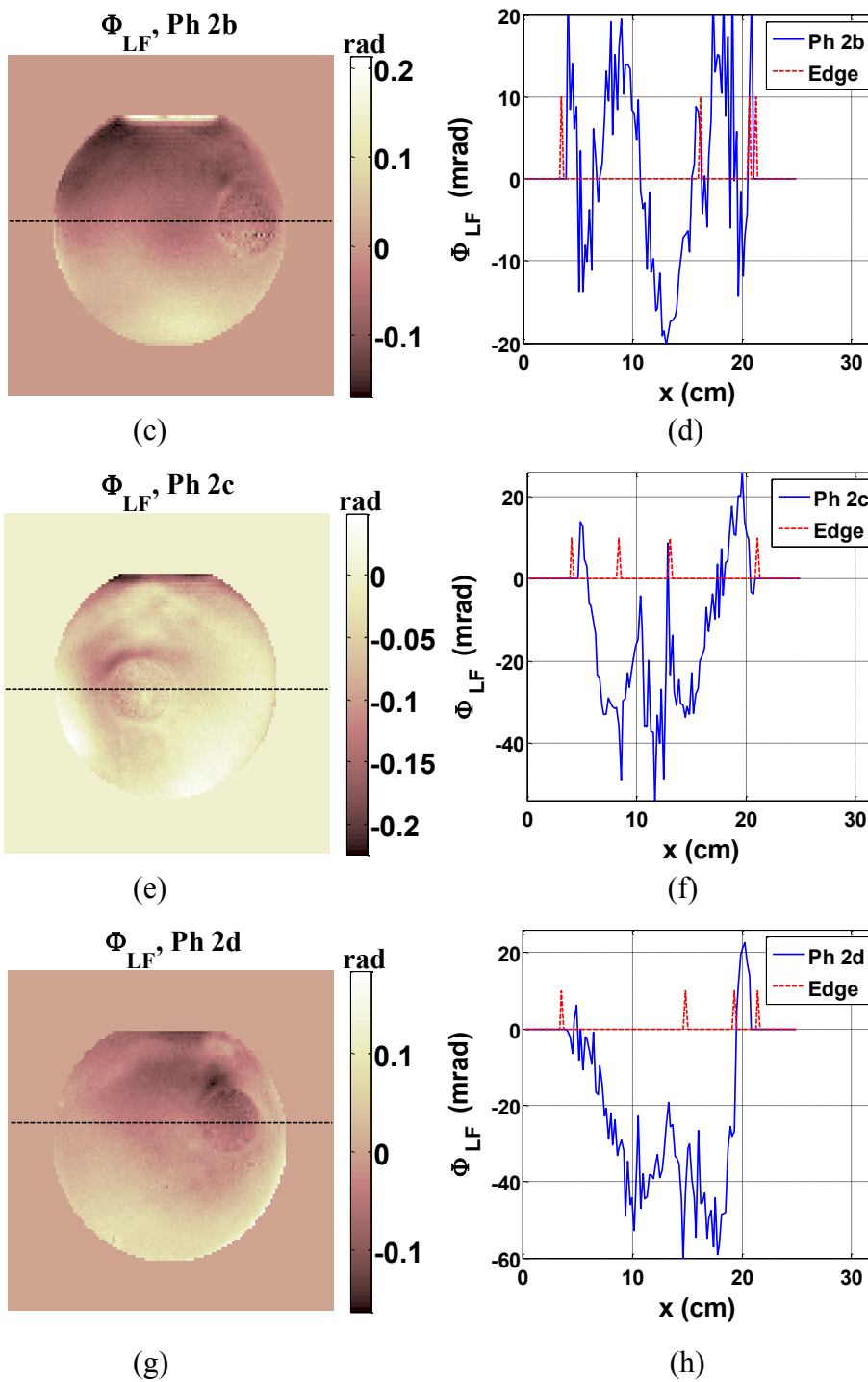
Figure 4.25 (Continued) Φ_{LF} distributions and profiles acquired for Phantom 2b-d.

$|\bar{J}_{LF}|$ images and profiles reconstructed for Phantom 2a-d are shown in Figure 4.26.

(a)

(b)

(c)

(d)
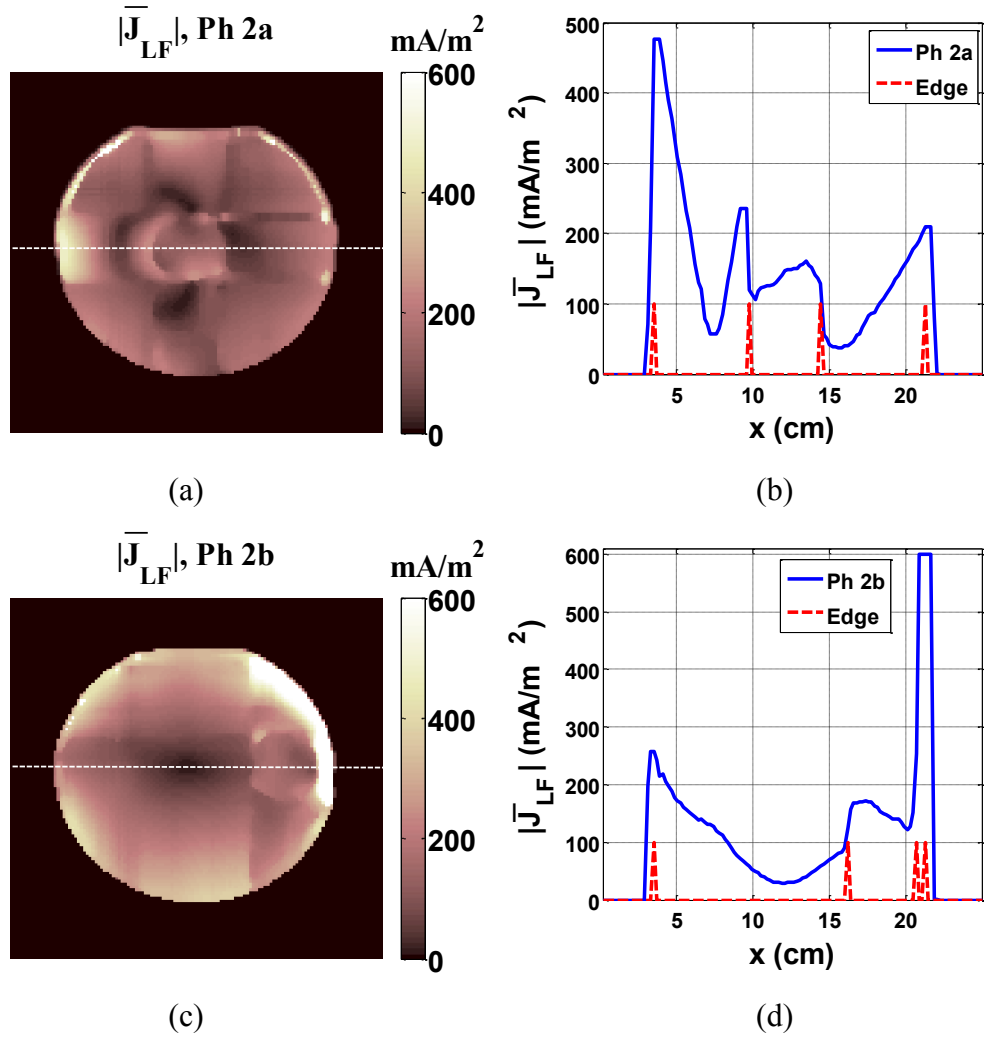
Figure 4.26 $|\bar{J}_{LF}|$ distributions and profiles reconstructed for Phantom 2a-b.

(e)

(f)

(g)

(h)
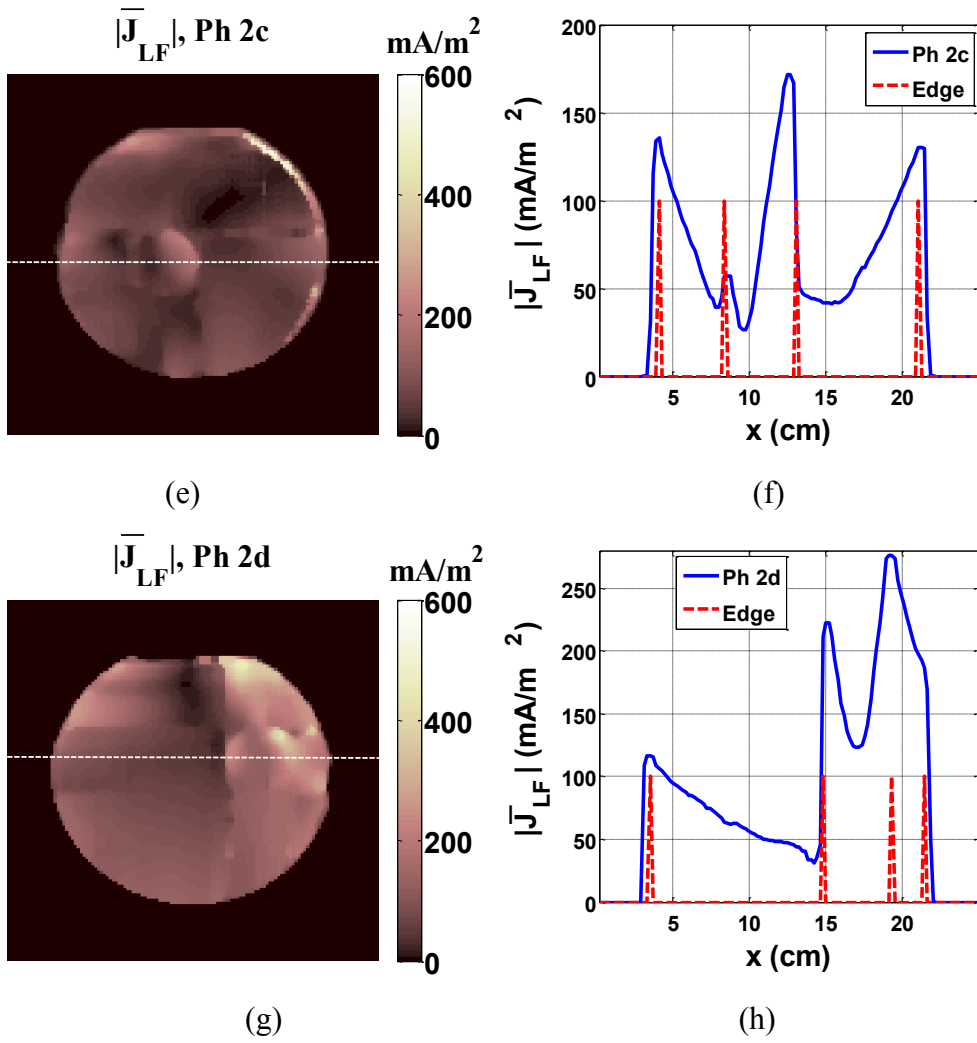
Figure 4.26 (Continued) $|\bar{J}_{LF}|$ distributions and profiles reconstructed for Phantom 2c-d.

As shown in Figure 4.26, the inhomogeneities are visible in reconstructed $|\bar{J}_{LF}|$ distributions. Sharp changes are observed at the boundary of the inhomogeneities and in the small regions located between the eccentric inhomogeneities and the phantoms. Slope of $|\bar{J}_{LF}|$ profiles decreases inside the resistive inhomogeneities and increases inside the conductive inhomogeneities

as shown in Figure 4.26 (a-b) and Figure 4.26 (c-d), respectively.

σ_{rec} images and profiles reconstructed for Phantom 2a-d are shown in Figure 4.27.

(a)

(b)

(c)

(d)

Figure 4.27 σ_{rec} distributions and profiles reconstructed for Phantom 2a-b.

σ_{rec}, Ph 2c

(e)

(f)

σ_{rec}, Ph 2d
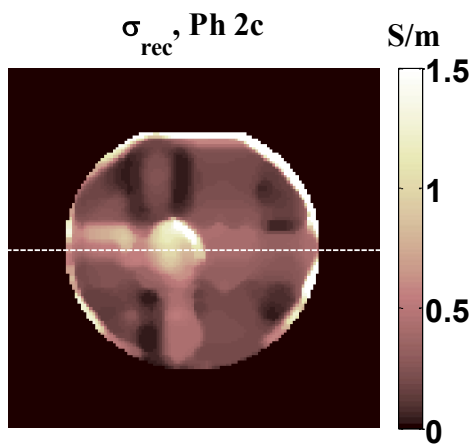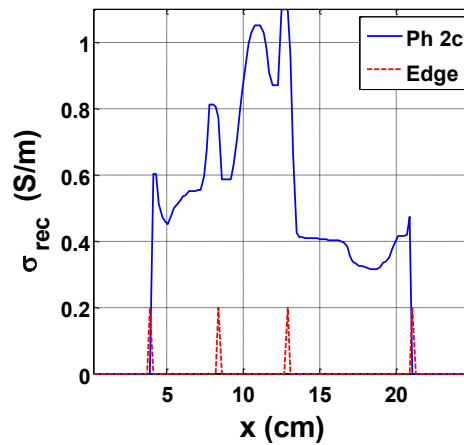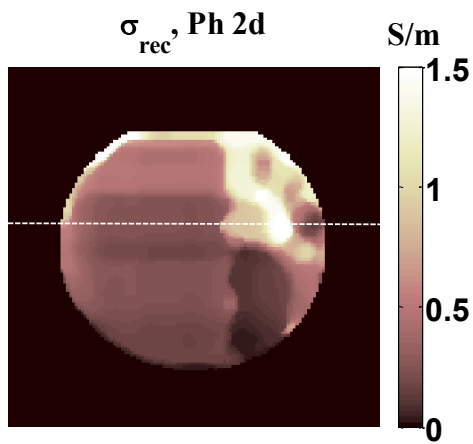
(g)
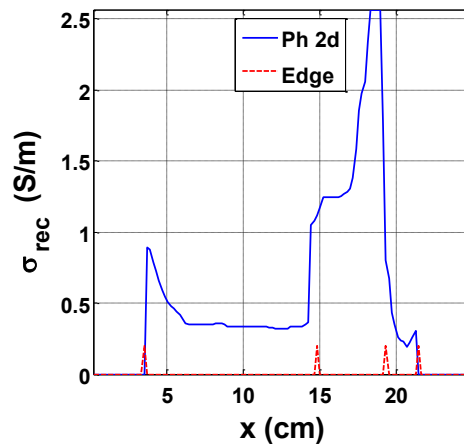
(h)

Figure 4.27 (Continued) σ_{rec} distributions and profiles reconstructed for Phantom 2c-d.

As shown in Figure 4.27, σ_{rec} images and profiles exhibit the resistive and the conductive properties of the inhomogeneities. Artifacts are observed at the boundary of the inhomogeneities and in the small regions located between the eccentric inhomogeneities and the phantoms.

$\Delta\Phi_{LF}$, $\left|\bar{J}_{LF}\right|_{max}$, $\left|\bar{J}_{LF}\right|_{avg}$, average of σ_{rec} distributions ($\sigma_{rec-avg}$) in the background and inhomogeneities, conductivity contrast ratio between the inhomogeneities and the background ($R_{ih/bg}$) and ϵ_σ values of Phantoms 2a-d are listed in Table 4.6

Table 4.6 $\Delta\Phi_{LF}$, $\left|\bar{J}_{LF}\right|_{max}$, $\left|\bar{J}_{LF}\right|_{avg}$, $\sigma_{rec-avg}$, $R_{ih/bg}$, and ϵ_σ values of Phantom 2a-d.

Ph	$\Delta\Phi_{LF}$ (mrad)	$\left\|\bar{J}_{LF}\right\|_{max}$	$\left\|\bar{J}_{LF}\right\|_{avg}$	$\sigma_{rec-avg}$ (S/m)		$R_{ih/bg}$	ϵ_σ(%)	
		(mA/m^2)		bg	ih		bg	ih
2a	57	909.3	62.8	0.7	0.5	0.7	25.5	41.3
2b	40	600.0	95.8	0.8	0.6	0.7	27.6	66.1
2c	70	624.8	29.3	0.5	0.9	2.0	64.4	43.3
2d	80	455.2	53.3	0.5	1.2	2.5	39.9	42.5

CHAPTER 5

DISCUSSION

5.1 Simulation and Experimental Results

5.1.1 Simulation 1

Simulation results in Figure 4.2-4.3 show that there is a linear relationship between r and $|\bar{J}_{LF}|$ which is consistent with (2.12). The linear relationship between r and $|\bar{J}_{LF}|$ results in quadratic characteristics between r and Φ_{LF} as shown in Figure 4.1 and expressed in (3.4-3.11). Simulation results in Figure 4.1 show that fitting quadratic polynomials to the measured B_{sz} profiles during the image reconstruction process is a reasonable approach. Due to the quadratic characteristics of Φ_{LF}, slope of Φ_{LF} profiles increase as a function of r which results in increased sensitivity of ICMREIT measurements to conductivity perturbations located at the periphery of the phantom compared to the central perturbations. It is also observed that $\Delta\Phi_{LF}$ value of 12 mrad for model 1 is very small and may be close to the phase measurement noise level of clinical MRI scanners.

As shown in Figure 4.2, error between the $|\bar{J}_{LF}|$ distributions obtained

from the numerical and the semi-analytical solutions is negligible which shows the reliability of the numerical solution method for ICMREIT. It is reasonable to take the $|\bar{J}_{LF}|$ distribution obtained from the numerical solution as the true distribution. As shown in Figure 4.3, reconstructed $|\bar{J}_{LF}|$ images at SNR=60 dB and SNR=50 dB are close to the true $|\bar{J}_{LF}|$ distribution and ϵ_J is close to 17 % at both noise levels as shown in Table 4.1. $|\bar{J}_{LF}|$ reconstructions are not affected from the noise. It is observed that the reconstruction of J_x and J_y by using only B_{sz} and neglecting x and y components of $\bar{\bar{B}}_s$ (B_{sx} and B_{sy}) results in accurate $|\bar{J}_{LF}|$ distributions for simulation model 1, which is composed of a z-gradient coil around a uniform conductor. Due to the circularly symmetric structure of simulation model 1, spatial derivatives of B_{sx} and B_{sy} ($\partial B_{sx}/\partial z$ and $\partial B_{sy}/\partial z$) are negligible which results in accurate J_x and J_y reconstructions by means of (3.2-3.3).

As shown in Figure 4.4, σ_{rec} images of simulation model 1 exhibit the electrical conductivity properties of Phantom 1. As shown in Figure 4.4 (a, c), σ_{rec} images reconstructed with J-derivative algorithm are close to the true σ values and ϵ_σ values are at low levels. It is observed that the effect of noise is suppressed by the filter shown in Figure 3.4. The reconstructions are not affected from the neglected $\partial\sigma/\partial x$ and $\partial\sigma/\partial y$ terms during the derivation of J-derivative algorithm, since Phantom 1 is uniform. In addition, accurate J_x and J_y reconstructions improve the performance of J-derivative algorithm. As shown in Figure 4.4 (b, d), σ_{rec} images reconstructed with E-calculation algorithm oscillate around the true σ values. Magnitude of oscillations increases towards the center of the selected slice due to small J_x and J_y values in this region. σ_{rec} images are affected from noise and ϵ_σ values of E-calculation

92

algorithm are almost two times greater than the ϵ_σ values of J-derivative algorithm, as shown in Table 4.1. It is clear that the performance of J-derivative algorithm is superior to the performance of E-calculation algorithm. This observation is resulted from the condition number of 588 for matrix $[A]_{N^2 \times N^2}$ of E-calculation algorithm. The performance of E-calculation algorithm can be increased by applying regularization methods for calculating the inverse of $[A]_{N^2 \times N^2}$.

5.1.2 Simulation 2

As shown in Figure 4.5-4.6, vertical $\left|\bar{J}_{LF}\right|$ and Φ_{LF} profiles of simulation model 4, which includes the y-gradient coil around a uniform phantom, have quadratic and cubic characteristics since the B_{pz} distribution of y-gradient coil is linearly related with y coordinates. These observations are consistent with (3.11) and show that fitting cubic polynomials to the vertical B_{sz} profiles during the image reconstruction process is a reasonable approach. Due to the cubic characteristics of vertical Φ_{LF} profiles, $\left|\bar{J}_{LF}\right|$ values increase towards the center of the selected slice. $\Delta\Phi_{LF}$ value of simulation model 4 is 1.7 times smaller than the corresponding value of simulation model 1. This observation is resulted from the B_{pz} distribution of the y-gradient coil with non-uniform polarity. Due to the Faraday's Law of electromagnetic induction, $\bar{J}_{LF}$ is related with $-\partial B_{pz}/\partial t$. Therefore, a B_{pz} distribution with non-uniform polarity induces $\bar{J}_{LF}$ vectors rotating in opposite polarities which result in reduced B_{sz} and Φ_{LF} distributions. It can be concluded that the use of a coil with uniform B_{pz} polarity throughout the object to be imaged is advantageous for ICMREIT. From this perspective, it is clear that the use of the z-gradient coil for ICMREIT is more proper than the use of the y-gradient coil.

As shown in Figure 4.6, reconstructed $\left|\bar{J}_{LF}\right|$ images of model 4 exhibit the characteristics of the true $\left|\bar{J}_{LF}\right|$ distribution, in general. However, error between the reconstructed and the true $\left|\bar{J}_{LF}\right|$ distributions is large. ϵ_J is close to 400 %. The main source of the error between the reconstructed and the true $\left|\bar{J}_{LF}\right|$ distributions is the neglected B_{sx} and B_{sy} distributions of the y-gradient coil during the reconstruction of J_x and J_y distributions. Since the simulation geometry is not circularly symmetric, the contribution of B_{sx} and B_{sy} to $\bar{J}_{LF}$ is not negligible. The effect of noise is visible at $y =0$ line, on which B_{sz} values are close to zero. As shown in Figure 4.7, quality of σ_{rec} images of model 4 is very low. An artifact is observed at $y =0$. σ_{rec} values oscillate around the true σ values. As shown in Table 4.1-4.2, ϵ_σ values of model 4 calculated at SNR=60 dB and SNR=50 dB are 2.64 and 2.77 times greater than the corresponding values of model 1. Erroneous reconstruction of J_x and J_y distributions is the main reason of the low quality of σ_{rec} images.

J-derivative image reconstruction algorithm is capable of reconstructing anisotropic conductivity distributions as shown in (2.38-2.47). In order to reconstruct a $\underline{\sigma}$ distribution of two elements (i.e. σ_{xx} and σ_{yy}), two coils with linearly independent B_{pz} distributions are necessary. The use of z and y gradient coils, which are readily available in MRI scanners, is an alternative for the realization of anisotropic conductivity reconstruction in ICMREIT. Simulation results shown in Figure 4.4 and Figure 4.7 show that σ_{rec} images reconstructed for the z-gradient coil are promising, whereas σ_{rec} images reconstructed for the y-gradient coil are insufficient. In order to realize anisotropic conductivity reconstruction with z and y-gradient coils of MRI scanners, $\bar{J}_{LF}$ distributions of y-gradient coils should be reconstructed with better accuracy.

94

5.1.3 Simulation 3

As shown in Figure 4.8 and Figure 4.10, horizontal $|\bar{J}_{LF}|$ and Φ_{LF} profiles of simulation model 2a-d, which include the z-gradient coil with inhomogeneous phantoms, have linear and quadratic characteristics in the background and the inhomogeneities of the phantoms. Therefore, it can be concluded that fitting quadratic polynomials to the Φ_{LF} profiles of inhomogeneous phantoms between the edge points of the background and the inhomogeneities is a reasonable approach. $|\bar{J}_{LF}|$ changes as a function of $\Delta\sigma$ inside the inhomogeneities which affects the slope of Φ_{LF} profiles. The slope of Φ_{LF} profiles increases in the conductive inhomogeneities, whereas Φ_{LF} slope decreases in the resistive inhomogeneities. $\Delta\Phi_{LF}$ values are close to 9 mrad, which is 75 % of the corresponding value of model 1. The ratio between the $\Delta\Phi_{LF}$ values of model 2a-d and model 1 is equal to the ratio between the background σ values which shows that Φ_{LF} is linearly related with σ.

As shown in Figure 4.9-4.10, reconstructed $|\bar{J}_{LF}|$ images of model 2a-d are close to the true $|\bar{J}_{LF}|$ distribution which exhibits the success of $\bar{J}_{LF}$ reconstruction for the z-gradient coil with inhomogeneous phantoms. Error between the reconstructed and the true $|\bar{J}_{LF}|$ values increases at the boundary of the inhomogeneities and in the small region located between the boundary of the eccentric inhomogeneities and the phantoms. Error of the reconstructed $|\bar{J}_{LF}|$ images at the boundary of the inhomogeneities is resulted from the sharp changes in $|\bar{J}_{LF}|$ values due to $\Delta\sigma$ between the inhomogeneities and the background. The source of the error in the small region located between the boundary of the eccentric inhomogeneities and the phantoms is insufficient

modeling of Φ_{LF} profiles in these regions. The fitted polynomials in these small regions do not represent the exact characteristics of true Φ_{LF} profiles. As shown in Table 4.1 and Table 4.3, ϵ_J values of model 2 increase as SNR of Φ_{LF} measurements decrease, different from relatively constant characteristics of the corresponding values calculated for model 1. Noise dependent characteristics of the reconstructed $|\bar{J}_{LF}|$ images of model 2a-d are due to the decreased sensitivity of Φ_{LF} measurements of model 2a-d, compared to the Φ_{LF} measurements of model 1. Simulation results show that $|\bar{J}_{LF}|$ images exhibit the electrical conductivity properties of the phantoms. Therefore, $|\bar{J}_{LF}|$ images can be utilized as the output of an imaging method entitled as induced current magnetic resonance current density imaging (ICMRCDI) [75].

As shown in Figure 4.11-4.12, σ_{rec} images of simulation model 2a-d exhibit the electrical conductivity properties of Phantom 2a-d. Resistive and conductive inhomogeneities can be distinguished from the background of σ_{rec} images and σ_{rec} values are close to the true σ values in the background and the inhomogeneities of the phantoms. In σ_{rec} images, artifacts are observed around the inhomogeneities and in the small regions located between the boundary of the eccentric inhomogeneities and the phantoms. These artifacts due to the error in $\bar{J}_{LF}$ reconstructions and neglected $\partial\sigma/\partial x$ and $\partial\sigma/\partial y$ terms during the derivation of the J-derivative algorithm are carried over the horizontal and the vertical profiles passing through the inhomogeneities due to the curve fitting operation. Similar to the ϵ_J values, $\epsilon_{\sigma-g}$ and $\epsilon_{\sigma-l}$ values of model 2 increase as SNR of Φ_{LF} measurements decreases as shown in Table 4.3. $\epsilon_{\sigma-g}$ values of model 2 are greater than ϵ_σ of model 1, due to the decreased sensitivity of Φ_{LF} measurements for model 2. It is also observed that $\epsilon_{\sigma-l}$ values are greater than

$\epsilon_{\sigma-g}$ values due to the smaller range of Φ_{LF} measurements inside the inhomogeneities compared to the background.

5.1.4. Simulation 4

As shown in Figure 4.13-4.17, characteristics of Φ_{LF}, $|\overline{J}_{LF}|$, and σ_{rec} distributions of model 3a-d, which are composed of the z-gradient coil with phantoms including small inhomogeneities, are similar to the corresponding characteristics of model 2a-d. As shown in Figure 4.15, the error between the reconstructed and the true $|\overline{J}_{LF}|$ values increases inside the inhomogeneities and the small regions located between the boundary of the inhomogeneities and the phantoms. In these regions, $|\overline{J}_{LF}|$ reconstruction error is due to the insufficiency of curve fitting operation and increased noise effects due to the reduced sensitivity of Φ_{LF} measurements in small cylindrical inhomogeneities with a diameter of 2 cm. It is also observed that $|\overline{J}_{LF}|$ reconstruction error in concentric inhomogeneities is greater than the corresponding error in eccentric inhomogeneities due to the position dependent sensitivity of Φ_{LF} measurements.

As shown in Figure 4.16-4.17, visibility of the inhomogeneities is low in σ_{rec} images of model 3a-d, compared to the σ_{rec} images of model 2a-d, due to the small size of the inhomogeneities. The noise affects the visibility of the inhomogeneities. As shown in Table 4.4, $\epsilon_{\sigma-g}$ and $\epsilon_{\sigma-l}$ increase as SNR of Φ_{LF} measurements decreases. It is very difficult to distinguish the inhomogeneities from the background for the σ_{rec} images reconstructed at SNR=50 dB. It is also observed that the visibility of eccentric inhomogeneities is greater than the visibility of concentric inhomogeneities due to the position

dependent sensitivity of Φ_{LF} measurements. Smaller $\epsilon_{\sigma-l}$ values of eccentric inhomogeneities compared to the $\epsilon_{\sigma-l}$ values of the concentric inhomogeneities verify this observation. σ_{rec} images of model 3a-d also show that imaging small inhomogeneities with ICMREIT is very difficult since spatial resolution is decreased due to the presence of the smoothing filter in the image reconstruction process.

5.1.5 Results of the sensitivity and the distinguishability analyses

The results of the analysis in Figure 4.18 show that sensitivity of ICMREIT to central conductivity perturbations is smaller than sensitivity of ICMREIT to eccentric conductivity perturbations. This observation is resulted from the linear relationship between $\bar{J}_{LF}$ and r as expressed in (2.12). For central inhomogeneities, $\left|\bar{J}_{LF}\right|$ is small due to small r values of the locations inside the inhomogeneities. Low sensitivity of ICMREIT to central conductivity perturbations is a major disadvantage of ICMREIT. Simulation results show that resistive inhomogeneities focus $\bar{J}_{LF}$ in regions between the boundary of the inhomogeneity and the conductor. Large $\left|\bar{J}_{LF}\right|$ values near the boundary of the resistive inhomogeneities increase the sensitivity of ICMREIT measurements. As a result, sensitivity of ICMREIT measurements to resistive ($\Delta\sigma < 0$) perturbations is greater than the sensitivity of ICMREIT measurements to conductive ($\Delta\sigma > 0$) perturbations.

The results of the analysis in Figure 4.19 show that distinguishability of a concentric inhomogeneity increases as ρ_{ih} and $\Delta\sigma$ of the inhomogeneity increase. This observation is resulted from the increasing characteristics of $\left|\bar{J}_{LF}\right|$

with r. As the size of a concentric inhomogeneity increases, the average value of $|\bar{J}_{LF}|$ and the resultant $|\Delta B_z(x,y)|_{avg}$ value of the inhomogeneity increase. Due to the linear relationship between $|\bar{J}_{LF}|$ and r, it is very difficult to image small concentric inhomogeneities. It is also observed that distinguishability of a concentric inhomogeneity is the same for resistive and conductive cases due to the circularly symmetric structure of the conductor and the inhomogeneities with respect to the z-gradient coil.

The results of the analysis in Figure 4.20 show that distinguishability of the resistive eccentric inhomogeneities is greater than the distinguishability of conductive eccentric inhomogeneities. This observation is resulted from the $\bar{J}_{LF}$ focusing properties of resistive eccentric inhomogeneities in small regions located between the boundary of the conductor and the inhomogeneities. Large $|\bar{J}_{LF}|$ values near the inhomogeneity generate large $|\Delta B_z(x,y)|_{avg}$ values inside the inhomogeneity which increase the distinguishability. It is also observed that distinguishability of eccentric inhomogeneities is greater than distinguishability of concentric inhomogeneities, which is resulted from the linear relationship between $|\bar{J}_{LF}|$ and r.

5.1.6 Experiment 1

The first experiment is performed by using Phantom 1a and Phantom 1b, which have uniform σ distributions of 0.83 S/m and 1.48 S/m. As shown in Figure 4.23, MR and k-space magnitude values of Phantom 1a are a single order of magnitude greater than the corresponding values of Phantom 1b. It is also observed that MR magnitude image of Phantom 1b has ring patterns.

Reduced signal strength of Phantom 1b may be resulted from the excessive Φ_{RF} created due to the high σ value of the phantom. In MRI, B_1 field, which is focused on x and y directions, induces RF eddy current ($\bar{J}_{RF}$) in yz and xz slices of the object to be imaged. $\bar{J}_{RF}$, which is the source of Φ_{RF}, can be evaluated by considering the cylindrical geometry shown in Figure 5.1.
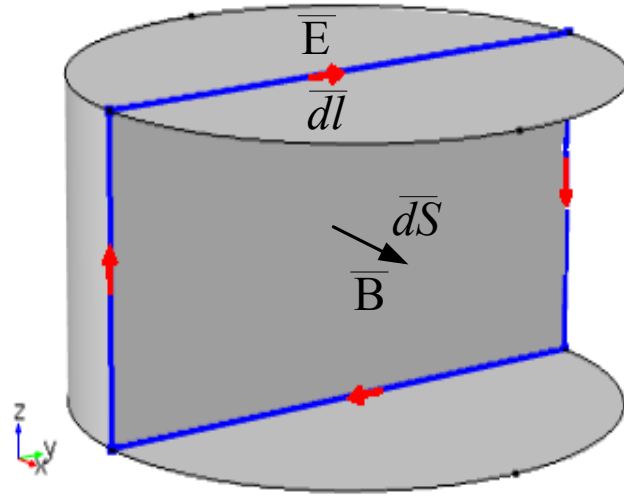
Figure 5.1 A cylindrical object and a $\overline{B}$ distribution focused on x direction. Half of the cylinder is not shown for visualization. $\overline{dl}$ and $\overline{dS}$ are differential line and surface elements. Blue line shows the line integration path.

The relationship between $\overline{E}$ and $\overline{B}$ in Figure 5.1 can be expressed by using the Faraday's Law as

$$\oint_L \overline{E}(x,y,z) \cdot \overline{dl} = -\int_S j\omega B(x,y,z)\hat{a}_x \cdot \overline{dS}. \qquad (5.1)$$

Using (5.1), L_2 norm of $\overline{E}$ ($|\overline{E}|$) can be expressed as

$$|\overline{E}| = \omega|\overline{B}|\frac{\pi r h}{(2r+h)}, \tag{5.2}$$

where r and h are the radius and the height of the cylinder, and $|\overline{B}|$ is L_2 norm of $\overline{B}$, respectively. Using the Ohm's Law, L_2 norm of $\overline{J}_{RF}$ ($|\overline{J}_{RF}|$) can be expressed as

$$|\overline{J}_{RF}| = \sqrt{\sigma^2 + \omega^2\varepsilon^2}|\overline{E}| = \omega|\overline{B}|\sqrt{\sigma^2 + \omega^2\varepsilon^2}\frac{\pi r h}{(2r+h)}, \tag{5.3}$$

where $\sqrt{\sigma^2 + \omega^2\varepsilon^2}$ is the complex conductivity of the cylinder. As shown in Figure (5.3), $|\overline{J}_{RF}|$ increases as a function of σ, r and h. Therefore, imaging a phantom with large σ, r and h values by using the proposed MRI pulse sequence for ICMREIT may create excessive Φ_{RF} which reduce the signal strength and SNR since excessively phased spins get out of the k-space sampling window. It can be concluded that the realization of ICMREIT with the proposed MRI pulse sequence is not possible for phantoms with large σ, r and h values.

Φ_{LF} distribution of Phantom 1b is not taken into consideration since the signal strength of this phantom is at a low level. On the other hand, characteristics of the Φ_{LF} distribution of Phantom 1a are similar to the characteristics of Φ_{LF} distribution of simulation model 1 as shown in Figure 4.1 and Figure 4.22. Measured $\Delta\Phi_{LF}$ value is 5.42 times greater than the corresponding value of simulation model 1. $|\overline{J}_{LF}|$ and σ_{rec} images reconstructed with the measured Φ_{LF} distribution exhibit the electrical conductivity properties of Phantom 1a as shown in Figure 4.23. Reconstructed $|\overline{J}_{LF}|$ image is linearly related with r and σ_{rec} image is close to the true σ distribution.

5.1.7 Experiment 2

In physical experiments, inhomogeneous phantoms are also investigated as shown in Figure 4.24-4.27. As shown in Figure 4.24, cross sectional geometries of Phantom 2a-d are observed in MR magnitude images. MR magnitude images do not include ring artifacts which show the reliability of the proposed MRI pulse sequence for imaging the electrical conductivity properties of Phantom 2a-d. As shown in Figure 4.25, the inhomogeneities are visible in measured Φ_{LF} distributions. Slope of Φ_{LF} profiles changes in accordance with the σ values of the background and the inhomogeneities. Φ_{LF} profiles have noisy behaviour especially in the regions close to the boundary of the inhomogeneities. Due to the noisy characteristics of the measured Φ_{LF} profiles, application of the curve fitting method can be considered as a reasonable approach.

Reconstructed $|\bar{J}_{LF}|$ and σ_{rec} images shown in Figure 4.26-4.27 exhibit the electrical conductivity properties of Phantom 2a-d. Linear dependence of $|\bar{J}_{LF}|$ with r is observed in the background of the reconstructed $|\bar{J}_{LF}|$ images as shown in Figure 4.26. The slope of $|\bar{J}_{LF}|$ profiles changes in accordance with the σ values of the background and the inhomogeneities. It can be concluded that the characteristics of the measured and the simulated $|\bar{J}_{LF}|$ images are similar. Sharp changes in $|\bar{J}_{LF}|$ values are observed at the boundary of the inhomogeneities and reconstruction quality is low in the region located between the eccentric inhomogeneities and phantoms. Low reconstruction quality is resulted from the neglected B_{sx} and B_{sy} distributions during the reconstruction process and insufficiency of the fitted polynomials in small regions. As shown in Figure 4.27, σ_{rec} images are rough estimates of the true σ distributions of

Phantom 2a-d. $\sigma_{rec-avg}$ and $R_{ih/bg}$ values listed in Table 4.6 exhibit the resistive and the conductive properties of the inhomogeneities with respect to the background. Artifacts are observed at the boundary of the inhomogeneities due to the neglected $\partial\sigma/\partial x$ and $\partial\sigma/\partial y$ terms during the derivation of the J-derivative algorithm. Error of J_x and J_y distributions due to the neglected B_{sx} and B_{sy} distributions also reduces the reconstruction quality in the regions located between the boundary of the eccentric inhomogeneities and the phantoms. ϵ_σ values listed in Table 4.6 are close to the simulated ϵ_σ values which show that the proposed method provides reasonable results in general. Simulation and experimental results show that implementation of J-derivative algorithm has drawbacks related with the calculation of $\bar{J}_{LF}$ by using only z component of $\overline{B}_s$, neglecting spatial derivatives of σ, and application of the smoothing filter. In order to overcome the drawbacks of the proposed current density ($\bar{J}$) based image reconstruction method, $\overline{B}$ based algorithms may be used. The well-known MREIT sensitivity algorithm [25] can be utilized for this purpose [76].

Simulation and experimental results show that the concept of ICMREIT is realized for simple phantoms including a single inhomogeneity by using the readily available z-gradient coil of a clinical MRI scanner without the utilization of an external hardware. It is observed that sensitivity of the method is low and the measurements are prone to noise. Therefore, it will be difficult to realize ICMREIT with complex phantoms. In experiments, we use the z-gradient coil, since it provides a symmetric geometry and a uniform B_{pz} distribution throughout the phantoms. In addition to the z-gradient coil, x and y gradient coils can be used separately or in pairs, to realize ICMREIT.

5.2 Comparison of Conventional MREIT and ICMREIT with Respect to Safety

The major problem of conventional MREIT is the necessity of injecting electrical current to body. Arpınar et al. [40] state that injection current is limited by the patient auxiliary current limit of 100 μA in IEC 60601-2-33 standard [43]. In order to use MREIT in clinical applications, injection current should be decreased to this limit. In research and development studies, the amplitude of injection current for MREIT is far beyond the patient auxiliary current limit and ranges between several mA [35-36, 39-40], to tens [37], and hundreds [39] of mA. By utilizing relatively high injection current amplitudes in MREIT experiments, successful conductivity images are reconstructed [32-42]. Reconstruction quality of MREIT decreases as the injection current amplitude decreases to the level of patient auxiliary current limit [40]. High injection current results in high J values throughout the object to be imaged. Lee et al. apply bipolar current of 28 mA and 300 ms duration to a saline phantom with a sausage inhomogeneity and reconstruct J values between 10 A/m^2 and 25 A/m^2 in the background and 5 A/m^2 inside the inhomogeneity [77]. These values are at least a single order of magnitude greater than the reconstructed $\left|\bar{J}_{LF}\right|$ values in ICMREIT experiments. By using $\left|\bar{J}_{LF}\right|_{max}$ measurements listed in Table 4.6, maximum $\left|\bar{E}\right|$ value ($\left|\bar{E}\right|_{max}$) is calculated as 1.2 V/m. The calculated $\left|\bar{E}\right|_{max}$ value is below the electric field limit of 3.75 V/m at 1 kHz [43, 78]. Therefore, ICMREIT can be considered as a safe method [65].

5.3 Problems and Limitations of ICMREIT

Simulation and experimental results show that measured Φ_{LF} and $|\bar{J}_{LF}|$ distributions are greater than the simulated Φ_{LF} and $|\bar{J}_{LF}|$ distributions. We think that the major source of the difference between the simulated and the experimental measurements is the low sensitivity of ICMREIT, which can be considered as a major concern for clinical applications. In addition, the mathematical model we use in numerical simulations may not represent the exact characteristics of the utilized MRI scanner in experiments. For example, oscillating gradient fields during the application of the proposed pulse sequence for ICMREIT may result in vibrations in the gradient coils of the MRI scanner as a result of the presence of Lorentz forces [65, 79]. The frequency of these vibrations may be comparable to the frequency of the oscillating gradients and these vibrations may create an additional $\partial B/\partial t$ source which may induce $\bar{J}_{LF}$ in the object to be imaged. $\bar{J}_{LF}$ induced by the vibrations has potential to contribute to the Φ_{LF} distribution by means of the MRI pulse sequence used in ICMREIT experiments [65].

The main reason of the low sensitivity of ICMREIT measurements is the low frequency of the oscillating gradient fields used in ICMREIT experiments [65]. On the other hand, MR-based high frequency electric properties imaging method have been utilized since the beginning of 1990s [80]. These methods, which use the B_1 field distribution of RF coils of MRI scanners, are commonly referred to as B_1 mapping [80-83]. In MRI, $\bar{J}_{RF}$ is induced in the object to be imaged due to σ and ε distributions of the object as shown in (5.3). Due to the induced $\bar{J}_{RF}$ distribution, B_1 distribution throughout the object is changed. By measuring this altered B_1 distribution, σ and ε properties of the objects are

extracted. The change in B_1 distribution throughout the object is high due to the induced $\bar{J}_{RF}$ distributions at the Larmor frequency. As a result, the reconstruction performance of B_1 mapping methods is very high [80-83].

The frequency of MR gradient coil based ICMREIT is limited by *SR* of MRI scanners. By utilizing higher *SR* values, t_r can be reduced which increases B_{sz_peak} and decreases $T_s = 2 \times t_r$. The increase in B_{sz_peak} and decrease in T_s compensate each other. If N_{cycle} of the proposed MRI pulse sequence is kept constant, the accumulated Φ_{LF} does not change as shown in (2.49). In theory, by using smaller t_r values, more gradient pulses can be included in the proposed MRI pulse sequence and Φ_{LF} can be increased as a result of the increase in N_{cycle} value. However, in practice, T_{plt} of the gradient pulses is much greater than t_r, since the duration of soft 180° RF pulses applied with the gradient waveform is in the order of 2.5 ms. Therefore, greater N_{cycle} values increase T_E which result in decreased signal strength and SNR. The proposed MRI pulse sequence with higher N_{cycle} values includes higher number of 180° RF pulses which increase the specific absorption rate (SAR) [65].

During t_r of the proposed MRI pulse sequence for ICMREIT, $\bar{J}_{LF}$ is induced in the conductive parts of the MRI scanner [53, 55, 65]. The induced $\bar{J}_{LF}$ distribution in the conductive parts of the MRI scanner is referred to as LF system eddy current distribution ($\bar{J}_{LF-sys}$) [55]. $\bar{J}_{LF-sys}$ may contribute to the measured Φ_{LF} distributions by means of the proposed MRI pulse sequence for ICMREIT. Today, many MRI pulse sequences include time varying gradients. For example, in echo-planar imaging (EPI) applications, read-out gradient is rapidly switched in order to sample the k-space in a short time period and

106

reduce the total imaging time [84-85]. In order to reduce the MR phase contribution of $\bar{J}_{LF-sys}$ during the application of the MRI pulse sequences that include time varying gradients, active shielding [86-87] and eddy current compensation methods [88-91] are used. Temporal characteristics of $\bar{J}_{LF-sys}$ can be modeled by using resistive-inductive (RL) series circuit. By using the series RL circuit model, time variation of $\bar{J}_{LF-sys}$ can be expressed as

$$\bar{J}_{LF-sys}(t) = \bar{J}_{LF-sys}^{ss} + [\bar{J}_{LF-sys}(0) - \bar{J}_{LF-sys}^{ss}] \ e^{-t/\tau}, \qquad (5.4)$$

where $\bar{J}_{LF-sys}^{ss}$ and $\bar{J}_{LF-sys}(0^-)$ are the steady state and the initial values of $\bar{J}_{LF-sys}$, respectively and τ is the time constant of the model. τ can be expressed as

$$\tau = \frac{L_{sys}}{R_{sys}}, \qquad (5.5)$$

where L_{sys} and R_{sys} are the effective inductance and the resistance of the system, respectively.

Zhou and King state that although $\bar{J}_{LF-sys}$ distributions of MRI scanners have various τ constants due to different coupling effects, many MRI scanners have τ constants between 1 and 20 ms, which contribute to the MR phase contrast [91]. For the MRI pulse sequence proposed for ICMREIT, $\bar{J}_{LF-sys}^{ss}$ increases as a function of the SR of the gradient waveform since $\bar{J}_{LF-sys}$ is related with $-\partial B/\partial t$, due to the Faraday's Law of electromagnetic induction.

$\bar{J}_{LF-sys}$ can reach $\bar{J}_{LF-sys}^{ss}$ after a time period of 5τ, which is in the order of 5 and 100 ms, by considering the eddy current time window presented by Zhou and King [91]. Since $\tau \gg t_r$, $\bar{J}_{LF-sys}$ cannot reach $\bar{J}_{LF-sys}^{ss}$ during the gradient pulses of the MRI pulse sequence for ICMREIT.

Let us consider the application of the MRI pulse sequence for ICMREIT twice, with t_r values of 300 and 30 μs. Considering these t_r values, $\bar{J}_{LF-sys}^{ss}$ values of the first and the second gradient waveforms can be considered as 1 and 10 per units (pu), respectively. By using (5.4), assuming $\bar{J}_{LF-sys}(0) = 0$ pu, and $\tau = 10$ ms, $\bar{J}_{LF-sys}(t_r)$ values can be calculated as 0.03 pu for both gradient waveforms. This observation shows that temporal variation of $\bar{J}_{LF-sys}$ during t_r can be modeled with a simple ramp function [92] as

$$\bar{J}_{LF-sys}(t) = \frac{\bar{J}_{LF-sys}^{ss}}{\tau} t. \qquad (5.6)$$

As shown in (5.6), adjusting the SR does not change $\bar{J}_{LF-sys}(t_r)$ since $\bar{J}_{LF-sys}^{ss}$ and t_r are directly and inversely proportional with SR, respectively. However, using higher SR values in an MRI pulse sequence increases the risk of neuro-muscular stimulation [92-93] in clinical applications and it may push the gradient amplifier of the MRI scanner towards its maximum limits. Therefore, it is proper to use low SR values for the MRI pulse sequence for ICMREIT.

Another alternative for increasing Φ_{LF} measurements is to use a bipolar gradient waveform with hard 180° RF pulses [63] as shown in Figure 5.2. The MRI pulse sequence shown in Figure 5.2 and the utilized MRI pulse sequence

shown in Figure 2.2 have the same principles for inducing $\bar{J}_{LF}$ in the object to be imaged and accumulating Φ_{LF} in MR signal. The use of a bipolar gradient waveform and suitable 180° RF pulses with hard envelopes are the distinctive features of the MRI pulse sequence shown in Figure 5.2. Since the MRI pulse sequence shown in Figure 5.2 has a bipolar gradient waveform, T_s is increased to $4 \times t_r$, which results in two times increase in Φ_{LF} measurements with the same N_{cycle} value.

The major difficulty of the MRI pulse sequence with a bipolar gradient waveform is the necessity of applying hard 180° RF pulses with positive and negative gradient pulses. In practice, duration of hard 180° RF pulses cannot be very small due to the limited RF power. For example, the shortest duration of hard 180° RF pulses of the utilized MRI scanner is 700 μs. Due to the limited RF power, hard 180° RF may not function ideally. It is observed that hard pulses applied with positive and negative gradients excite symmetric slices with respect to the gradient iso-center. In order to select the same slice during the application of the pulse sequence shown in Figure 5.2, the selected slice must be on the gradient iso-center which reduces the sensitivity of Φ_{LF} measurements. In addition, it is observed that hard 180° RF pulses applied with positive and negative gradient pulses result in ring type artifacts in MR magnitude images as shown in Figure 5.3.

Actually, the use of non-ideal hard 180° RF pulses with the MRI pulse sequences shown in Figure 2.2 and Figure 5.2 results in MR phase artifacts due to the cross-talk of the of the neighbor slices. It is observed that cross talk effects increase towards the slice located at $z = 5$ cm and decrease towards the upper and the lower ends of the phantom, located at $z = 10$ cm and $z = 0$ cm, respectively.
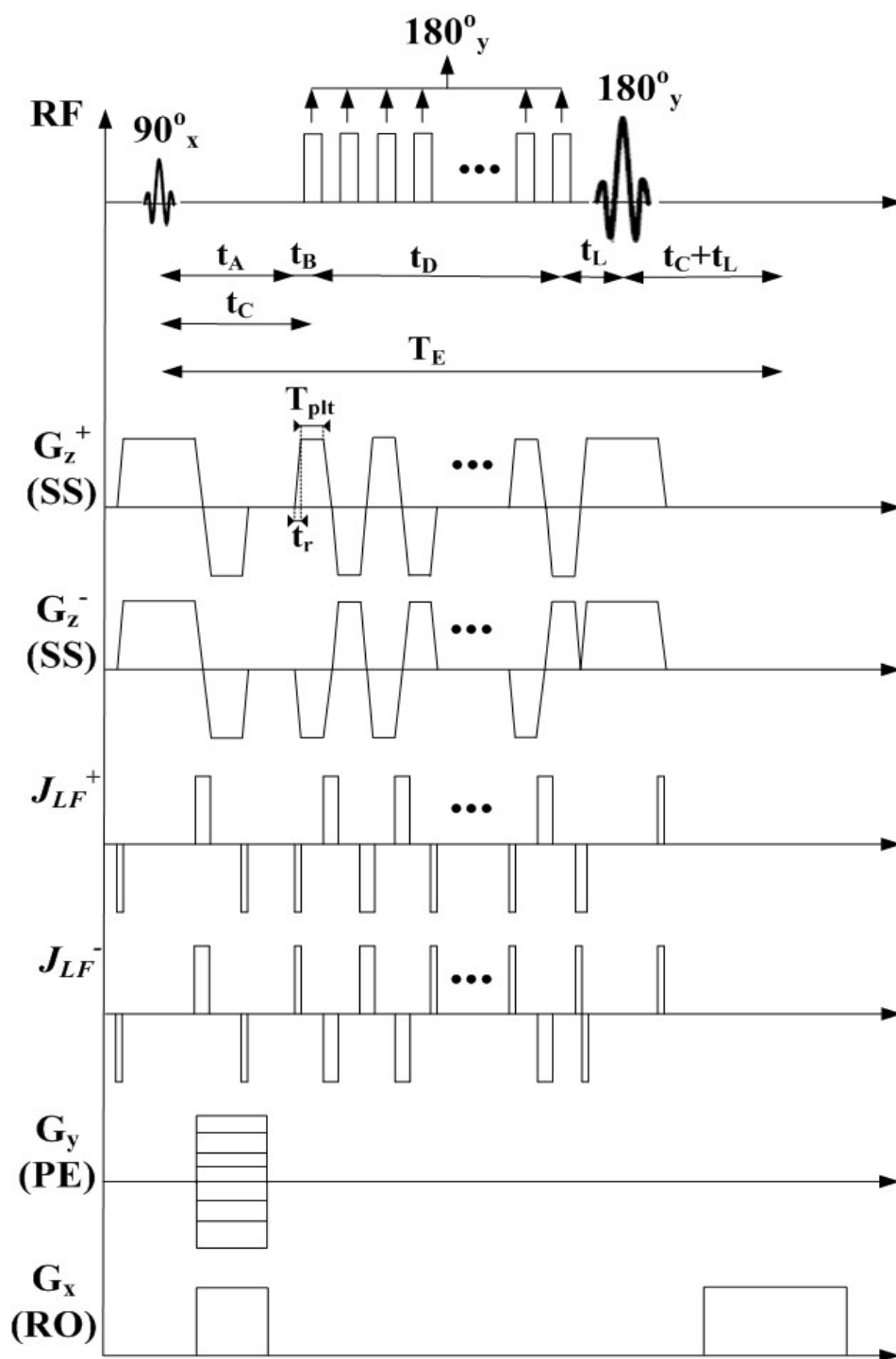
Figure 5.2 An MRI pulse sequence including a bipolar gradient waveform for the practical realization of ICMREIT [63].

| (a) | (b) |
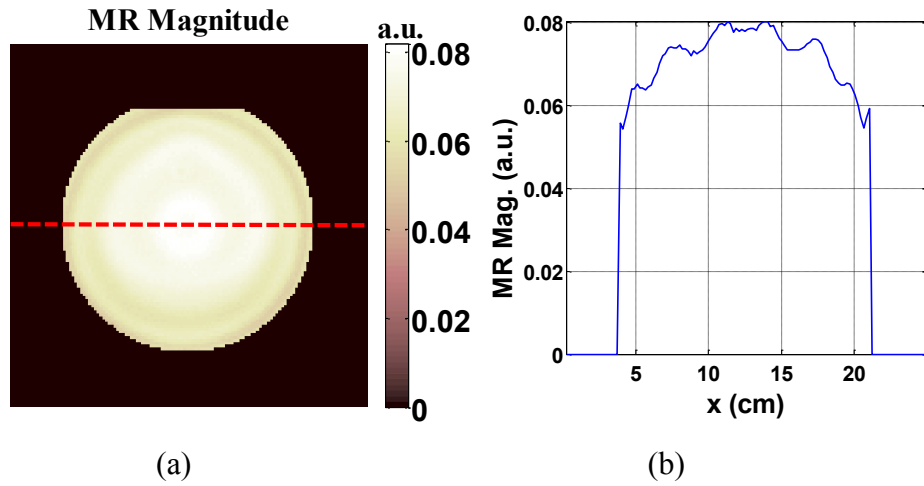
Figure 5.3 MR magnitude image (a) and profile (b) acquired for a uniform phantom of 0.49 S/m and the MRI pulse sequence with bipolar gradients. Geometric properties of the phantom are similar to Phantom 1a-b and the phantom is composed of 0.05 g $CuSO_4$ and 0.45g NaCl in 100 ml distilled water. Parameters of the MRI pulse sequence are similar to the parameters listed in Table 3.6. Image slice is close to the gradient iso-center.

In this study, the selected slice is located at $z = 9$ cm in order to minimize the cross-talk effects of the hard 180° RF pulses. In practical applications, different slices should be selected with the proposed MRI pulse sequence for ICMREIT. Therefore, the cross talk effects of the proposed MRI pulse sequence should be minimized by tailoring the RF pulses and using appropriate crusher gradients [92].

Increasing GS values of the proposed MRI pulse sequence is the remaining alternative for increasing the sensitivity of Φ_{LF} measurements. For the MRI pulse sequence used in physical experiments, GS is equal to the magnitude of the SS gradient and inversely related with ST. Therefore, an

111

increase in GS results in selection of thin slices which reduces the signal strength and SNR [65]. Further, the gradient waveform with increased GS values has more potential for neuro-muscular stimulation [92-93].

5.4 The Concept of RF Leakage

Mandija et al. [53] and Oran and İder [55] utilize conventional spin-echo MRI pulse sequence for the experimental realization of ICMREIT. In order to induce $\bar{J}_{LF}$ in a volume conductor, Oran and İder [55] use the SS gradient and Mandija et al. [53] locate an extra gradient on read-out axis, symmetrically around the 180° RF pulse of the conventional spin-echo MRI pulse sequence. Similar to our application, the MRI pulse sequences in [53, 55] are applied twice with positive and negative $\bar{J}_{LF}$ inducing gradient polarities and result in Φ^{+} and Φ^{-} distributions as expressed in (2.50-2.51). It is proposed to obtain Φ_{LF} by taking the difference of Φ^{+} and Φ^{-} as shown in (2.52). Mandija et al. describe the concept of geometrical shifts (Δx) in read-out direction for a spin-echo MRI pulse sequence and state that Δx is resulted from the imaging imperfections due to $\bar{J}_{LF-sys}$ and B_o inhomogeneities during read-out [53]. Since Φ^{+} and Φ^{-} are obtained with gradient waveforms with opposite polarities, the geometrical shifts in Φ^{+} and Φ^{-} are in opposite directions. Mandija et al. [53] express the shifted Φ^{+} and Φ^{-} distributions as

$$\Phi^{+}(x - \Delta x, y, z) = \Phi_{RF}(x - \Delta x, y, z) + \Phi_{LF}(x - \Delta x, y, z)$$
$$= \Phi_{RF}(r) - \Delta x \frac{\partial \Phi_{RF}(r)}{\partial x} + \Phi_{LF}(r) - \Delta x \frac{\partial \Phi_{LF}(r)}{\partial x} + O(x^2)$$

(5.7)

and

$$\Phi^-(x - \Delta x, y, z) = \Phi_{RF}(x + \Delta x, y, z) - \Phi_{LF}(x + \Delta x, y, z)$$
$$= \Phi_{RF}(r) - \Delta x \frac{\partial \Phi_{RF}(r)}{\partial x} + \Phi_{LF}(r) - \Delta x \frac{\partial \Phi_{LF}(r)}{\partial x} + O(x^2)$$

$$(5.8)$$

Using (5.7-5.8), it is proposed to calculate the shifted Φ_{RF} ($\Phi_{RF}{}^{shifted}$) and Φ_{LF} ($\Phi_{LF}{}^{shifted}$) distributions as

$$\Phi_{RF}{}^{shifted} = [\Phi^+(x - \Delta x, y, z) + \Phi^-(x + \Delta x, y, z)]/2 \qquad (5.9)$$
$$= \Phi_{RF}(r) + O(x^2)$$

and

$$\Phi_{LF}{}^{shifted} = [\Phi^+(x - \Delta x, y, z) - \Phi^-(x + \Delta x, y, z)]/2 \qquad (5.10)$$
$$= \Phi_{LF}(r) - \Delta x \frac{\partial \Phi_{RF}(r)}{\partial x} - \Delta x \frac{\partial \Phi_{LF}(r)}{\partial x} + O(x^2).$$

Mandija et al. [53] define RF leakage (Φ_{RF_leak}) as

$$\Phi_{RF\_leak} = \Delta x \frac{\partial \Phi_{RF}(r)}{\partial x} \qquad (5.11)$$

and model Φ_{RF} as

$$\Phi_{RF}(x) = ax^2 + bx + c. \qquad (5.12)$$

Substituting (5.12) in (5.11) results in

$$\Phi_{RF\_leak} = \Delta x(2ax + b). \qquad (5.13)$$

Mandija et al. apply artificial shifts (Δx) to the measured Φ^+ and Φ^-

distributions and calculate $\Phi_{RF}{}^{shifted}$ and $\Phi_{LF}{}^{shifted}$ distributions by using (5.9-5.10) [53]. As shown in Figure 1 of [53], $\Phi_{RF}{}^{shifted}$ and Φ_{RF} distributions are almost the same, which is consistent with (5.9). It is concluded that Φ_{RF} distributions are not affected from Δx. As shown in Figure 2,4-5 of [53], $\Phi_{LF}{}^{shifted}$ distributions have linear pattern in horizontal direction and scales linearly with Δx and conductivity, which is consistent with (5.10) and (5.13). In [53], it is concluded that Φ_{RF_leak} is much greater than Φ_{LF} and dominant in $\Phi_{LF}{}^{shifted}$ distributions. As shown in Figure 4-5 of [53], it is observed that Φ_{LF} distributions without artificial shifts do not scale with conductivity and do not have linear pattern in horizontal direction. The effect of Φ_{RF_leak} is not observed in true Φ_{LF} distributions without artificial shifts. In fact, Φ_{LF} profiles without artificial shifts show noisy characteristics. We think that the application of artificial shifts may generate Φ_{RF_leak} in $\Phi_{LF}{}^{shifted}$ distributions and Φ_{RF_leak} is not observable in true Φ_{LF} distributions.

The concept of Φ_{RF_leak} is investigated by using the experimental results obtained for the proposed MRI pulse sequence for ICMREIT and Phantom 2a. As shown in (5.11), Φ_{RF_leak} is related with $\frac{\partial \Phi_{RF}(r)}{\partial x}$. Using the measured Φ_{RF} and Φ_{LF} distributions, we compare the measured Φ_{LF} and the calculated $\frac{\partial \Phi_{RF}(r)}{\partial x}$ distributions. Acquired MR magnitude, Φ_{LF} and Φ_{RF} distributions with the corresponding horizontal profiles passing through the center of the inhomogeneities are shown in Figure 5.4. As shown in Figure 5.4, decreasing characteristics of Φ_{LF} and Φ_{RF} slopes inside the resistive inhomogeneity with respect to the background exhibit σ properties of the phantom.
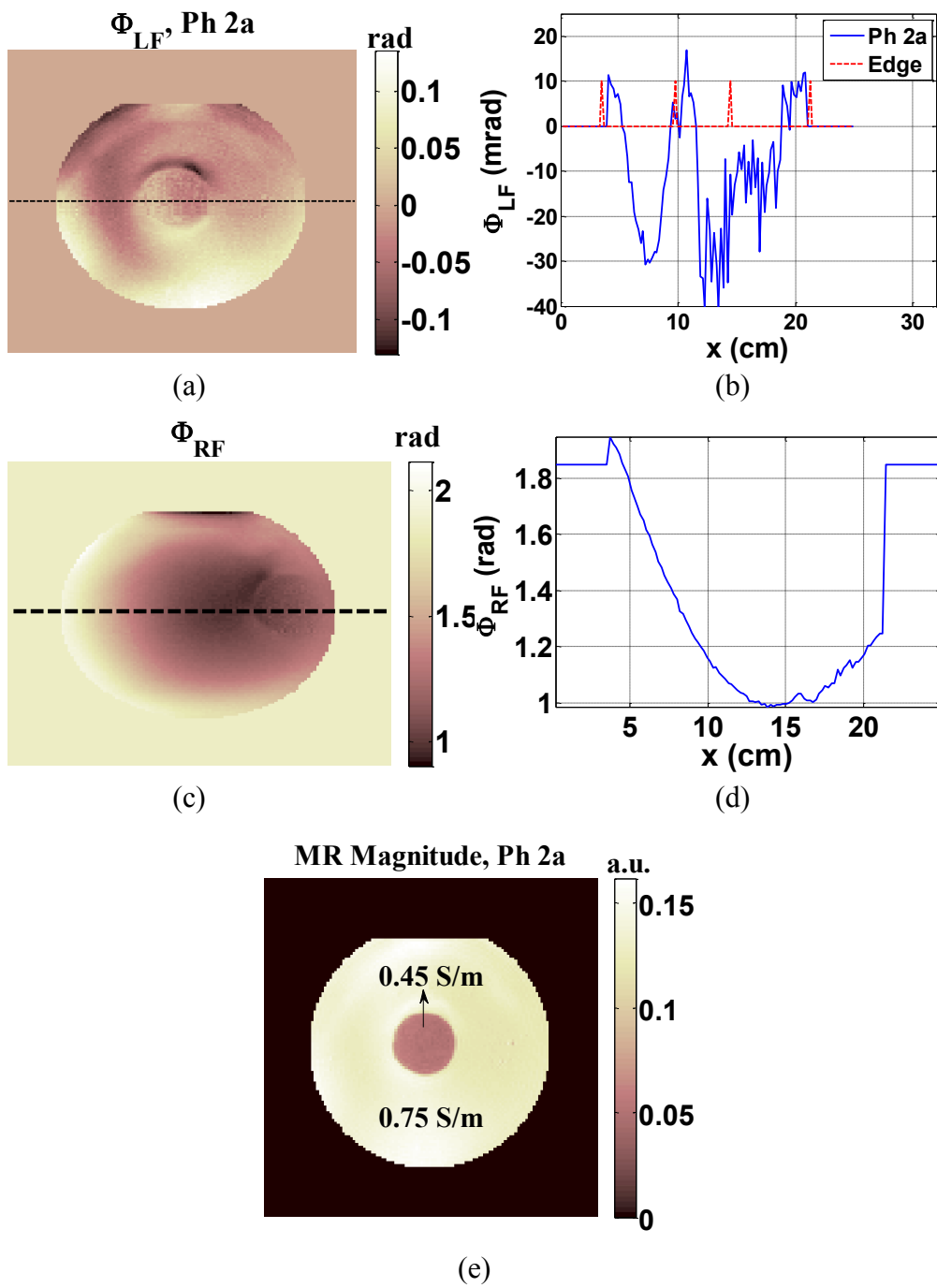
Figure 5.4 Φ_{LF} (a-b), Φ_{RF} (c-d), and MR magnitude distributions (e) of Phantom 2a.

In order to evaluate the dominance of Φ_{RF_leak} in measured Φ_{LF} distributions, the characteristics of $\partial\Phi_{RF}/\partial x$ are investigated. If Φ_{RF_leak} is dominant in measured Φ_{LF} images, measured Φ_{LF} and $\partial\Phi_{RF}/\partial x$ distributions should be similar. Spatial derivative operation amplifies the noise. Considering the model shown in (5.12), second order curve fitting is applied to the measured Φ_{RF} distributions. $\partial\Phi_{RF}(r)/\partial x$ distributions are calculated for true and smoothed Φ_{RF} distributions as shown in Figure 5.5.
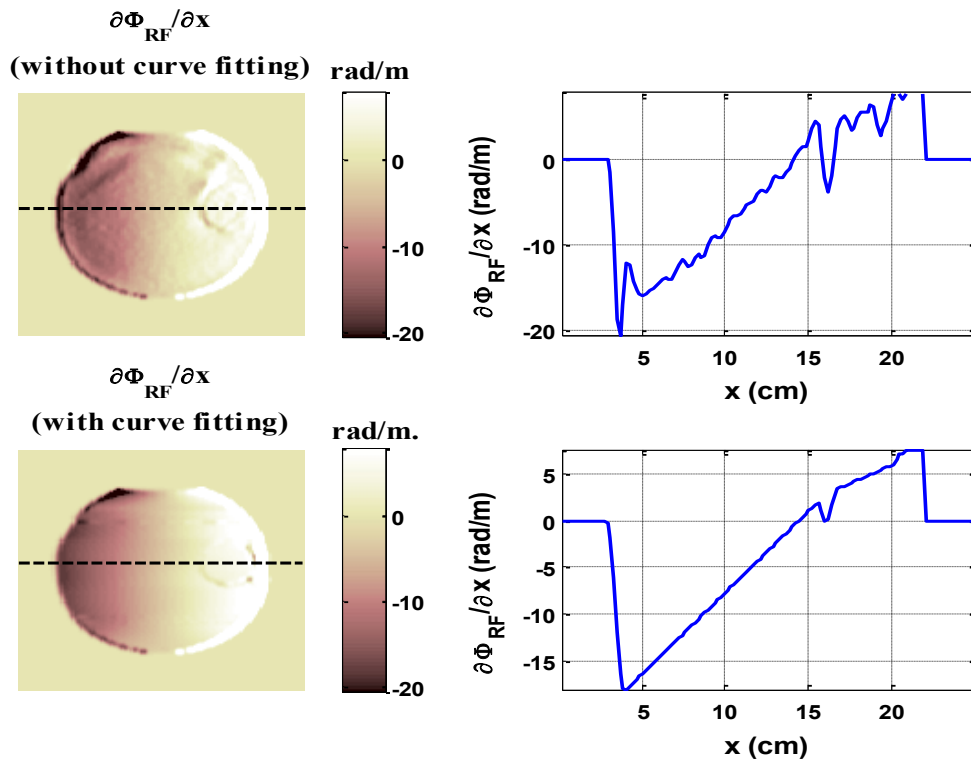
Figure 5.5 $\partial\Phi_{RF}/\partial x$ distributions with the corresponding horizontal profiles calculated by using true (without curve fitting) and smoothed (with second order curve fitting) Φ_{RF} distributions.

As shown in Figure 5.5, the slope of $\partial\Phi_{RF}(r)/\partial x$ profiles is positive over the selected slice. $\partial\Phi_{RF}(r)/\partial x$ profiles can be modelled with a first order

polynomial similar to the model given in (5.12-5.13). The slope of $\partial\Phi_{RF}/\partial x$ profiles is constant in the background of the phantom. Inside the inhomogeneity, the slope of $\partial\Phi_{RF}/\partial x$ profiles decreases due to the decreased conductivity of the inhomogeneity. Visibility of the inhomogeneity is increased in $\partial\Phi_{RF}(r)/\partial x$ distribution calculated with smoothed Φ_{RF} distribution due to the decrease of noise in Φ_{RF} distribution by means of curve fitting operation.

As shown in Figure 5.4-5.5, Φ_{LF} and $\partial\Phi_{RF}/\partial x$ distributions have different characteristics. As shown in Figure 5.5, Φ_{LF} profile has quadratic characteristics in the background and the inhomogeneity of Phantom 2a. Experimental results show that Φ_{RF_leak} may not be the source of measured Φ_{LF} distributions since the characteristics of Φ_{LF} and $\partial\Phi_{RF}/\partial x$ distributions are different.

In MR based electrical conductivity imaging, reconstructed σ images are related with the second order derivatives of measured phase distributions [44, 77, 80-83]. If Φ_{RF_leak} is dominant in Φ_{LF} images and contributes to the reconstructed σ images, then $\partial^2\Phi_{RF\_leak}/\partial x^2 = \Delta x\, \partial^3\Phi_{RF}/\partial x^3$ should give information about σ distributions. By using true Φ_{RF} distribution shown in Figure 5.4, $\partial^3\Phi_{RF}/\partial x^3$ distribution and the corresponding horizontal profiles are calculated as shown in Figure 5.6.

As shown in Figure 5.6, $\partial^3\Phi_{RF}/\partial x^3$ oscillates around zero which shows that $\nabla^2\Phi_{RF\_leak}$ does not represent the electrical conductivity properties of the phantom.

(a)   (b)
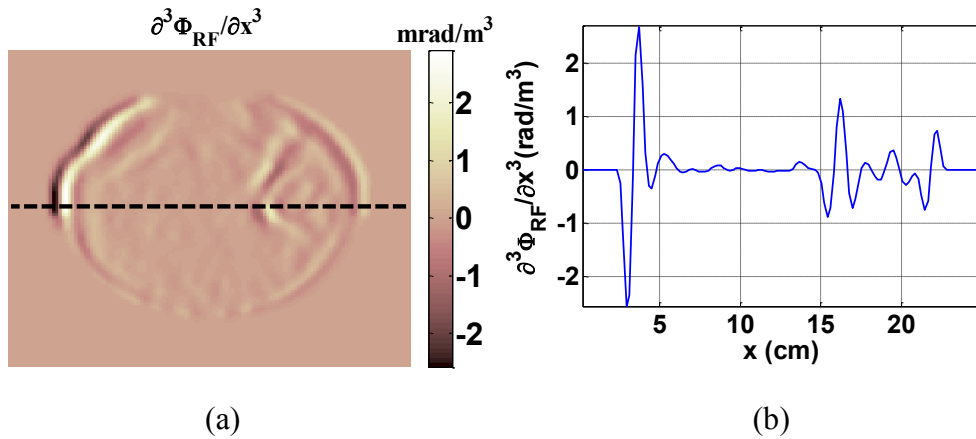
Figure 5.6 $\partial^3 \Phi_{RF}/\partial x^3$ distribution (a) and profile (b) for Phantom 2 (a).

5.5 Diffusion, Drift, and Magnetohydrodynamic Flow Effects

In this study, the characteristics of the MR phase distributions obtained as a result of the proposed MRI pulse sequence for ICMREIT are evaluated by using the electromagnetic phenomena in LF and RF regimes. As shown in Figure 2.2, the proposed MRI pulse sequence includes multiple SS gradient pulses with trapezoidal shape and symmetric with respect to the soft 180° RF pulses. If a phantom to be imaged includes moving molecules or ions, acquired MR signal can be attenuated and additional phase can be accumulated in MR images due to the non-zero gradient pulses on each side of the soft 180° RF pulses [94-95]. Phase contributions due to moving molecules or ions and $\bar{J}_{LF}$ induced by the time varying gradient waveform may be at the same order of magnitude.

Molecules and ions move due to diffusion, drift [96], or an external mechanical force [97]. Movement of molecules and ions due to a concentration gradient can be described as diffusion.

118

Diffusion can be expressed by using Fick's Law [96] as

$$\bar{j}_{diff} = -D_m \nabla C \,, \tag{5.14}$$

where $\bar{j}_{diff}$ is the diffusion flux, D_m and C are the diffusion coefficient and the concentration, respectively. For a uniform phantom filled with a saline solution, diffusion takes place in all directions which will result in negligible phase contribution of $\bar{j}_{diff}$ (Φ_{diff}). However, for the inhomogeneous phantoms filled with a saline solution in the background and including gel inhomogeneities, ∇C of water molecules are non-zero in regions close to the boundary of the inhomogeneities. Therefore, Φ_{diff} may contribute the measured Φ_{LF} images of inhomogeneous phantoms used in this study. The effect of Φ_{diff} on measured Φ_{LF} images may be evaluated with a more realistic approach by using biological tissue phantoms, such as chicken breast in which diffusion is restricted through the fibers [98].

Movement of ions due to an electrical potential gradient can be described as drift [96]. Ionic flux ($\bar{j}_{drift}$) due to drift forces [96] can be expressed as

$$\bar{j}_{drift} = -\mu_p \frac{z_p}{|z_p|} C_p \nabla V \,, \tag{5.15}$$

where the subscript p represents the pth ion, μ_p is the ionic mobility, z_p is the valance of the ion, C_p is the concentration of the ion, and V is the electrical potential field. In physical experiments, $\bar{J}_{LF}$ is due to $\bar{j}_{drift}$ inside the saline solutions. It is tried to measure the phase effects of B_{sz} distribution created by

$\bar{J}_{LF}$. Besides the B_{sz} effects of $\bar{j}_{drift}$, movement of ions due to $\bar{j}_{drift}$ may also contribute to measured Φ_{LF} images. However, the use of the proposed MRI pulse sequence for ICMREIT to evaluate the MR phase effects of drift of ions is very difficult. By injecting rectangular electrical current pulses to a uniform phantom filled with an ionic solution and using synchronized drift encoding gradient fields in x, y, or z directions with the injected current, MR phase effects of movement of ions due to drift forces can be evaluated. An MRI pulse sequence for imaging drift effects is proposed as shown in Figure 5.7.
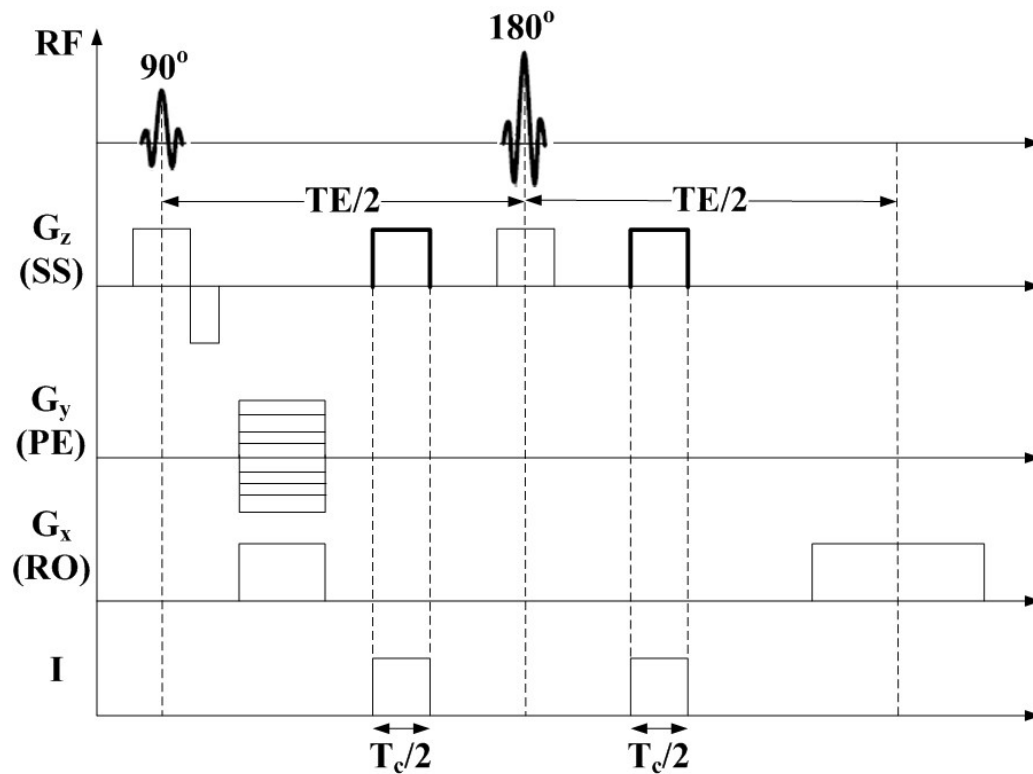
Figure 5.7 A spin-echo MRI pulse sequence with rectangular current (I) pulses and drift encoding gradients. Drift encoding gradients are in synchrony with I pulses, applied to SS gradient coil, and shown with a thicker line width.

The MRI pulse sequence shown in Figure 5.7 is similar to the spin-echo based MRI pulse sequences used in MRCDI and MREIT experiments [19-22, 26-27]. This pulse sequence should be applied to a uniform phantom filled with an ionic solution. Due to the homogenous nature of the uniform phantom, MR phase effects of diffusion will be negligibly small. Electrical current (I) is injected in synchrony with the MRI pulse sequence. The polarity and the magnitude of the current pulses applied before and after the 180° RF pulse are equal which results in cancellation of the MR phase effects of the magnetic flux density distributions, created by the injected current. The ions inside the phantom move due to the drift forces created by the injection current and the movement is encoded by the synchronized drift encoding gradient pulses, which are applied before and after the 180° RF pulse. By using these drift encoding gradients, drift related phase is accumulated in MR images. Drift encoding gradients can be applied in SS, PE or RO directions. The MRI pulse sequence shown in Figure 5.7 should be applied twice with and without electrical current pulses. By taking the difference of the resultant MR phase images obtained in two acquisitions, drift related phase can be obtained.

External mechanical forces applied or generated during an MRI pulse sequence results in movement of water molecules. Balasubramanian et al. inject electric current with 60 μA amplitude and 150 s duration to a phantom filled with an ionic solution during an EPI experiment [97]. They state that interaction of the ionic current ($\bar{J}$) with the magnetic flux density ($\bar{B}$) generates a Lorentz force distribution inside the ionic solution [97] as

$$\overline{F}_{em} = \bar{J} \times \bar{B} \,, \qquad\qquad (5.16)$$

where $\overline{F}_{em}$ represents the electromagnetic or Lorentz force. They express the movement of fluid molecules due to $\overline{F}_{em}$ by using the Navier-Stokes equation [97] as

$$\overline{F}_{em} = \rho_{fl} \frac{d\overline{u}}{dt}, \tag{5.17}$$

where ρ_{fl} and $\overline{u}$ are the fluid density and velocity, respectively. Balasubramanian et al. describe the flow of fluid molecules due to (5.17) as magnetohydrodynamic (MHD) flow. It is stated that MHD flow results in phase shifts in MR images without the utilization of specially designed velocity encoding gradients [95]. The usual imaging gradients of the MRI pulse sequences serve as the velocity encoding gradients [95].

During ICMREIT experiments, $\overline{J}_{LF}$ is induced in the phantoms filled with ionic solutions. Considering that B_o of the MRI scanner is the greatest component of $\overline{B}$ during an MRI experiment and substituting the semi-analytical solution for $\overline{J}_{LF}$ in (5.16) result in

$$\overline{F}_{em} = \left(-\frac{1}{2} j\omega \, r \, \sigma \, B_{pz} \, \overline{a}_\varphi\right) \times (B_o \overline{a}_z) = -\frac{1}{2} j\omega \, r \, \sigma \, B_{pz} B_o \overline{a}_r, \tag{5.18}$$

where $\overline{a}_r$ is the unit vector in radial direction. Considering (5.17-5.18), a single cycle of the proposed MRI pulse sequence for ICMREIT can be expressed as shown in Figure 5.8. As shown in Figure 5.8, $\overline{u}$ decrease to a minimum value with the negative $\overline{F}_{em}$ pulse, remains constant during T_{plt}, and increases through zero with the positive $\overline{F}_{em}$ pulse. It is observed that the average of $\overline{u}$ during a single gradient pulse is non-zero.

122
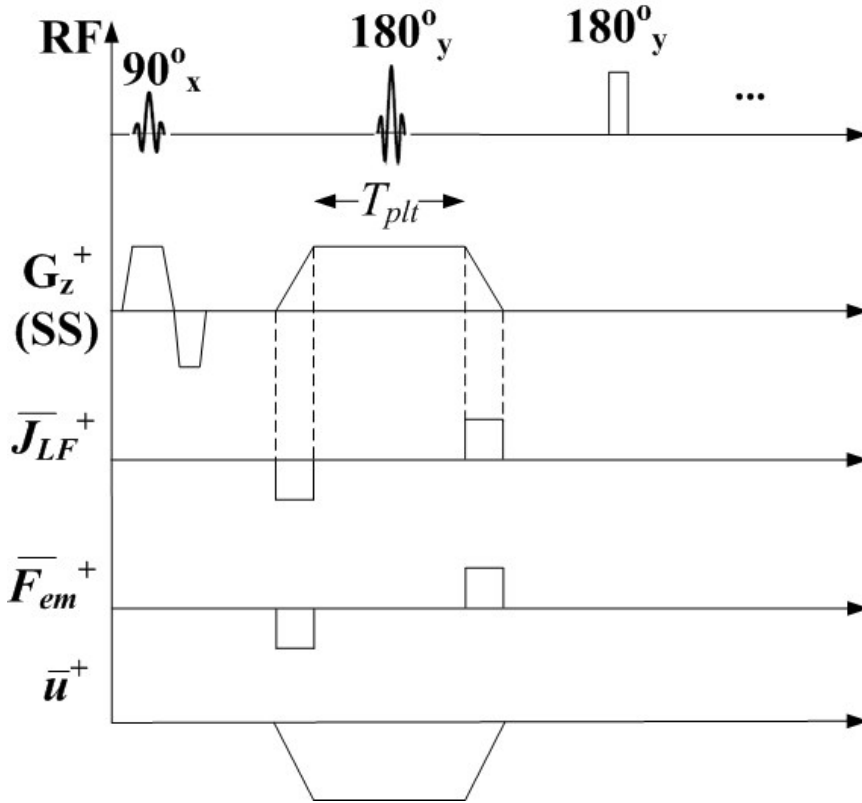
Figure 5.8 A single cycle of the proposed MRI pulse sequence for ICMREIT including $\overline{F}_{em}$ and $\overline{u}$ waveforms.

The non-zero SS gradients around the soft 180° RF pulse as shown in Figure 5.8 have potential to encode the MHD flow with a velocity of $\overline{u}$ and contribute to the measured Φ_{LF} distributions. This contribution can be represented as MHD phase (Φ_{MHD}). For the inhomogeneous phantoms used in physical experiments, σ and ρ_{fl} values of the background solutions and gel inhomogeneities are different. Therefore, Φ_{MHD} has potential to generate contrast in measured Φ_{LF} distributions which is related with σ and ρ_{fl} distributions.

CHAPTER 6

CONCLUSION AND FUTURE STUDY

In this thesis, ICMREIT is investigated starting from modeling and analysis to physical experiments. ICMREIT concept is realized by using the z-gradient coil of a clinical MRI scanner and simple experimental phantoms without utilizing external hardware. The proposed ICMREIT imaging technique provides a novel contrast based on LF electrical conductivity of the imaged media (tissues in medical imaging) in addition to conventional MR contrast such as spin, T_1, and T_2 weighted contrast. The major problem of the ICMREIT implementation presented in this study is the low sensitivity of Φ_{LF} measurements. Investigation of the concepts related with diffusion, drift and MHD forces shows that flow effects may contribute to the measured Φ_{LF} distributions since the sensitivity of the method is very small. Sensitivity of ICMREIT can be increased by using a gradient waveform with, greater GS and N_{cycle} values or bipolar gradient pulses. However, the application of such sensitivity increasing methods is not straightforward due to the concerns related with neuro-muscular stimulation, SAR values, and imaging artifacts. The reconstructed $|\bar{J}_{LF}|$ and σ_{rec} images with simulated and experimental measurements exhibit the electrical conductivity properties of the phantoms.

Neglected B_{sx} and B_{sy} distributions during the reconstruction of J_x and J_y distributions and insufficiency of the curve fitting method in small regions located between the boundary of the eccentric inhomogeneities and the phantoms increase reconstruction errors. Curve fitting based smoothing filter reduce the spatial resolution. Neglected $\partial\sigma/\partial x$ and $\partial\sigma/\partial y$ terms during the derivation of the J-derivative algorithm result in boundary artifacts in σ_{rec} images and these artifacts are carried over the horizontal and the vertical profiles passing through the inhomogeneities. Due to the error sources related with physical measurements and image reconstruction, σ_{rec} images are rough estimates of the simple phantoms and they exhibit qualitative reconstructions rather than quantitative images [65]. ICMREIT can be considered as a safe imaging method since $\left|\overline{E}\right|_{max}$ values calculated from simulation and experimental results are smaller than the electric field limit at 1 kHz [43, 65, 78].

Future studies should focus on providing σ_{rec} images with better quality and resolution. To achieve this, the quality of physical measurements and success of the image reconstruction process should be increased. To increase the quality of the physical measurements, the proposed MRI pulse sequence should be optimized. To increase the sensitivity of the physical measurements, the use of bipolar gradient waveforms with hard 180° RF pulses should be investigated. In order to increase the reconstruction performance of the method, J_x and J_y distributions should be reconstructed with better accuracy. The smoothing filter in image reconstruction process should be eliminated in order to increase the spatial resolution of σ_{rec} images. $\overline{B}$ based image reconstruction algorithms, such as MREIT sensitivity algorithm [25], can be utilized for reconstructing σ_{rec} images. The effects of diffusion, drift, and MHD forces on

measured Φ_{LF} distributions can be investigated by using numerical simulations and physical experiments.

REFERENCES

[1] L. Geddes and L.E. Baker, "The specific resistance of biological materials: A compendium of data for the biomedical engineer and physiologis*t*," *J. Med. Biol. Eng.*, vol. 5, no. 3, pp. 271-293, 1967.

[2] C. Gabriel, S. Gabriel, and E. Corthout, "The dielectric properties of biological tissues: I. Literature survey," *Phys. Med. Biol.,* vol. 41, pp. 2231–2249, 1996.

[3] S. Gabriel, R.W. Lau and C. Gabriel, "The dielectric properties of biological tissues: II. Measurements in the frequency range 10 Hz to 20 GHz," *Phys. Med. Biol.,* vol. 41, pp. 2231–2249, 1996.

[4] W. Kuang and S.O. Nelson, "Low-frequency dielectric properties of biological tissues: A review with some new insights," *Trans Am. Soc. Agric. Eng.*, vol. 41, no. 1, pp. 173-184,1998.

[5] D.C. Barber and B.H. Brown, "Imaging spatial distributions of resistivity using applied potential tomography," *Electron. Lett. E: Sci. Instrum., vol.* 19, no. 22, pp. 933-935, 1983.

[6] D.C. Barber and B.H. Brown, "Applied potential tomography," *J. Phys.*

E: Sci. Instrum.,vol. 17, no. 9, pp. 723-733, 1984.

[7]   L. Borcea, "Applied potential tomography," *Inv. Prob., vol.* 18, pp. R99-136, 2002.

[8]   W. Lionheart, N. Polydorides, and A. Borsic, "The reconstruction problem" in *Electrical impedance tomography, Methods, History and Applications,* IOP Publishing, D. Holder Ed., 2005, pp. 3-64.

[9]   G.J. Saulnier, "EIT instrumentation," in *Electrical impedance tomography, Methods, History and Applications,* IOP Publishing, D. Holder Ed., 2005, pp. 84-182.

[10] B.M. Eyüboğlu., "Electrical impedance imaging: injected current electrical impedance imaging," in *Wiley-Encyc. Biomed. Eng*., vol. 2, M. Akay Ed., 2006 pp.1195-1205.

[11] D.C. Barber, "Electrical Impedance Tomography," in *The Biomedical Engineering Handbook Second Edition,* 3rd ed., J.D. Bronzino, Ed. CRC Press, Boca Raton, 2006, pp. 17_1-17_14.

[12] G. Hahn et al., "Imaging pathologic pulmonary air and fluid accumulation by functional and absolute EIT," *Physiol. Meas*., vol.27, no.5, pp. 187-198, 2006.

[13] E. Teschner and M. Imhoff, *Electrical impedance tomography: The realization of regional ventilation monitoring*, Dräger Medical GmbH, Lübeck, 2010.

[14] T-J. Kao et al., "Real-Time 3D electrical impedance imaging for ventilation and perfusion of the lung in lateral decubitus position," in *Proc. IEEE Int. Conf. Eng. in Med. and Biol. (EMBC 2014)*, Chicago, 2014, pp. 1135-1138.

[15] B. Amm et al., "Real-Time 3D electrical impedance imaging for ventilation monitoring of the lung: pilot study," in *Proc. IEEE Int. Conf. Eng. in Med. and Biol. (EMBC 2014)*, Chicago, 2014, pp. 6064-606.

[16] W.R. Purvis, R.C. Tozer, and I.L. Freeston, "Impedance imaging using induced currents," in *Proc. IEEE Int. Conf. Eng. Med. Biol. Soc.*, 1990, pp. 198-201.

[17] N.G. Gençer, M. Kuzuoğlu, and Y.Z. İder, "Electrical impedance tomography using induced currents," *IEEE Trans. Med. Imag.*, vol. 13, no. 2, pp. 338-350, 1994.

[18] N.G. Gençer, "Electrical Impedance Tomography Induced Current," in *Wiley-Encyc. Biomed. Eng.*, M. Akay, Ed., 2006.

[19] G.C. Scott et al., "Measurement of nonuniform current density by magnetic resonance," *IEEE Trans. Med. Imag.*, vol. 10, no. 3, pp. 362-374, 1991.

[20] G.C. Scott et al., "Sensitivity of Magnetic-Resonance Current-Density Imaging," *J. Magn. Reson.*, vol. 97, no. 3, pp. 235-254, 1992.

[21] I. Sersa et al., "Electric current density imaging of mice tumors," *Magn.*

Reson. Med., vol. 37, no. 4, pp. 404-409, 1997.

[22] B.M. Eyüboğlu, R. Reddy, and J.S. Leigh, "Imaging electrical current density using nuclear magnetic resonance," *Elektrik, Turkish J. Elect. Eng. Comp. Sci.,* vol. 6, no. 3, pp. 201–214, 1998.

[23] U. Mikac, F. Demsar, K. Beravs and I. Sersa, "Magnetic resonance imaging of alternating electric currents," *Magn. Reson. Imag.*, vol. 19, pp. 845-856, 2001.

[24] N. Zhang, "Electrical impedance tomography based on current density imaging," MSc. thesis, University of Toronto, Toronto, 1992.

[25] Y.Z. İder and Ö. Birgül, "Use of magnetic field generated by the internal distribution of injected currents for electrical impedance tomography (MR-EIT)," *Elektrik, Turkish J. Elect. Eng. Comp. Sci.,* vol. 6, no. 3, pp. 215–225, 1998.

[26] B.M. Eyüboğlu, R. Reddy, and J.S. Leigh, "Magnetic resonance-electrical impedance tomography," Prov. Patent U.S. 60/122,310, March 1, 1999.

[27] B.M. Eyüboğlu, R. Reddy, and J.S. Leigh, "Magnetic resonance-electrical impedance tomography," US Patent 6,397,095 B1 May 28, 2002.

[28] Ö. Birgül, B.M. Eyüboğlu, and Y.Z. İder, "Experimental results for 2D magnetic resonance electrical impedance tomography (MR-EIT) using magnetic flux density in one direction" *Phys. Med. Biol.,* vol. 48, no. 21, pp. 3485–3504, 2003.

[29] Ö. Birgül, B.M. Eyüboğlu, and Y.Z. İder, "Current constrained voltage scaled reconstruction (CCVSR) algorithm for MR-EIT and its performance with different probing current patterns," *Phys. Med. Biol.,* vol. 48, no. 5, pp. 653-671, 2003.

[30] L.T. Müftüler et al., "Resolution and contrast in magnetic resonance electrical impedance tomography (MREIT) and its application to cancer imaging," *Tech. Canc. Res. Treat,* vol. 3, no.6, pp. 599-609, 2004.

[31] E.J. Woo, J.K. Seo, and S. Lee, "Magnetic resonance electrical impedance tomography (MREIT)," in *Electrical impedance tomography, Methods, History and Applications,* IOP Publishing, D. Holder Ed., 2005, pp. 254-309.

[32] B.M. Eyüboğlu, "Magnetic resonance electrical impedance tomography," in *Wiley-Encyc. Biomed. Eng.*, vol. 4, M. Akay, Ed., 2006, pp. 2154-2162.

[33] S.H. Oh et al., "Electrical conductivity images of biological tissue phantoms in MREIT," *Physiol. Meas.,* vol. 26, pp. S279–S288, 2005.

[34] E.K Woo and J.K. Seo, "Magnetic resonance electrical impedance tomography (MREIT) for high-resolution conductivity imaging," *Physiol. Meas.,* vol. 29, pp. R1–R26, 2008.

[35] H.J. Kim et al., "In vivo electrical conductivity imaging of a canine brain using a 3 T MREIT system," *Physiol. Meas.,* vol. 29, pp. 1145-1155, 2008.

[36] H.J. Kim et al., "In vivo high-resolution conductivity imaging of the human leg using MREIT: the first human experiment," *IEEE Trans. Med. Imag.*, vol. 28, no. 11, pp. 1681-1687, 2009.

[37] K. Jeon et al., "MREIT conductivity imaging of the postmortem canine abdomen using CoReHA," *Physiol. Meas.,* vol. 30, pp. 957-966, 2009.

[38] K. Jeon et al., "Integration of the denoising, inpainting and local harmonic B_z algorithm for MREIT imaging of intact animals," *Phys. Med. Biol.,* vol. 55, pp. 7541-7556, 2010.

[39] A.S. Minhas et al., "Experimental performance evaluation of multi-echo ICNE pulse sequence in magnetic resonance electrical impedance tomography," *Magn. Reson. Med.*, vol. 66, no. 4, pp.957-965, 2011.

[40] V.E. Arpınar et al., "MREIT experiments with 200 μA injected currents: a feasibility study using two reconstruction algorithms, SMM and harmonic B_z," *Phys. Med. Biol.,* vol. 57, pp. 4245-4261, 2012.

[41] E. Değirmenci and B.M. Eyüboğlu, "Image reconstruction in magnetic resonance conductivity tensor imaging (MRCTI)" *IEEE Trans. Med. Imag.*, vol. 31, no.3 pp. 525-532, 2012.

[42] E. Değirmenci and B.M. Eyüboğlu, "Practical realization of magnetic resonance conductivity tensor imaging (MRCTI)" *IEEE Trans. Med. Imag.*, vol. 32, no. 3, pp. 601-608, 2013.

[43] Medical electrical equipment - part 2-33: Particular requirements for the basic safety and essential performance of magnetic resonance equipment for medical diagnosis, IEC 60601-2-33:2010, 2010.

[44] L. Özparlak and Y.Z. İder, "Induced current magnetic resonance electrical impedance tomography," *Physiol. Meas.*, vol. 26, no. 2, pp. 289-305, 2005.

[45] Y. Liu, S. Zhu, and B. He, "Induced current magnetic resonance electrical impedance tomography of brain tissues based on J-substitution algorithm: a simulation study," *Phys. Med. Biol.*, vol. 54, no. 14, pp. 4561-4573, 2009.

[46] M.E. Özsüt, "Design and implementation of Labview based data acquisition and image reconstruction environment for METU-MRI system," MSc. thesis, Middle East Technical University, Ankara, Turkey, 2005.

[47] A.L.H.M.W. van Lier, C.A.T. van den Berg, and U. Katscher, "Measuring electrical conductivity at low frequency using the eddy currents induced by the imaging gradients," in 20th *Proc. Intl. Soc. Mag. Reson. Med. (ISMRM)*, 2012, p. 3467.

[48] Ö.F. Oran et al., "Convection-reaction equation based low-frequency conductivity imaging using readout gradient induced eddy currents," in *Proc. 21th Intl. Soc. Mag. Reson. Med. (ISMRM)*, 2013, p. 4188.

[49] N. de Geeter, G. Crevecoeur, and L. Dupré, "A numerical study on conductivity estimation of the human head in the low frequency domain using induced current MR phase imaging EIT with multiple gradients," *IEEE Trans. Magn.*, vol. 49, no. 9, pp. 5004-5010, 2013.

[50] H.H. Eroğlu and B.M. Eyüboğlu, "Induced current magnetic resonance electrical impedance tomography with z-gradient coils," in *Proc. IEEE Int. Conf. Eng. in Med. and Biol. (EMBC 2014)*, Chicago, 2014, pp. 1143-1146.

[51] H.H. Eroğlu and B.M. Eyüboğlu, "Two alternatives for magnetic resonance electrical impedance tomography: injected or induced current," *Physiol. Meas.*, vol. 37, no. 11, pp. 2024-2049, 2016.

[52] D. Isaacson, "Distinguishability of conductivities by electric current computed tomography," *IEEE Trans. Med. Imag.*, vol. mi-5, no. 2, pp. 91-95, 1986.

[53] S. Mandija et al., "A geometrical shift results in erroneous appereance of low frequency tissue eddy current induced phase maps," *Magn. Reson. Med.,* vol.76, no.3, pp. 905-912, 2016.

[54] E. Gibbs and C. Liu, "Feasibility of imaging tissue electrical conductivity by switching field gradients with MRI," *Tomogr.*, vol. 1, no. 2, pp. 125-135, 2015.

[55] Ö.F. Oran and Y.Z. İder, "Feasibility of conductivity imaging using subject eddy currents induced by switching of MRI gradients," *Magn.*

Reson. Med., vol. 77, no. 5, pp. 1926-1937, 2017.

[56] W. Frei (2013) Computational Electromagnetics Modeling, Which Module to Use? COMSOL A.B. [Online]. Available: https://www.comsol.com/blogs/computational-electromagnetics-modeling-which-module-to-use/

[57] W. Frei (2016) How to Choose Between Boundary Conditions for Coil Modelling. COMSOL A.B. [Online]. Available: https://www.comsol.com/blogs/how-to-choose-between-boundary-conditions-for-coil-modeling/

[58] P. Bettess "Infinite elements" *Int. J. Numer. Meth. Eng.* vol. 11, no. 3, pp. 53–64, 1977.

[59] O.C. Zienkiewicz, C. Emson, and P. Bettess, "A novel boundary infinite element," *Int. J. Numer. Meth. Eng.,* vol. 19, no. 3, pp.393–404, 1983.

[60] O.F. Gandhi, J.F. DeFord, and H. Kanai, "Impedance method for calculation of power deposition patterns in magnetically induced hyperthermia," *IEEE Trans. Magn.,* vol. BME-31, no. 10, pp. 644-651, 1984.

[61] D.P. Fernandez et al., "A database for static dielectric constant of water and steam," *J.Phys.Chem.Ref.Data*, vol. 24, no. 1, pp. 33-69, 1995.

[62] M.N.O. Sadiku, *Numerical Techniques in Electromagnetics with Matlab,* 2nd ed., CRC Press, Boca Raton, 2001, pp.134-222.

[63] B.M. Eyüboğlu, H.H. Eroğlu, M. Sadighi, et al., "Induced Current Magnetic Resonance Electrical Impedance Tomography (ICMREIT) Pulse Sequence Based on Bipolar Gradient Pulses," Turkish Patent Institute pending patent No. P16/0494.

[64] B.M. Eyüboğlu, H.H. Eroğlu, and M. Sadighi, "Tek Kutuplu Kesit Seçici Gradyan Darbe Tabanlı Akım İndüklemeli Manyetik Rezonans Elektriksel Empedans Tomografisi (AİMREET) Darbe Dizini," Turkish Patent Institute pending patent No. P17/0601.

[65] H.H. Eroğlu et al., "Induced current magnetic resonance electrical conductivity imaging by low frequency switching of gradient coils," submitted to *IEEE Trans. Med. Imag.* unpublished.

[66] J.M.C. Tas, "Modelling and analyzing the z-gradient coil in an MRI scanner," MSc. thesis, Dept. Math. Comp. Sci., Technische Universiteit Eindhoven, Eindhoven, the Netherlands, 2005.

[67] R. Maini and H. Aggarwal, "Study and Comparison of various image edge detection techniques," *Int. J. Imag. Proc. (IJIP)*, vol. 3, no. 1, pp. 1-11, 2009.

[68] R. Boyacıoğlu, "Performance evaluation of current density based magnetic resonance electrical impedance tomography reconstruction algorithms," MSc. thesis, Middle East Technical University, Ankara, Turkey, 2009.

[69] D. Isaacson, "Process and apparatus for distinguishing conductivities by electric current computed tomography," US4920490 A Apr 24, 1990.

[70] A.D. Seagar, D.C. Barber, and B.H. Brown, "Theoretical limits to sensitivity and resolution in impedance imaging," *Clin. Phys. Physiol. Meas.*, vol. 8, no. 13, pp. 13-31, 1987.

[71] B.M. Eyüboğlu, A. Köksal, and M. Demirbilek, "Distinguishability analysis of induced current EIT system using discrete coils," *Phys. Med. Biol.*, vol. 45, no. 7, pp. 1997-2009, 2000.

[72] A. Köksal, B.M. Eyüboğlu, and M. Demirbilek, "A quasi-static analysis for a class of induced current EIT system using discrete coils," *IEEE Trans. Med. Imag.*, vol. 21, no. 6, pp. 688-694, June 2002.

[73] H. Altunel, B.M. Eyüboğlu, and A. Köksal, "Distinguishability for magnetic resonance electrical impedance tomography (MR-EIT)," *Phys. Med. Biol.*, vol. 52, no. 2, pp. 375-387, 2007.

[74] R.J. Sadleir et al., "Noise analysis in magnetic resonance electrical impedance tomography at 3 and 11 T field strengths," *Physiol. Meas.*, vol. 26, pp. 875-884, 2005.

[75] H.H. Eroğlu, M. Sadighi, K. Sümser et al., "Experimental realization of induced current magnetic resonance current density imaging," in *Proc. IEEE Int. Conf. Eng. in Med. and Biol. Soc. (EMBC 2015),* Milano, 2015, pp. 614-617.

[76] H.H. Eroğlu and B.M. Eyüboğlu, "Sensitivity based image reconstruction for ICMREIT," in *Proc. Int. Symp. on Biomed. Imag.* (ISBI), Beijing, 2014.

[77] B.I. Lee, S.H. Oh, E.J. Woo et al., "Static resistivity image of a cubic saline phantom in magnetic resonance electrical impedance tomography (MREIT)," *Physiol. Meas.*, vol. 24, pp. 579-589, 2003.

[78] A. Borsic and K.D. Paulsen, "Safety study for induced current magnetic resonance-electrical impedance tomography in breast imaging," in *Proc. 10th Int. Conf. on Biomed. App. of Elect. Imp. Tomog.*, Manchester, 2009, pp. 1-2.

[79] T.W. Nixon, S. McIntyre, D.L. Rothman, and R.A. de Graaf, "Compensation of gradient-induced magnetic field perturbations," *J. Magn. Reson.*, vol. 192, no. 2, pp. 209-217, 2008.

[80] E.M. Haacke, L.S. Petropoulos, E.W. Nilges et al., "Extraction of conductivity and permittivity using magnetic resonance imaging," *Phys. Med. Biol.*, vol.36, pp.723–733, 1991.

[81] U. Katscher, T. Voigt, C. Findeklee et al., "Determination of electrical conductivity and local SAR via B1 mapping," *IEEE Trans. Med. Imag.*, vol. 28, no.9, pp. 1365–1374, 2009.

[82] S.B. Bulumulla, S.K.B. Lee, and T.B. Yeo, "Conductivity and permittivity

imaging at 3.0 T," *Conc. in Magn. Reson. Part B (Magn. Reson. Eng.)*, vol.41B (1), pp.13–21, 2012.

[83] A.L.H.M.W. van Lier, D.O. Brunner, K.P. Pruessmann et al., "B1+ phase mapping at 7T and its application for in vivo electrical conductivity mapping," *Magn. Reson. in Med.* vol.67, pp. 552–561, 2012.

[84] P. Mansfield, "Multi-planar image formation using NMR spin echoes," *J. Phys. C: Solid State Phys.*, vol. 10, pp. L55-L58, 1977.

[85] M.P-Amin, S.A. Mirowitz, J.J. Brown et al., "Principles and Applications of Echo-planar Imaging: A Review for the General Radiologist[1]," *Radiograph.*, vol. 21, no. 3, pp. 767-779, 2001.

[86] P. Mansfield and B. Chapman, "Active magnetic screening of coils for static and time-dependent magnetic field generation in NMR imaging," *J. Phys. E: Sci. Instrum.*, vol. 19, pp.540-545, 1986.

[87] H. Sugimoto, "Magnetic resonance imaging system including active shield gradient coils.," European Patent 0 433 002 A2 Jun 19, 1991.

[88] A.J. Wheaton and W.R. Dannels, "Mapping eddy current fields in MRI system," US Patent 2014/0232393 A1 Aug 2014.

[89] R.S. Hinks, "Measurement and calibration of eddy currents for magnetic resonance imagers," US Patent 4,978,919 Dec 1990.

[90] C. Ma, and X.H. Jiang, "A new eddy current compensation method in MRI," *PIERS online,* vol. 3, no. 6, pp. 874-878, 2007.

[91] Y. Zhou and K.F. King, "Eddy current measurement and correction in magnetic resonance imaging systems with a static phantom," US 7,112,964 B2 Sep 26, 2006.

[92] M.A. Bernstein, K.F. King, and X.J. Zhou, *Handbook of MRI Pulse Sequences*, Elsevier Academic Press, 2004, p.216.

[93] M. Brand and O. Heid, "Induction of electric fields due to gradient switching:a numerical approach," *Magn. Reson. in Med.* vol.48, pp. 731–734, 2002.

[94] E.O. Stejskal and J.E. Tanner, "Spin diffusion measurements: spin echoes in the presence of a time-dependent field gradient," *J. Chem. Phys.* vol.42, no.1, pp. 288–292, 1965.

[95] D. J. Bryant, I. A. Payne, D. N. Firmin et al., "Measurement of flow with NMR imaging using a gradient pulse and phase difference technique," *J. Comp. Assist. Tomogr.* vol.8, no.4, pp. 588–593, 1984.

[96] R. Plonsey and R.C Barr, "Bioelectric Potentials," in *Bioelectricity A Quantitative Approach,* 3rd ed., Springer Science+Business Media, LLC, New York, 2007, pp. 45-69.

[97] M. Balasubramanian, R.V. Mulkern, W.M. Wells et al., "Magnetic resonance imaging of ionic currents in solution: the effect of magnetohydrodynamic flow," *Magn. Reson. Med.,* vol.74, pp. 1145–1155, 2015.

[98] O.I. Kwon, W.C. Jeong, S.Z.K. Sajib et al., "Anisotropic conductivity tensor imaging in MREIT using directional diffusion rate of water molecules," *Phys. Med. Biol.,* vol.59, pp. 2955–2974, 2014.

CURRICULUM VITAE

PERSONAL INFORMATION

Surname, Name: Eroğlu, Hasan Hüseyin

Nationality: Turkish (TC)

Date and Place of Birth: 23 August 1985, Sandıklı/Afyonkarahisar

Marital Status: Married

Phone: +90 505 4018814

Fax: +90 312 291 2199

email: eroglu.hasan@metu.edu.tr

EDUCATION

Degree	Institution	Year of Graduation
MSc.	METU Electrical and Electronics Engineering	2010
BSc.	METU Electrical and Electronics Engineering	2007
High School	Maltepe Military High School	2003

WORK EXPERIENCE

Year	Place	Enrollment
2016-present	Gaziler Physical Therapy and Rehabilitation Education and Research Hospital	Chief of Clinical Engineering Unit
2009-2016	TAF Rehabilitation and Care Center	Chief of Medical Device Repair and Maintenance Division
2007-2009	Gülhane Medical Military Academy	Chief of Medical Device Calibration Division
2007-2008	Turkish Military Academy, Faculty and Collage Company	Class Officer

FOREIGN LANGUAGES

Advanced English

PUBLICATIONS

Journal Articles

[1]   H.H. Eroğlu, M. Sadighi, and B.M. Eyüboğlu,, "Induced current magnetic resonance electrical conductivity imaging with oscillating gradients," *submitted to IEEE Trans Med. Imag.,* Submitted for publication.

[2]   H.H. Eroğlu and B.M. Eyüboğlu, "Two alternatives for magnetic resonance electrical impedance tomography: injected or induced current," *Physiol. Meas.*, vol. 37, no. 11, pp. 2024-2049, 2016.

[3]   H.H. Eroğlu and A.M. Hava, "Control, design, and implementation of a low cost ultracapacitor test system" *Turkish J. Elect. Eng. Comp. Sci.,* vol.21, no.3, pp. 630-648, 2013.

National Magazines

[1]   H.H. Eroğlu and A.M. Hava, "Enerji depolama uygulamalarında ultrakondansatörlerin yeri ve kullanımı" *Otomasyon Dergisi*, 225, pp. 306-312, March 2011.

Conference Papers

[1]   K. Sümser, N. Naji, M. Sadighi, H.H. Eroğlu, and B.M. Eyüboğlu, "MRI-SPAMM based magnetic resonance electrical impedance tomography," *in Proc. Intl. Soc. Mag. Reson. Med. (ISMRM)*, 24, 2016, p.1940.

[2]   N. Naji, H.H. Eroğlu, K. Sümser, M. Sadighi, B.M. Eyüboğlu, "Enhancing induced current magnetic resonance electrical impedance tomography (ICMREIT) image reconstruction," *in Proc. 12th IASTED Int. Conf. Biomed. Eng. (BIOMED)*, Insbruck, 2016, pp. 832-834.

[3]   H.H. Eroğlu, M. Sadighi, K. Sümser et al., "Experimental realization of induced current magnetic resonance current density imaging," in *Proc. IEEE Int. Conf. Eng. in Med. and Biol. Soc. (EMBC 2015),* Milano, 2015, pp. 614-617.

[4]   H.H. Eroğlu and B.M. Eyüboğlu, "Induced current magnetic resonance electrical impedance tomography with z-gradient coils," in *Proc. IEEE Int. Conf. Eng. in Med. and Biol. (EMBC 2014)*, Chicago, 2014, pp. 1143-1146.

[5]   C. Göksu, M. Sadighi, H.H. Eroğlu, and B.M. Eyüboğlu, "Realization of magnetic resonance current density imaging at 3 Tesla," in *Proc. IEEE Int. Conf. Eng. in Med. and Biol. (EMBC 2014)*, Chicago, 2014, pp. 1115-1118.

[6]   H.H. Eroğlu and B.M. Eyüboğlu, "Sensitivity based image reconstruction for ICMREIT," *Int. Symp. In Biomed. Imag. (ISBI 2014)*, Beijing, 2014.

[7]   C. Göksu, B.M. Eyüboğlu, and H.H. Eroğlu, "A programmable current source for MRCDI and MREIT applications," in *Proc. 13th Mediter. Conf. Med. Biol. Eng. Comp. (MEDICON)*, Sevilla, 2013, vol.41, pp. 198-201.

[8]   H.H. Eroğlu, B.M. Eyüboğlu, C. Göksu, "Design and implementation of a bipolar current source for MR-EIT applications," in *Proc. 13th Mediter. Conf. Med. Biol. Eng. Comp. (MEDICON)*, Sevilla, 2013, vol.41, pp. 161-164.

[9]   H.H. Eroğlu, "Paralel ışın izdüşümleri yöntemiyle bilgisayarlı tomografi benzetimi", in *Proc. 17. Biyomedikal Mühendisliği Ulusal Toplanısı, (BİYOMUT)*, İstanbul, 2012, pp. 283-286.

[10]   H.H. Eroğlu, B.M. Eyüboğlu, "Tek kutuplu sabit akım uyarıcı tasarımı ve deneysel gerçeklenmesi", in *Proc. 17. Biyomed. Müh. Ulus. Top., (BİYOMUT)*, İstanbul, 2012, pp. 211-214.

[11]   H.H. Eroğlu and A.M. Hava, "Design and implementation of an ultracapacitor test system," in *Proc. IEEE 20th Int. Symp. Ind. Elect. (ISIE)*, Gdansk, 2011, pp. 194-199.

[12]   H.H. Eroğlu and A.M. Hava, "Ultrakondansatörlerin başarımlarının deneysel olarak değerlendirilmesi," in *Proc. Elek.-Elekt-Bilg. Müh. Semp., (ELECO)*, Bursa, 2010, pp. 259-263.

[13]   H.H. Eroğlu and A.M. Hava, "Güç elektroniği dönüştürücüleri ile ultrakondansatörlerin enerji yönetimi," in *Proc. Elek.-Elekt-Bilg. Müh. Semp., (ELECO)*, Bursa, 2010, pp. 254-258.

[14]   D.D. Demirgüneş, O. Eroğul, H.H. Eroğlu, and Z. Telatar, "Biyomedikal ve klinik mühendislik birimlerinde yürütülen tıbbi cihaz kalibrasyon hizmetleri ve önemi," in *Proc. 13. Biyomed. Müh. Ulus. Top., (BİYOMUT)*, Ankara, 2008.

[15]   O. Eroğul, D.D. Demirgüneş, and H.H. Eroğlu, "Klinik mühendisliği birimlerinin yapısı, faaliyetleri ve hastaneler için önemi," in *Proc. 13. Biyomed. Müh. Ulus. Top., (BİYOMUT)*, Ankara, 2008.

GRANTS/AWARDS

2014-2016 Scholarship: "Akım İndüklemeli Manyetik Rezonans Elektriksel Empedans Tomografisi", 113E979, The Scientific and Technological Research Council of Turkey (TÜBITAK).

2017- Scholarship: "Eş Zamanlı Manyetik Rezonans Difüzyon Tensörü ve İletkenlik Tensörü Görüntüleme", 116E157, The Scientific and Technological Research Council of Turkey (TÜBITAK).

PATENT APPLICATIONS

[1] B.M. Eyüboğlu, H.H. Eroğlu, and M. Sadighi, "Tek Kutuplu Kesit Seçici Gradyan Darbe Tabanlı Akım İndüklemeli Manyetik Rezonans Elektriksel Empedans Tomografisi (AİMREET) Darbe Dizini," Turkish Patent Institute pending patent No. P17/0601.

[2] B.M. Eyüboğlu, H.H. Eroğlu, M. Sadighi, K. Sümser, and N. Naji, "Çift kutuplu gradyan darbe tabanlı akım indüklemeli manyetik rezonans elektriksel empedans tomografisi (AİMREET) Darbe Dizini," Turkish Patent Institute, Pending Patent No. P16/0494.

[3] B.M. Eyüboğlu, K. Sümser, H.H. Eroğlu, M. Sadighi, and N. Naji, "Spin etiketli manyetik rezonans akim yoğunluğu ve elektriksel empedans görüntüleme (AİMREET) Darbe Dizini," Turkish Patent Institute, Pending Patent No. 2015/13995.

[4] Ş. Tereyağoğlu, A. Altuğ, H.H. Eroğlu, "Elektro-foto stimülasyon cihazı," Turkish Patent Institute, Pending Utility Model No. 2014/03858.